SEISMIC LANDSLIDE EXPOSURE ANALYSIS FOR TÜRKİYE

ANNISA RIZQILANA
July, 2025

SUPERVISORS:
Dr. H. Tanyas
Dr. L. Lombardo

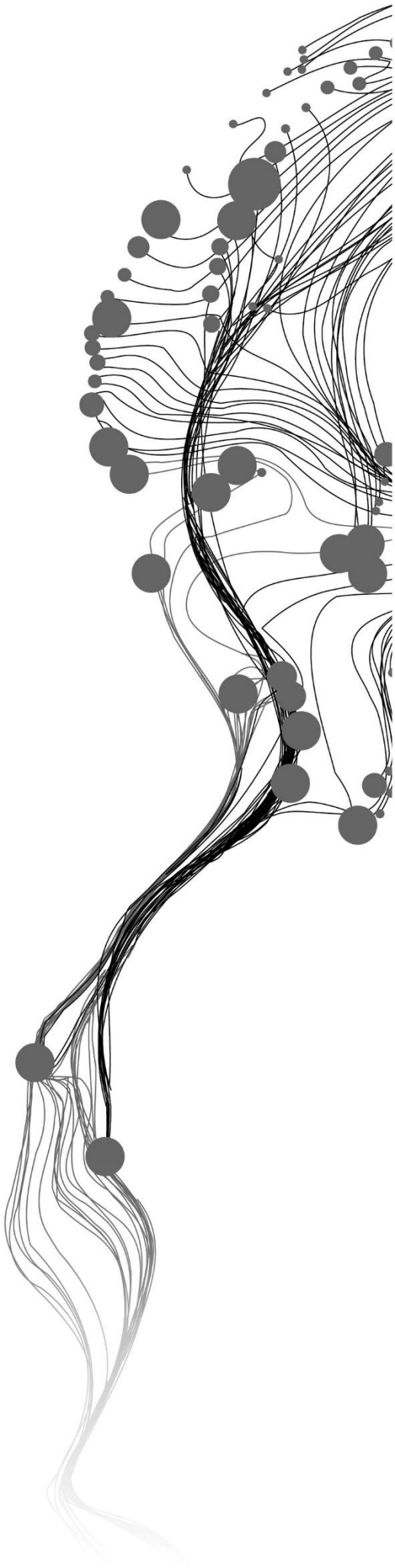

SEISMIC LANDSLIDE EXPOSURE ANALYSIS FOR TÜRKİYE

ANNISA RIZQILANA
Enschede, The Netherlands, July, 2025

Thesis submitted to the Faculty of Geo-Information Science and Earth Observation of the University of Twente in partial fulfilment of the requirements for the degree of Master of Science in Geo-information Science and Earth Observation.
Specialization: Natural Hazards and Disaster Risk Reduction

SUPERVISORS:
Dr. H. Tanyas
Dr. L. Lombardo

THESIS ASSESSMENT BOARD:
Prof. dr. C.J. van Westen(Chair)
Prof. Dr. Tolga Görüm (External Examiner, Istanbul Teknik Üniversitesi)

ABSTRACT

Earthquake-induced landslides are the most common secondary hazard triggered by earthquakes, particularly in mountainous regions of tectonically active countries like Türkiye. Although often overshadowed by the primary effect of the earthquake, these landslides can cause severe damage to infrastructure, disrupt access to affected areas, and delay emergency response and recovery efforts. Despite their hazardous potential, national-scale assessments that estimate the likelihood of future earthquake-triggered landslides and their potential impact on infrastructures remain limited. This study addresses this gap by developing a data-driven model to simulate earthquake-induced landslide susceptibility and estimate infrastructure exposure across Türkiye under different seismic hazard scenarios.

Using a Generalized Additive Model (GAM) framework, the susceptibility model was trained on two co-seismic landslide inventories, including the 2011 Van and 2023 Kahramanmaras earthquakes. A total of 17 variables were initially evaluated in the exploratory phase to understand their relationship with landslide occurrence. Based on their statistical relevance, four continuous variables, including slope steepness, local relief (LR), peak ground acceleration (PGA), and proximity to active faults, along with two categorical variables, which are lithology and land cover, were selected for the final model. Using both random cross-validation (RCV) and spatial cross-validation (SCV), the model achieved area under the curve (AUC) scores of 0.86 and 0.81, respectively. These results indicate that the model can predict landslide occurrence well despite the spatial differences.

Although the model does not include runout simulation or dynamic environmental conditions, it provides a practical and transferable framework for scenario-based assessment at a national scale. To explore how landslide susceptibility might vary under different earthquake conditions, the model was simulated under four PGA exceedance scenarios (2%, 10%, 50%, and 68% in 50 years) derived from Türkiye's national seismic hazard map. As the PGA intensity increases in rarer scenarios, the predicted susceptibility values also tend to rise, ranging from a maximum of 0.3 in the 68% scenario to as high as 0.82 in the 2% scenario. This trend shows that stronger but less frequent earthquakes have a bigger impact on slope stability.

To evaluate the potential consequences, an exposure assessment was carried out to estimate the spatial overlap between each susceptibility map scenario and the critical infrastructure across the country. This assessment combined both the susceptibility values and associated uncertainties to identify the number of exposed elements at risk (EaRs) and assess the confidence level of the predictions. While the amount of exposure varied depending on how infrastructure intersected with susceptible slope units, a general trend was observed: exposure under the 68% scenario was predominantly concentrated in lower susceptibility classes, whereas the 2% scenario showed a greater proportion of exposure in the higher susceptibility classes.

This study highlights the potential of integrating probabilistic seismic hazard maps with data-driven susceptibility models to support future prediction of earthquake-induced landslides. Enhancing data resolution and completeness will be essential for improving model performance and expanding its applicability to other regions or scenarios. In addition, combining this approach with simplified physically based models and promoting open data sharing could encourage broader collaboration and facilitate more robust, flexible, and widely applicable landslide risk assessments.

Keywords: earthquake-induce landslide, susceptibility modeling, seismic hazard map, exposure, Türkiye

ACKNOWLEDGMENTS

When I first arrived in the Netherlands to begin this journey, I brought with me professional experience and a genuine curiosity, but I quickly realized how little I actually knew. The first two quartiles were overwhelming and full of self-doubt. However, I was lucky to have support from the people around me, who helped me push through and grow, both academically and personally.

I would like to express my sincere gratitude to all the lecturers at ITC for their guidance and support throughout this journey. Their enthusiasm, encouragement, constructive feedback, and patience played a key role in helping me through this academic process. Each course and discussion pushed me to think critically and helped me grow both as a student and a professional. I am especially thankful to my supervisors, Hakan and Luigi, for their trust and support in every process of my thesis. Their willingness to listen, guide, and challenge gave me the confidence to move forward, even when I was uncertain. I truly appreciate their belief in me—it made all the difference.

Special thanks also go to LPDP Indonesia for giving me the opportunity to pursue my dream of studying abroad. It has always been my goal to continue my education in the Netherlands, and with this scholarship, that dream became a reality. Over the past two years, I have gained not only academic knowledge but also unforgettable experiences that have shaped who I am today.

To my Indonesian friends (Arthur, Azza, Dian, Fadhil, Irene, and Kak Widya) and my fellow ITC classmates and friends (Daniel, David, Laine, Sanskriti, Shawn, and Simone), thank you for being my home away from home. Your friendship and support have meant the world to me. Thank you for the laughter, the long nights, and for sharing both the struggles and the milestones. Together, we made countless memories that I will always carry with me.

I would also like to express my heartfelt thanks to my family, especially my cute little brother, Muhammad Shalahuddin Alja'farawy. Thank you for always being just one call away. Your presence and reassurance helped me stay grounded during the most stressful times. As you near the completion of your PhD, I sincerely hope your dream of securing a postdoc in Europe comes true. You deserve it more than anyone I know.

To anyone I may have forgotten to mention by name, please know that your support, kindness, and presence have not gone unnoticed. Whether it was through a simple check-in message, a shared laugh during stressful times, or a quiet moment in the study room. I am truly grateful to everyone who walked alongside me and helped make this journey a little lighter. Your support reminded me that I wasn't alone, and that was often all I needed to keep going.

TABLE OF CONTENTS

LIST OF FIGURES

LIST OF TABLES

LIST OF ABBREVIATIONS

AUC	Area Under the Curve
DEM	Digital Elevation Model
EAF	East Anatolian Fault
EaR/EaRs	Element at Risks
FN	False Negative
FP	False Positive
GIS	Geographic Information System
GAM	Generalized Additive Model
GMPE	Ground Motion Prediction Equation
HS	High Susceptibility
HU	High Uncertainty
LR	Local Relief
LS	Low Susceptibility
LU	Low Uncertainty
MS	Moderate Susceptibility
MU	Moderate Uncertainty
MMI	Modified Mercalli Intensity
NAF	North Anatolian Fault
OSM	Open Street Map
PGA	Peak Ground Acceleration
PGV	Peak Ground Velocity
PSHA	Probabilistic Seismic Hazard Assessment
RCV	Random Cross Validation
ROC	Receiver Operating Characteristics
SCV	Spatial Cross Validation
TN	True Negative
TP	True Positive
VIF	Variance Inflation Factor
VLS	Very Low Susceptibility
VLU	Very Low Uncertainty
VRM	Vector Ruggedness Measure
TWI	Topographic Wetness Index

1. INTRODUCTION

1.1. Background

Earthquake-induced landslides are the most widespread and destructive secondary hazards triggered by strong seismic events, particularly for communities living in tectonically active mountainous landscapes (Bird & Bommer, 2004; Mousavi et al., 2011; Jesse et al., 2018). These events can significantly amplify the earthquake impacts, such as loss of life, infrastructure damage, and socioeconomic problem (Tanyaş et al., 2017; Shao & Xu, 2022; Ojomo et al., 2024; Wang et al., 2024). The susceptibility of a given landscape to slope failures increases in the aftermath of strong earthquakes as they reduce the shear strength of hillslopes (Karakas et al., 2024; Xi, Lombardo, et al., 2024; Xi, Tanyas, et al., 2024). Therefore, understanding the spatial distribution of landslide susceptibility following major earthquakes is critical for hazard assessment and land-use planning (Jesse et al., 2018; Lima et al., 2022).

Numerous approaches have been developed to model landslide susceptibility, including earthquake-induced landslide, which is generally categorized into physical-based and statistical-based methods (Lima et al., 2022). Physically based models, such as Newmark analysis, simulate slope failure using detailed geotechnical and seismic parameters, taking into account both the ground shaking that initiates the landslide and the mechanical response of the slope during failure (Bray & Travasarou, 2007). However, physics-based approaches require detailed datasets to accurately represent terrain properties, material behavior, and triggering conditions (Cheng et al., 2021; Z. Chen & Wang, 2023). Therefore, while they offer high accuracy, these approaches mainly suitable for local scale assessments, such as sub-catchment (Shao & Xu, 2022).

Contrary, data-driven models rely on observed landslide inventories and their relationship with environmental conditioning factors to learn spatial patterns of landslide occurrences (Kritikos et al., 2015; Tanyas et al., 2019). This makes the model's accuracy and reliability depend on the availability and completeness of the data (Robinson et al., 2018; Cheng et al., 2021). This approach is often used for regional-scale assessments as it does not need as much detailed data and can be easily applied across wide regions (Lima et al., 2022; Shao & Xu, 2022).

In both modeling approaches, ground shaking is one of the main input variables, typically represented as peak ground acceleration (PGA) (Nowicki et al., 2014; Cheng et al., 2021; Alvioli et al., 2024). Most studies obtain PGA values from empirical Ground Motion Prediction Equations (GMPEs) or ShakeMaps derived from specific historical earthquakes (Nowicki et al., 2014; Allstadt et al., 2018). However, these sources are event-specific, which relies on the historical ground motion record, making it less reliable for higher earthquake magnitudes and broader distances in the future scenario analysis (Nakanishi & Takemura, 2023; Vandana et al., 2024).

Alternatively, Probabilistic Seismic Hazard Assessment (PSHA) is another method for estimating ground motion parameters for future earthquakes. It provides a probabilistic estimation of expected PGA over a specified time window while taking into account the uncertainties of earthquake location, time, and magnitude (Caccavale et al., 2017; Gerstenberger et al., 2020; Shao et al., 2023). The primary output of PSHA is the seismic hazard map, which presents the spatial distribution of ground motion intensities at various exceedance probabilities (Akkar et al., 2018). These maps are especially valuable for long-term hazard prediction and scenario-based modeling, as they allow researchers and planners to assess the spatial

variation of seismic risk without relying on a single historical earthquake event. However, their integration into earthquake-induced landslide susceptibility remains limited.

Furthermore, compared to the primary hazards such as earthquakes and rainfall-induced landslides, the exposure assessment of earthquake-induced landslides remains unexplored, particularly at the national scale. This may be due to the complexity of the earthquake-induced landslide modeling process and the availability of the event-specific data. However, as aforementioned, earthquake-induced landslides can cause additional damage, particularly in mountainous areas. Therefore, including them in exposure assessment could give a better hazard understanding and support proactive spatial planning (Wasowski et al., 2011; B. Zhang et al., 2022).

1.2. Study Case

Türkiye is a country with frequent and damaging earthquakes. Several strong earthquakes have been recorded in the last three decades, and the most recent, the 2023 Kahramanmaras earthquake sequence, caused over 50,000 casualties and damaged about 4 million infrastructures (ADRC, 2023; Wikipedia, 2025). However, no national-scale data-driven model currently exists to assess earthquake-induced landslide susceptibility, and no known study has used PGA derived from a seismic hazard map to drive such a model. Most earthquake-induced landslide studies in Türkiye remain localized, focusing on individual events like the 2011 Van earthquake or the 2023 Kahramanmaraş earthquake (Gorum, 2016; Karakas et al., 2024).

1.3. Research Aim

As previously discussed, despite the destructive potential of earthquake-induced landslides, their susceptibility and exposure assessment, particularly on a national scale, remain limited. Moreover, no existing study has incorporated PGA derived from seismic hazard maps for earthquake-induced landslide susceptibility. To address these gaps, this research aims to develop a national-scale co-seismic landslide susceptibility model using data-driven methods. The model is based on co-seismic landslide inventories from the 2011 Van (Gorum, 2016) and 2023 Kahramanmaraş (Yılmaz, et al., unpublished) earthquake sequences. PGA values extracted from a seismic hazard map of Türkiye are utilized to simulate multiple earthquake scenarios and generate spatial predictions of landslide susceptibility across the country.

Furthermore, this study integrates the resulting susceptibility maps with spatial datasets of elements at risk (EaRs) to assess their exposure under different seismic hazard conditions. By combining landslide susceptibility modeling with exposure analysis, this research is expected to enhance a better understanding of earthquake-triggered landslide impacts and support future scenario-based hazard assessment across the country.

1.4. Research Objectives and Research Questions

The main objective of this study is to model earthquake-induced landslides across Türkiye and assess their potential impact under different seismic scenarios.

Based on the overall objectives, sub-objectives are identified as follows:

1. To generate a data-driven model for the co-seismic landslides triggered by the 2011 and 2023 Türkiye earthquake sequence
    - What environmental conditions influenced the spatial distribution of the landslides triggered by the earthquake sequence?
    - Which predictive factors most strongly contribute to the model?

2. To incorporate seismic hazard map information as an input parameter in the earthquake-induced landslide prediction across Türkiye
    - How can a seismic hazard map be used to estimate the spatial distribution of earthquake-induced landslides for future events?
    - How does the earthquake-induced landslide susceptibility vary across different seismic hazard scenarios?

3. To assess the exposure of elements-at-risk (EaR) under multiple earthquake-induced landslide susceptibility scenarios.
    - How does the exposure of EaR vary across different seismic hazard scenarios in Türkiye?

2. STUDY AREA & THE DATASETS

This chapter provides the spatial extent and datasets used in this research. Section 2.1 introduces the geographical scope of the study, including its tectonic and topographic characteristics. Section 2.2 explains the landslide inventories utilized, derived from past co-seismic events in 2011 and 2023. Section 2.3 presents the seismic and environmental conditioning factors used as controlling parameters observed. Section 2.4 describes the seismic hazard map used as the ground motion input on the simulation, and Section 2.5 discusses the EaR considered for exposure analysis.

2.1. Study Area

Türkiye is formed by the tectonic collision of the Arabian and African plates, which are still actively moving westward and generating two major fault zones: the North Anatolian Fault Zone (NAF) and the East Anatolian Fault Zone (EAF) (Tatar et al., 2020), Fig 1. The active tectonic movement releases energy, generates various ground movements, and creates a young and steep topography with weak shear strength hillslope (Karakas et al., 2021).

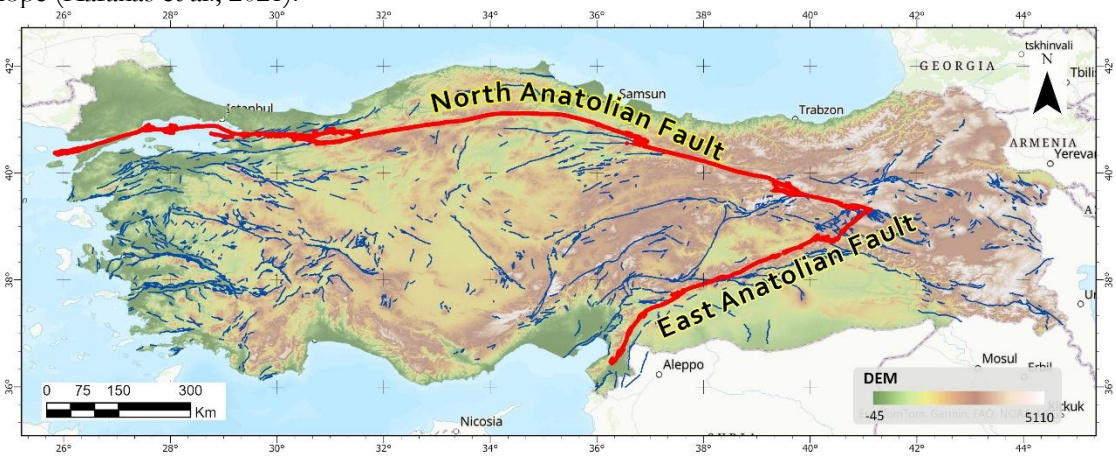

Fig 1 The tectonic setting of Türkiye. The red lines illustrate the major active faults, the North Anatolian and East Anatolian faults, while the blue lines represent another active fault system across the region.

As shown in Fig 2, the study area covered the areas affected by the 2011 Van earthquake in the northeast and the 2023 Kahramanmaras earthquake in the south-central of Turkey. Although many strong earthquakes have been recorded in the last three decades, including 1999 Izmit, 1999 Düzce, 2011 Van, 2020 Elazig, and 2020 Izmir earthquakes, earthquake-induced landslides are rarely investigated in the country (Görüm et al., 2023). For the moment, there are only two landslide event inventories in Türkiye, the first one for the 2011 Van earthquake (Gorum, 2016) and the second one for the 2023 Kahramanmaras earthquake (Yılmaz, et al., unpublished) sequence. Therefore, I will use these two inventories in the scope of this research to develop a predictive landslide model. The study area and the

The 2011 Van earthquake occurred at a shallow depth on an unmapped reverse fault within the compressional tectonic zone of EAF (Utkucu, 2013). The earthquake ruptured approximately 60 x 20 km rupture with an average displacement of 2 meters and a focal depth of 10-15 km. It triggered landslides over a 2,480 km^2 area (Gorum, 2016).

On the other hand, the 2023 earthquake sequence consists of two major shocks. The epicenter of the first earthquake is located around 15 km east of EAF and the earthquake caused over 6 m offset, while the second was located approximately 90 km north of the fault with 7 m surface displacement (Mai et al., 2023;

Melgar et al., 2023). This earthquake sequence triggered thousands of slope failures over a 100 km² area (U. S. Geological Survey, 2023a, 2023b).

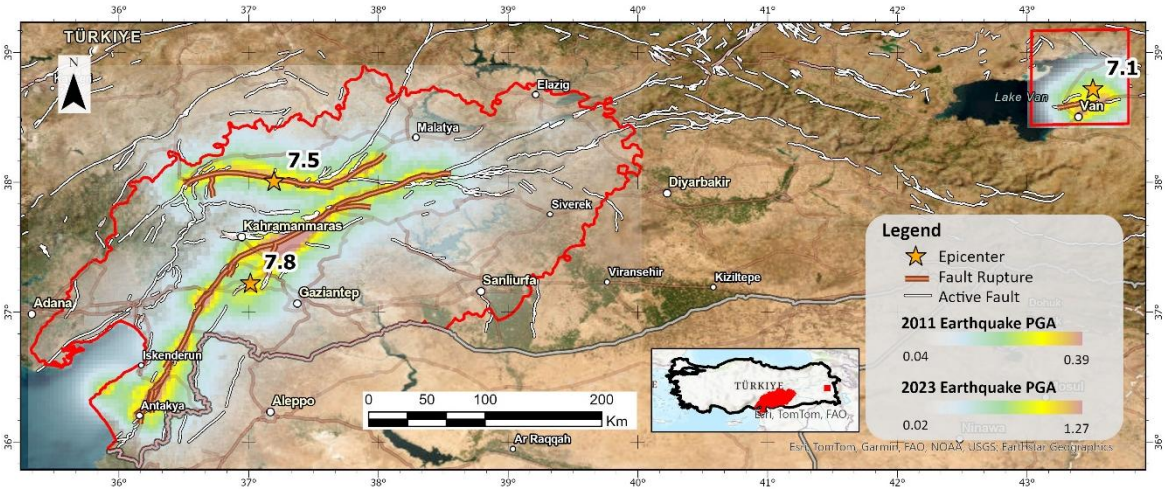

Fig 2 The study area consists of two separate areas which affected by the 2011 and 2023 Türkiye earthquakes. The picture shows the study area including the PGA, the source, and the fault rupture of each event.

Both earthquakes happened in the EAF tectonic system with various morphometric and geological conditions (Gorum, 2016; Görüm et al., 2023). The Van region is dominated by sedimentary, volcanic, and ophiolitic rocks, whereas the Kahramanmaraş region features a more complex mixture of sedimentary, ophiolitic, and metamorphic rocks (Çaglayan & Yurtseven, 1998). These lithological differences influence the landslide mechanisms in each area and may affect how susceptible the slopes are to ground shaking.

In addition to its complex geology, the climatic and topographic conditions of the country may also play some roles in landslide occurrences. The country has several climatic zones, including Mediterranean, continental, and semi-arid systems, making it have various precipitation and temperature pattern (Türkeş, 1996). The Kahramanmaraş region is characterized by a dry summer, cold and wet winter, and semi-humid to semi-arid subtropical due to Mediterranean influence. In contrast, the Van region has a continental highland climate characterized by colder winters, drier conditions, and more extreme seasonal variations. These climatic differences can influence vegetation cover, erosion rates, and weathering processes, which could affect long-term slope stability and the spatial patterns of landslide susceptibility.

As for the topographic characteristics of the country, it is mostly mountainous and rugged, which can be grouped into three classes based on its origin, including tectonic, volcanic, and erosion (Deniz Ekinci, 2012). Kahramanmaraş is dominated by the Southeastern Taurus Mountains and features a highly mountainous terrain, with nearly 60% of its area covered by rugged slopes. In contrast, Van Province in Eastern Anatolia lies within a high-altitude plateau surrounded by mountainous ridges, including volcanic peaks. The area's rough terrain, combined with its location within a tectonically active zone. Together, these contrasting landscapes represent different geomorphological settings, offering useful insights into how topography influences the spatial distribution of landslide susceptibility across Türkiye.

2.2. Landslide Inventories

To study earthquake-induced landslides in Türkiye, this research utilized the co-seismic landslide inventories of the 2011 Van and 2023 Kahramanmaraş earthquakes. The 2011 inventory, published by Gorum (2016), contains 82 documented landslides, which mostly consist of falls and slides. However, different landslide types were not indicated for each polygon in the inventory.

The 2023 inventory, developed by Yılmaz, et al., is currently unpublished. Over twenty thousand co-seismic landslides are stored in the inventory. The smallest landslide in inventory covers an area of 4 m^2, while the largest exceeds 1 km^2. Over 8,000 of the cases happened in areas larger than 1,000 m^2. These landslide cases are generally classified into six categories based on their movement type, which are fall, flow, avalanche, slide, lateral spread, and complex.

The following descriptions of landslide movement type are based on the classification proposed by Varnes (1978). A fall-moving landslide is characterized by a very rapid to extremely rapid movement that occurs on a steep slope or cliffs, typically involving little or no shear displacement. The detached material, either rock or debris, falls freely from the slope in various sizes. An avalanches-type landslide is a rapid movement downslope, typically associated with snow and ice. This landslide movement type in the inventory has two types of material, debris and rock. In debris avalanches, the movement is progressive yet rapid, involving the entire mass of unconsolidated material. On the other hand, rock avalanches involve fragmented rock masses, often triggered by structural failure or intense ground shaking.

Slide-movement landslide is a progressive rock or debris movement down the slope, driven by the intense shear strain and displacement along the well-defined surface. This movement type is classified into rotational and translational slides according to the failure geometry and the nature of the movement. In contrast, a flow-moving landslide is a fluid-like debris or earth material downslope movement, influenced by the water contained in the material. The transition from slide to flow behavior in debris material depends on factors such as water content, material mobility, and movement character.

Lateral spread movement refers to the displacement of soil or rock driven by shear or tensile fracturing, predominantly occurring in bedrock. It is often considered as complex-type landslide due to its mechanism, which may involve elements of rotational, translational, and even flow movement. Lateral spreads typically develop progressively, beginning in a localized area and expanding outward to a broader area. As aforementioned, complex-type landslides are also present in the inventory. These involve a combination of two or more types of landslide movement, either occurring in different parts of the moving mass or at different stages of landslide development. Two types of complex movements identified in the inventory are earth slide-earth flow and rock slide-debris avalanche.

Most landslides triggered by the Türkiye 2023 earthquake occurred in steep terrain, with slope angles exceeding 20 degrees. Therefore, nearly half of the inventory consists of rockfalls, followed by avalanches, which account for approximately one-quarter of the cases. Flows and slide landslide types have similar proportions, while the complex-type landslide is the least, with only 99 out of the total 20,270 cases. However, although rockfall-type landslides have the largest portion of the inventory, they are excluded from further analysis due to their distinct movement mechanism, leaving the remaining five categories. A detail of the inventory is displayed in Table 1.

Table 1 Co-seismic landslides inventory of Türkiye's February 2023 earthquake event.

Movement Type	Material Type	Total cases	Total area (km2)
Fall	Rock	9,286	28.58
Avalanche	Rock	1,158	8.05
	Debris	3,617	10.48
Slide	Rock	59	1.59
	Earth	2,884	4.51
Flow	Debris	3	0.12

Movement Type	Material Type	Total cases	Total area (km2)
	Earth	2,843	0.74
Lateral spread	Earth	321	4.25
Complex	Rock and debris	73	7.42
	Earth	26	0.28
Total		**20,270**	**66.02**

The polygons of the landslide inventory are later converted into raster format to construct the data matrix used as an input for the model. The detailed process of this conversion is explained in Section 3.1 (data matrix). This step ensures spatial alignment between the inventory and the controlling parameters used in the analysis.

2.3. Controlling Parameters

Earthquake-induced landslides happen cause of the complex interaction between the controlling parameters, such as seismic parameters, terrain parameters, and slope materials. Understanding the interaction mechanism between these parameters might improve earthquake-induced landslide distribution predictions (Gorum et al., 2011). However, there is no universal guideline to determine which parameter should be included in the model due to the complexity and spatial heterogeneity in different regions (Ayalew & Yamagishi, 2005). Thirteen controlling parameters are utilized in this study, selected based on a literature review of previous landslide research. These parameters include DEM derivatives (slope steepness, local relief, vector ruggedness measure (VRM), and topographic wetness index (TWI), northness, eastness, plan curvature, and profile curvature), proximity to fault lines, PGA, lithology, and land cover (Fig 3). They were then used to build the data matrix through zonal statistics analysis using GIS software. The detailed methodology for generating the data matrix is further explained in Section 3.1 (Data Matrix).

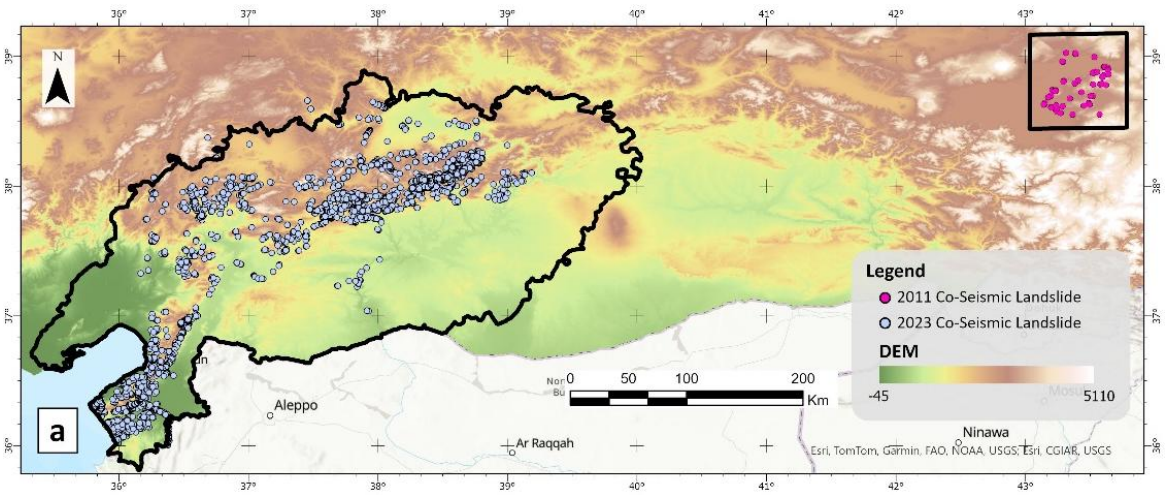

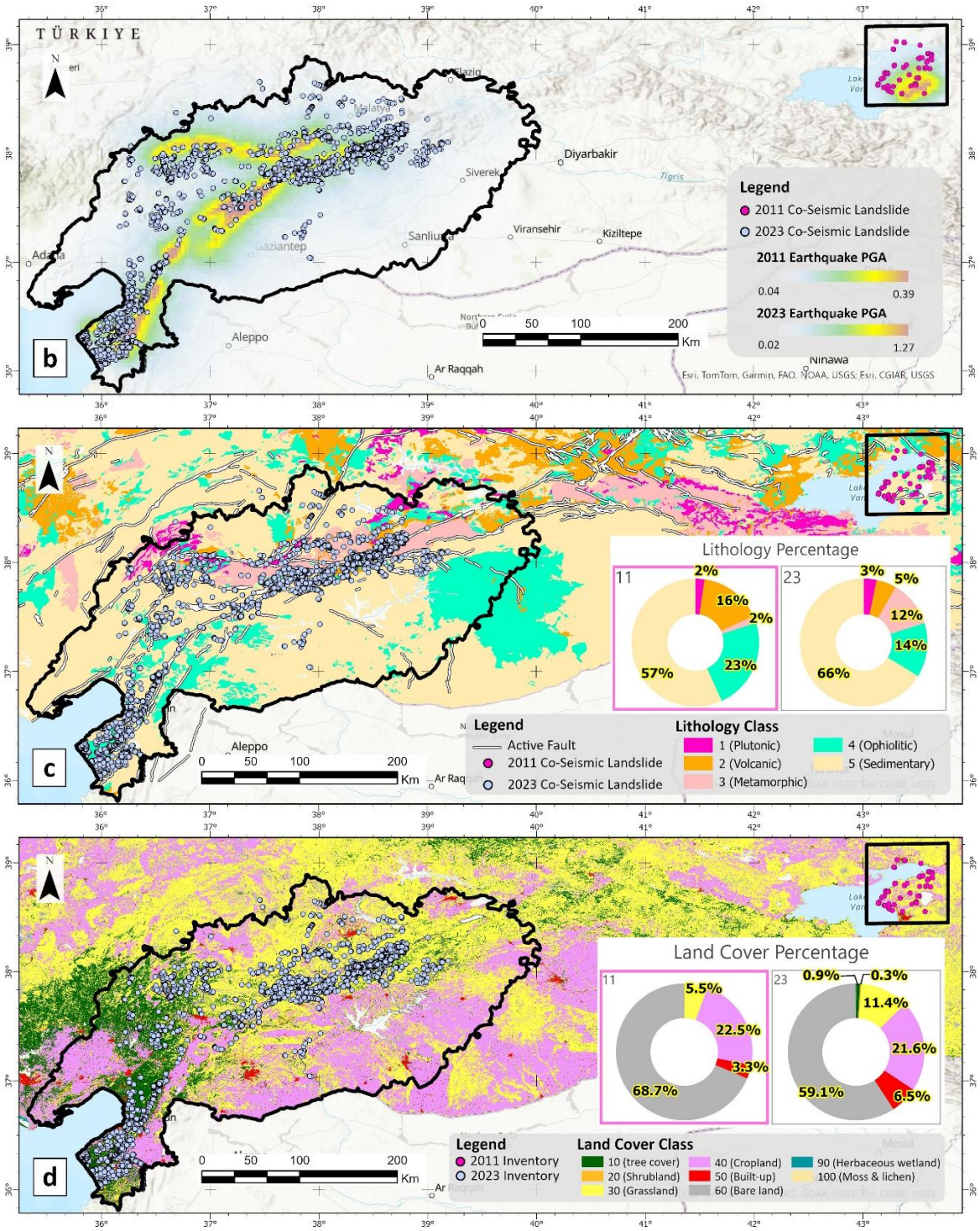

Fig 3 The spatial distribution of the controlling parameter explored in this research, including the DEM that then derived into slope steepness, the aspects, the curvatures, LR, TWI, and VRM (a), PGA of each earthquake (b), the geology condition including lithological type and the active faults (c), and the land cover type (d).

DEMs are an essential tool in landslide prediction models, as they provide the basic information for deriving terrain parameters, such as slope steepness and aspect. This research utilized the DEM provided by NASA, which is a modernized version of SRTM DEM with a medium spatial resolution of 30 meters. The dataset is open-source and was easily accessed and imported through the OpenTopography plugin in QGIS software. The terrain parameters derived from the DEM for this model include slope steepness, aspect,

curvature, LR, VRM, and TWI. All DEM derivatives were processed using modules in GRASS GIS software, such as r.slope.aspect, r.mapcalc, and r.vector.ruggedness.

Slope steepness indicates how steep the slope is. Generally, steeper slopes have a higher probability of landslide occurrence because the driving force acting downslope increases as the slope gets steeper, while the resistance shear strength does not proportionally increase (S. Lee & Min, 2001). Therefore, slope steepness is one of the most important control parameters for landslide prediction. The slope steepness values in the study area range from 0 to 81.5 degrees, with most pixels concentrated within the 0 - 30^{o} range, indicating a gentle to moderate slope.

Aspect, or slope orientation, relates to several environmental factors, such as sunlight exposure, discontinuities, wind direction, soil moisture, and saturation level, which affect the degree of weathering and erosion on a slope (Ayalew & Yamagishi, 2005). Therefore, studies have shown a tendency for slope failure occurrence to align with a specific aspect, indicating a directional failure distribution (S. Lee & Min, 2001; Khazai & Sitar, 2004; Ayalew & Yamagishi, 2005). To simplify the modeling process, the aspect was decomposed into two continuous variables: northness and eastness. Each is calculated using the cosine and sine of the aspect angle, making both values range from -1 to 1.

Curvature values represent the shape of the terrain in both horizontal and vertical dimensions. A positive curvature value indicates a convex shape, while a negative value corresponds to a concave form. The value near zero value commonly reflects a flat or planar slope (S. Lee & Min, 2001; W. Chen et al., 2014). Concave-shaped slope tends to accumulate and retain water, which potentially reduces the material's shear strength and increases the slope failure likelihood (S. Lee & Min, 2001). The profile curvature within the study area ranges from -0.12 to 0.08, while the planar curvature values are near 0. This indicates that most slopes in the area have relatively gentle curvature in both vertical and horizontal directions.

Local relief corresponds to the topographic change, which is defined as the difference between the minimum and maximum elevation in a certain area (Schmidt & Montgomery, 1995). It is often associated with structural discontinuities on the slope, such as joints and faults, which tend to indicate higher permeability and potentially increase the slope susceptibility to failure (Conforti et al., 2014). Several studies showed a correlation between landslide frequency and local relief value, particularly in earthquake-induced landslide cases (X. Chen et al., 2017; Qin et al., 2023). The LR in this study area ranges from 0 – 1327, with most of the pixels concentrated within the 100 to 500 range, which indicates a wide elevation variation within the localized area.

VRM is a rugged terrain measurement using the three-dimensional orthogonal dispersion of vectors perpendicular to the terrain surface (Sappington et al., 2007). It reflects the slope and aspect heterogeneity within a given area. Higher VRM values indicate more rugged and complex terrain, which often correlates with slope instability and landslide frequency (He et al., 2021). In the study area, VRM values range from 0 to 0.6, with most of the pixels gathered in 0 and 0.02. This indicates that the terrain likely has a smooth and uniform surface. However, the presence of high VRM values reflects the localized complex topography.

TWI represents water flow accumulation within a watershed and is commonly used to capture the topographic control over hydrological processes. A high TWI value indicates an area with a higher water accumulation, which could increase the landslide likelihood, especially when combined with a steep slope (Ghasemian et al., 2022). The TWI value within the study area ranges from -1.3 to 27.8, with most pixels concentrated between 0 and 15. This indicates that the majority of the area has moderate wetness conditions, although some areas show a high potential for water accumulation.

As a triggering factor in an earthquake-induced landslide event, ground motion is considered to have a significant contribution to the landslide distribution (Khazai & Sitar, 2004). Although there are three seismic parameters in every earthquake event, including PGA, PGV, and MMI, this study only utilizes PGA, as is commonly used in previous studies. Moreover, according to (Omine et al. (2008), PGA is more sensitive to slight damage. The PGA dataset used in this research is a composite of PGA values from both epicenters of the 2023 Türkiye earthquake event, sourced from USGS ShakeMap. The values range from 0 to 1.27g, with the highest value concentrated near the fault rupture zones, reflecting areas that experienced the most intense ground shaking.

Geological settings, such as the type of lithology, play a significant role in the distribution of earthquake-induced landslides, as each lithological unit has varying levels of susceptibility to failure (Chigira & Yagi, 2006; Khazai & Sitar, 2004). The geological map used in this research was sourced from Türkiye's General Directorate of Mineral Research and Exploration Institute. The dataset has various types of geological formations from different ages, but it was generalized into five lithological types, including plutonic, volcanic, metamorphic, ophiolitic, and sedimentary. The dominant lithological type within the study area is sedimentary, while plutonic is the least.

The presence of faults along hillslopes significantly influences landslide distribution as it generates fractures and discontinuities within the slope materials, creating a weak shear strength condition (Chigira & Yagi, 2006; Keefer, 2000; Khazai & Sitar, 2004). Studies highlighted that landslide tends to accumulate near the fault line on the steep slope, and their frequency generally decreases as the distance to the fault increases (W. Chen et al., 2014; Basharat et al., 2016; Shafique, 2020). The fault dataset utilized in this research was obtained from the same source as the geological map. Rather than using the presence of active faults as a categorical variable, this study utilized the distance to the nearest fault as a continuous parameter. The Euclidean Distance tool in ArcGIS Pro was used to generate the proximity-to-fault raster, resulting in a value ranging from 0 to 0.7. The majority of the pixels fall within the 0 - 0.2 range, indicating the dense presence of active faults around the study area.

Land cover refers to biological and physical features present on the earth's surface, which includes both natural and anthropogenic features such as vegetation, soil, and water bodies (Herold et al., 2006). While the influence of land cover on landslide occurrence might vary and sometimes be ambiguous, it remains an important factor, as the mass-wasting processes are often influenced by the surface cover (Basharat et al., 2016). This research utilizes land cover data from ESA WorldCover 2021, which provides a 10-meter resolution land cover map derived from Sentinel 1 and 2. The dataset includes 11 land cover classes, but only 8 are present in the study area, which are tree cover, shrubland, grassland, cropland, built-up, bare land, herbaceous wetland, and moss and lichen. The dominant land cover types in the study area are grassland and cropland, while moss and lichen are the least.

Rainfall is one of the most common landslide triggers (Johnston et al., 2021). High rainfall amounts in steep slope areas significantly increase the landslide frequency because the accumulated water increases the pore pressure and changes the slope stability (Tetteh et al., 2025; K. Zhang et al., 2019). However, including rainfall would require event-specific timing and intensity data, which will limit the model transferability to future earthquake events or broader regions. Therefore, rainfall is excluded from this research due to its lack of applicability, particularly for future predictions.

2.4. Seismic Hazard Map

A seismic hazard map is a map that visualizes the potential ground-shaking intensity at a given location, which has been considered an important tool for hazard estimation, mitigation, and preparedness action (Sreejaya et al., 2022). According to USGS (2019), the seismic hazard map is usually pictured as contours that store the ground movement information, including the PGA, with a chance of exceedance in a specific return period. In earthquake-induced landslides, ground motion intensity is considered the triggering factor, making its integration significant for earthquake-induced landslide distribution (Khazai & Sitar, 2004). However, the use of seismic hazard maps as the source of ground motion intensity in the landslide susceptibility model has never been done before.

As a novelty, this research utilized Türkiye's seismic hazard map (Akkar et al., 2018) to derive the ground motion intensity value as an input for model simulation. The dataset consists of both PGA and PGV values for 2%, 10%, 50%, and 68% exceedance probability in 50 years. However, this research utilized only the PGA for all four exceedance rates for model simulation. The PGA spatial distribution of 68% exceedance is displayed in Fig 4, while the rest is in Appendix A.1.

The exceedance rate in a specific return period means there is a chance that the ground shaking at a location will exceed a certain intensity at least once within the return period (USGS, 2019). This means that the 2% exceedance scenarios cause a very strong ground motion which rarely happens. In contrast, the 68% exceedance causes minor shaking and happens frequently. This behavior is reflected in the PGA value of each scenario, where the 68% scenario only ranges from 0.02 to 0.2, while the rarest scenario ranges from 0.15 to 1.33. Despite the contrast range, overall the scenarios show similar patterns where the high PGA values are concentrated along the major fault zones.

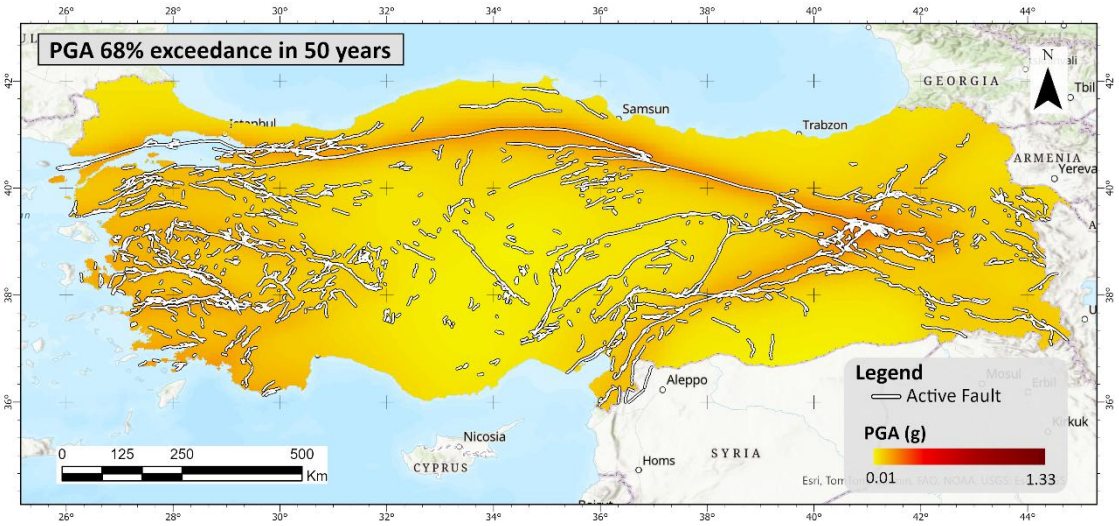

Fig 4 PGA of 68% exceedance probability in 50 years, derived from Türkiye's seismic hazard map

2.5. Element at Risks

According to van Westen et al., (2006), EaRs refer to the elements that are at risk, including population, building, and economic activities. EaRs are an important factor in hazard risk estimation, as it is included in its calculation formula. Although this research is not going to do a risk analysis, however, overlay the EaRs with the susceptibility map might give some insight to the stakeholders.

The selection of which EaR to analyze depends on multiple factors, including the type of hazard, the vulnerability of the assets, the spatial extent of the study area, and the availability of the data (van Westen et

al., 2006). Moreover, EaR can be characterized in various ways, including spatial, temporal, population, and thematic, depending on the purpose of the research. This research focuses on spatial EaRs, which are generally divided into three types: EaRs measured by length, by area, and by count (Table 2).

Road networks, railways, gas pipelines, and electricity lines were selected as the EaRs measured by length. These elements are critical components of the national infrastructure system. However, their elongated nature is often transversed across various terrains, including mountainous regions, making them exposed to hazards, including landslides (van Westen et al., 2006; E. M. Lee et al., 2016; Marchesini et al., 2024). The railway and road datasets were downloaded from the open street map (OSM) on May 26th, 2025. The railway dataset was used directly, while the road network was filtered to include only the trunk, primary, and secondary road types for the relevance of national-scale analysis. The gas pipeline dataset was obtained from the Global Energy Monitor, which is regularly updated but permission-based data. The electricity distribution line dataset was sourced from the World Bank ESMAP Gridfinder platform. Both pipeline and electricity line datasets were accessed on April 9th, 2025.

The EaRs measured by areas included agricultural land, and commercial and industrial zones. These elements represent critical economic and assets that may be directly and indirectly disturbed by the landslide impacts(van Westen et al., 2006; Francesco Caleca et al., 2025). The spatial extent of the agricultural land was derived from the CORINE Land Cover 2018. This dataset categorizes agricultural areas into four main classes: arable land, permanent crops, pastures, and heterogeneous agricultural areas. Each is further subdivided into specific agricultural land use types. Similar to the road and railway datasets, the commercial and industrial zones were downloaded from OSM. Both datasets were accessed on May 26, 2025. These land use categories were selected for their economic relevance and their potential to be impacted by ground movement, especially in regions where they overlap with medium to high landslide susceptibility zones.

Building and critical infrastructure were selected as the EaRs measured by count. These point-based elements represent population density, economic investment, and essential services, which are potentially impacted by earthquake-induced landslide events (van Westen et al., 2006; Uzielli et al., 2008; Francesco Caleca et al., 2025). Both building footprint and critical infrastructure data were obtained from OSM on May 26th, 2025. While the building footprint data can be directly used, the critical infrastructure data were extracted from the POIS layer. For the purpose of this study, only infrastructure relevant to transportation, finance, government, health, education, and emergency services was selected.

Table 2 EaRs used in this research

Measurement Types	EaRs	Sources
Line	Road network	OSM
	Railway	OSM
	Gas pipeline	Global Energy Monitor
	Electricity transmission line	World Bank ESMAP Gridfinder
Area	Agriculture area	CORINE Land Cover 2018
	Commercial and industrial area	OSM
Feature count	Building	OSM
	Critical infrastructure	OSM

3. METHODOLOGY

This chapter outlines the methodological framework applied in this study. Section 3.1 explains how the data matrix was constructed by integrating landslide inventory data with the controlling parameters. Section 3.2 describes the development of the co-seismic landslide model using a Generalized Additive Model (GAM). Section 3.3 presents the scenario-based simulations using different PGA values derived from the seismic hazard map to generate national-scale susceptibility predictions. Section 3.4 details the process of estimating the exposure of EaRs under each susceptibility scenario.

3.1. Data Matrix

A data matrix was created to combine the landslide occurrence as the target variable (y) and landslide controlling parameters as independent variables or predictors (x) for model development. Both the landslide inventories and their controlling parameter layers were partitioned into slope units as the mapping unit for the analysis. A slope unit is one kind of mapping unit that is made by partitioning terrain by drainage and dividing lines, making it represent the slope characteristic better, and more suitable for geomorphological use (Alvioli et al., 2016; Woodard et al., 2024). The landslide inventory polygons were converted into point features by extracting their centroids, which were then used to count the number of landslides occurring within each slope unit. This process was done in ArcGIS Pro. Afterward, the landslide counts within each slope unit were classified into binary categories, landslide (1) and no landslide (0), using presence or absence structure. This process was done in R once the data matrix was built and ready to be used to initiate the model.

Unlike landslide presence, different methods were applied to assign controlling parameter values to each slope unit. Although all variables were extracted using the Zonal Statistics function in ArcGIS Pro, the statistical methods varied depending on the parameter type. The following approach was used in Moreno et al., (2023). Both mean and standard deviation were calculated for terrain parameters, such as slope steepness, aspects, curvatures, TWI, and VRM. Additionally, each slope unit's range of slope steepness was used to compute local relief.

The mean value within each slope unit was calculated for proximity to the active fault. In contrast, the maximum value was extracted using the Zonal Statistic function for PGA. For categorical parameter values, including geology and land cover, the majority statistic function was used to identify the dominant categorical class within a single slope unit. The complete process for generating the data matrix is shown in Fig 5. Although the variable layers had various spatial resolutions, resampling was unnecessary, as the analysis was conducted at the slope unit level rather than the pixel level.

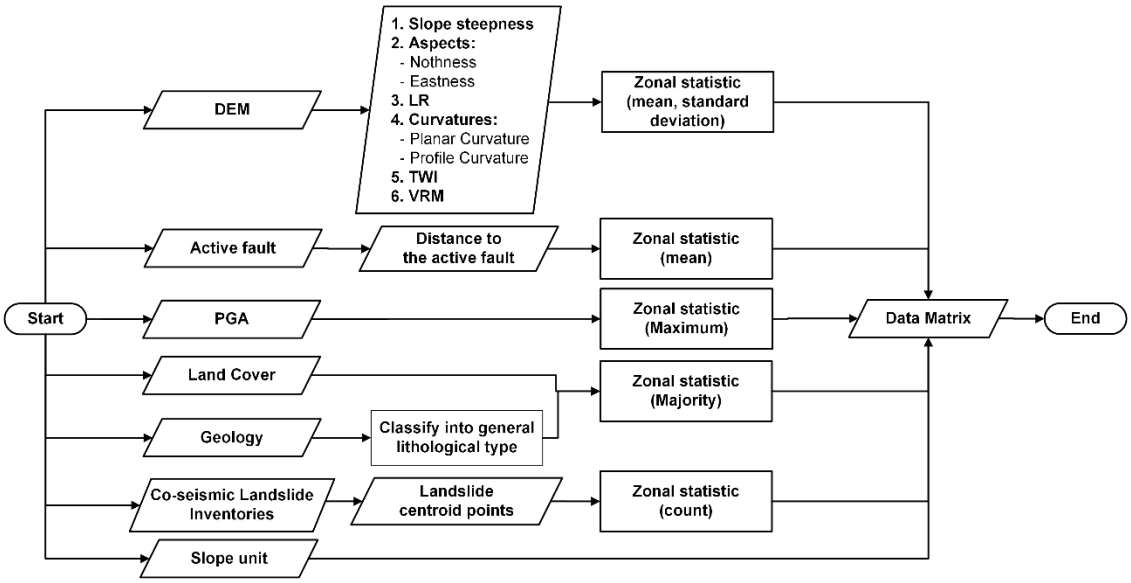

Fig 5 The flowchart illustrates the data matrix development process, detailing each step involved in extracting parameter values and assigning them to slope units.

3.2. Landslide Prediction Model with GAM

This study adopted the Generalized Additive Model (GAM) framework to build the co-seismic landslide model. GAM is an extension of the classic linear model which allows the model to predict both linear and non-linear relationships between the predictors and response variables, making it more flexible and useful for a data-driven model (Moreno et al., 2023). Additionally, it can handle various types of covariates, including continuous and categorical variables, using smooth functions or splines (Wood & Augustin, 2002).

In this study, the Bayesian version of GAMs is applied using the Integrated Nested Laplace Approximation (INLA) approach (Rue et al., 2009). The GAM was implemented as a binomial family and logit link due to the binarized setup of the response variable. This method allows the model to estimate the model parameters and their uncertainty efficiently.

Several steps were performed to develop the co-seismic landslide model, including the pre-processing and exploratory analysis, model configuration, model evaluation, and model extraction. A detailed explanation of each step is provided in Sections 3.2.1 to 3.2.4. The complete framework of the model is illustrated in Fig 6.

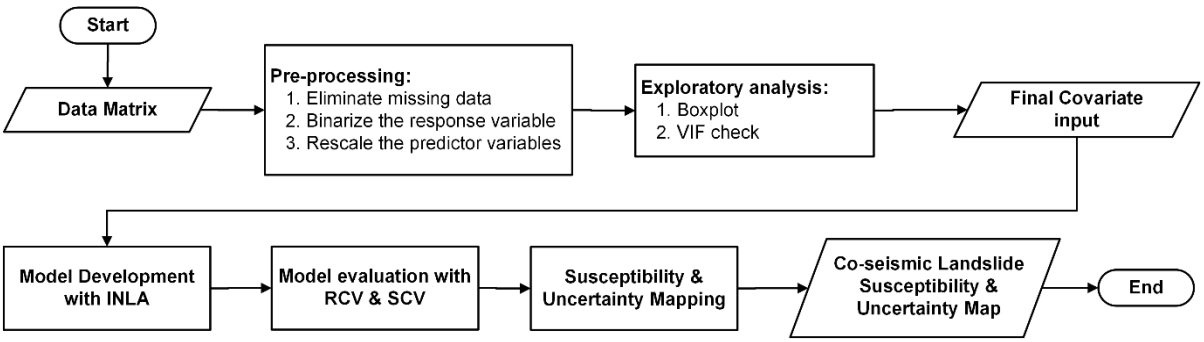

Fig 6 The flowchart illustrates the co-seismic susceptibility development process, including the preprocessing process, exploratory analysis, model development, model evaluation, and susceptibility & uncertainty mapping

3.2.1. Data preprocessing and exploratory analysis

Prior to modeling, the dataset underwent several pre-processing steps. First, all slope units with missing values (NA) were removed from the dataset to avoid errors caused by miscalculations during the modeling process. Then, the landslide occurrence was binarized using a presence and absence setup, where 1 indicates landslide and 0 indicates no landslide. Continuous variables were rescaled using mean-zero and unit variance to ensure comparability across scales and improve the model convergence.

An exploratory analysis was conducted to support the covariate selection of the continuous variables, including boxplot and Variance Inflation Factor (VIF). Boxplot helps to visualize the distribution of each variable, roughly describing how each variable might influence the landslide occurrence. VIF was calculated to check the multicollinearity between variables, where a value higher than 10 was considered a high multicollinearity, and the value below was considered acceptable.

3.2.2. Model Development

Covariate regression using INLA was conducted as an exploratory nonlinear model. This is the final filter of the covariate selection process. Each predictor was modeled individually against the response variable to see how it affected the landslide occurrence. Only the variables that show a clear and meaningful pattern were kept for the final model. The selected predictor variables were then used to build the final GAM model using the INLA package in R. The GAM was constructed with the following general formulation:

$$\eta(P) = \beta_0 + f_{slope}(z_{slope}) + f_{LR}(z_{LR}) + f_{fprox}(z_{fprox}) + f_{PGA}(z_{PGA}) + f_{lithology} + f_{landCover}$$

Where $\eta(P)$ is the logit-transformed probability of landslide occurrence, $f_x(z_x)$ represent the smooth function of each continuous variable and f_x is the categorical effect modeled as independently and identically distributed (iid). Continuous predictors were modeled using smooth functions to allow for non-linear relationships, while lithology and land cover were used as fixed categorical effects. The outcome is modeled as Bernoulli probability distribution, which fits the binary nature of the response variable.

3.2.3. Model Evaluation

The model performance was evaluated using Random Cross-validation (RCV) and Spatial cross-validation (SCV). These methods were implemented using caret and sperrorest packages R respectively (Kuhn, 2008; Brenning, 2012) and run repetitively for 10 folds. The RCV was built using createfold(), which allows it to randomly split the dataset into k folds. Each fold is used once as the test, by setting the data as NA, while the rest are used to predict the model. The predicted probabilities from the training dataset were then compared to the actual labels in the test fold using the Receiver Operating Characteristic (ROC) curve. The Area Under the Curve (AUC) was calculated using the pROC package (Robin et al., 2011) simultaneously during this process. This process was repeated across all folds, and the mean of AUC values was reported to summarize overall performance. The RCV method assesses how well the model can predict when the train and test data are spatially mixed. It provides a general overview of model accuracy but may have a bias due to its spatial autocorrelation, making it overestimate the performance (Valavi et al., 2019).

On the other hand, SCV was generalized by spatially clustering the dataset using k-means clustering based on the slope unit's centroid coordinates. The outcomes were used as spatial folds, where slope units in one geographic region were held out for testing while the remaining clusters were used for training. This approach helps to address the optimistic bias of the RCV method (Valavi et al., 2019). Combining both RCV and SCV performance evaluation will ensure a robust assessment of the model's ability to predict the unseen data, especially in a spatial context where autocorrelation may bias model performance (Ahmed et al., 2023; Moreno et al., 2023).

3.2.4. Susceptibility and Uncertainty Mapping

After model validation, the fitted GAM was used to generate national-scale landslide susceptibility maps. The maps represent the mean predicted landslide probability for each slope unit. Alongside susceptibility, uncertainty maps were also generated using the 95% credible interval of the predicted probabilities. The uncertainty was calculated as the range between the 2.5th and 97.5th percentiles of the predicted posterior distribution. These maps provide both a quantitative estimate of landslide probability and confidence in each prediction, which is essential for informed interpretation and decision-making.

3.3. Model Simulation

To assess how the co-seismic landslide susceptibility model varies under different seismic hazard levels, the validated model was simulated and projected for the whole of Türkiye. In the simulation setup, all other covariates were kept constant using values from the national-scale dataset. Only the PGA variable was changed for each simulation. Four different PGA values were substituted to the model based on the exceedance probability derived from Türkiye's national seismic hazard map. These scenarios correspond to 2%, 10%, 50%, and 68% exceedance probabilities in 50 years, which represent the earthquake intensities from the rarest to the most frequent events. This substitution allowed a controlled analysis of how landslide susceptibility shifts under varying levels of seismic input.

In the simulation, a combined dataset was constructed by merging the training data and simulation data into a single data frame. Each subset was labeled according to its respective PGA exceedance scenario (2%, 10%, 50%, and 68%) and associated with a "Source" identifier. The INLA model was fit using a binomial likelihood with a logit link function. The model was implemented using the inla.posterior.sample function, with computation configured to include posterior mean estimates of susceptibility. The output of the simulation includes the mean probabilities and the credible interval for each slope unit under four PGA scenarios, which represent the predicted susceptibility under different levels of earthquake intensities. Finally, to give spatial understanding, the outputs were extracted and mapped for each PGA scenario, resulting in national-scale susceptibility maps.

3.4. Exposure

Exposure analysis was performed to measure the potential consequences of each earthquake-induced landslide scenario. It was conducted by intersecting selected EaRs to each susceptibility and uncertainty map and quantifying the potential damage under four seismic scenarios. Prior to the overlaying process, both landslide susceptibility and uncertainty outputs were reclassified into categorical classes using quantile classification. The classification process was carried out using the Arcpy library within a Python script in ArcGIS Pro. This process divided both susceptibility and uncertainty automatically into four categorical classes, including very low (VL), low (L), moderate (M), and high (H), making them uniform, more interpretable, and easier to combine. Combining these two dimensions ensures that the exposure metrics reflect both the intensity and reliability of the hazard estimation.

The reclassified susceptibility and uncertainty maps for each seismic hazard scenario were then spatially overlaid with the EaR layers using ArcGIS Pro. The overlay process was carried out separately for each scenario. The exposed EaR is then quantified within each combination class by calculating the total length, area, or count, depending on the EaR type mentioned in Section 2.5.

4. RESULTS

This chapter presents the results of the modeling and discusses the implications of the findings. Section 4.1 explores the statistical distribution and correlations of the parameters through exploratory data analysis. Section 4.2 presents the results of the co-seismic landslide model and interprets the effect of each variable. Section 4.3 evaluates the national-scale susceptibility maps generated through scenario-based simulation using varying PGA inputs. Lastly, Section 4.4 discusses the spatial distribution of earthquake-induced landslide exposure and compares the impact across multiple hazard scenarios.

4.1. Exploratory Analysis of the Parameters

As mentioned in Section 3.4, an exploratory analysis was conducted prior to the modeling process to determine which predictor variable should be used as predictor variables based on their contribution to landslide occurrence and their potential collinearity. The exploratory analysis involved assessing the distribution of the parameters through boxplots and checking for collinearity among variables. This process only examines the continuous predictors such as slope steepness, LR, proximity to the active fault, and PGA. Detailed outcomes of each step are presented sequentially in Sections 4.1.1 to 4.1.2.

4.1.1. Boxplot

Boxplots were used to visually assess and compare the distribution of predictor variables between the binarized landslide occurrence, which was encoded as 0 (no landslide) and 1 (landslide). The boxplot showed the central tendency of the parameters through its median and interquartile range, while the outliers, the whiskers, and the box represent the general spread of the data. It provided some insight into how each variable might influence the landslide occurrence. The boxplot of the predictor variables observed in this research is shown in Fig 7.

Typically, significant differences in the median values between groups and minimum overlap between boxes indicate a significant influence of the parameters on the landslide occurrence. Several parameters presented clear differences in the median values, such as slope, LR, VRM, proximity to the active fault (fprox), and PGA, which indicate a potential relevance to landslide occurrence. Higher median values of the predictor variable in areas that experience landslides indicate that the parameters tend to correlate positively with the landslide occurrence, suggesting that increased values contribute to a higher potential of slope failure. This pattern is clearly seen in the slope steepness, LR, VRM, and PGA. On the contrary, lower median values correspond to lower susceptibility. An inverse relationship is observed in proximity to the active fault and rainfall, where the lower value contributes to the landslide occurrences.

The remaining parameters, including eastness, northness, profile curvature, and planar curvature, showed minimal differences in median value between the landslide and no-landslide groups. Their boxplots significantly overlap, making it hard to distinguish the data distribution between the groups. Additionally, these variables contain numerous outliers, which may indicate specific localized parameter conditions. This pattern suggests that both the aspects and curvature parameters have a weaker influence on the landslide occurrence.

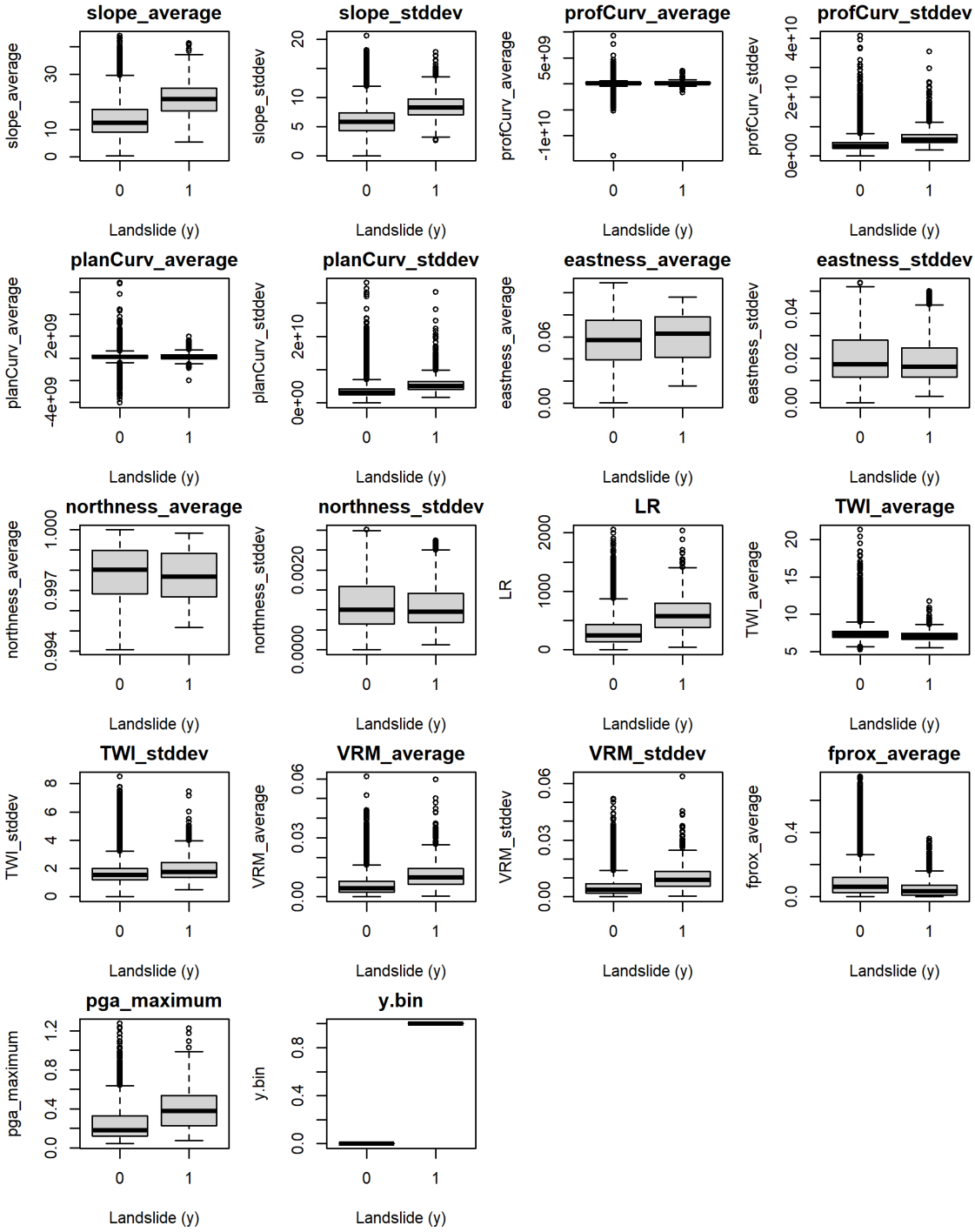

Fig 7 Boxplot of each predictor variable against the landslide occurrence. 0 value means no landslide, and 1 means landslide.

4.1.2. Collinearity Check with VIF

A Variance Inflation Factor (VIF) was performed to quantitatively assess the collinearity among the predictor variables. VIF value measures how much the variance of coefficient regression increases due to collinearity with other variables. The higher the VIF, the more the variable is correlated with others, which makes it hard to ensure its individual effect. Generally, a VIF value higher than 10 is considered high multicollinearity and will considered to be removed, while the collinearity value between 5 and 10 indicates moderate collinearity, which needs additional analysis before removal (Kutner et al., 2004). The VIF value of each parameter is displayed in Table 3.

Table 3 VIF value of each predictor variable.

Variables	VIF Value	Label
Slope average	10.86	High collinearity
Slope stddev	3.16	Acceptable
Profile curvature average	1.28	Acceptable
Profile curvature stddev	9.86	Moderate collinearity
Planar Curvature average	1.18	Acceptable
Planar Curvature stddev	10.34	High collinearity
Eastness average	40.44	High collinearity
Eastness stddev	37.12	High collinearity
Northness average	41.20	High collinearity
Northness stddev	36.23	High collinearity
LR	3.45	Acceptable
TWI average	3.12	Acceptable
TWI stddev	2.64	Acceptable
VRM average	10.16	High collinearity
VRM stddev	7.63	Moderate collinearity
Proximity to fault	1.19	Acceptable
PGA	1.10	Acceptable

The VIF result shows that some variable exceeds the acceptance threshold, including planar curvature stddev, the aspect variables, and the VRM average. Several variables have moderate collinearity, including the standard deviation of profile curvature and VRM. Although slope steepness is the most important variable for landslide prediction, its high VIF value became a concern. However, removing one of the slope steepness variables might help reduce the VIF value. Therefore, the slope steepness standard deviation will be removed to improve the VIF value of the slope steepness average.

4.2. Co-seismic Landslide Model

This section presents the modeling phase of this research, which includes the development of the co-seismic landslide model, performance evaluation, and model simulation. The model was constructed based on categorical predictors and selected continuous predictor variables as an outcome from the covariate regression (4.2.1) in combination with section 4.1. GAM was utilized to capture the non-linear relationships between predictors and landslide occurrence. The model was simulated in 4 scenarios to predict the earthquake-induced landslide in Türkiye. Detailed outcomes of each step are presented sequentially in Sections 4.2.1 to 4.2.4.

4.2.1. Covariate Regression

To assess the importance of each predictor variable, Covariate regression analysis was conducted. In this step, each predictor was individually regressed against the binary landslide as the response variable to evaluate their relationships. The regression coefficient plots of each variable are presented in Fig 8. The plots help to visualize the influence of each variable and its relationship behavior. In each plot, the solid line represents the estimated mean effect of the covariate, while the dashed lines indicate the 95% credible intervals.

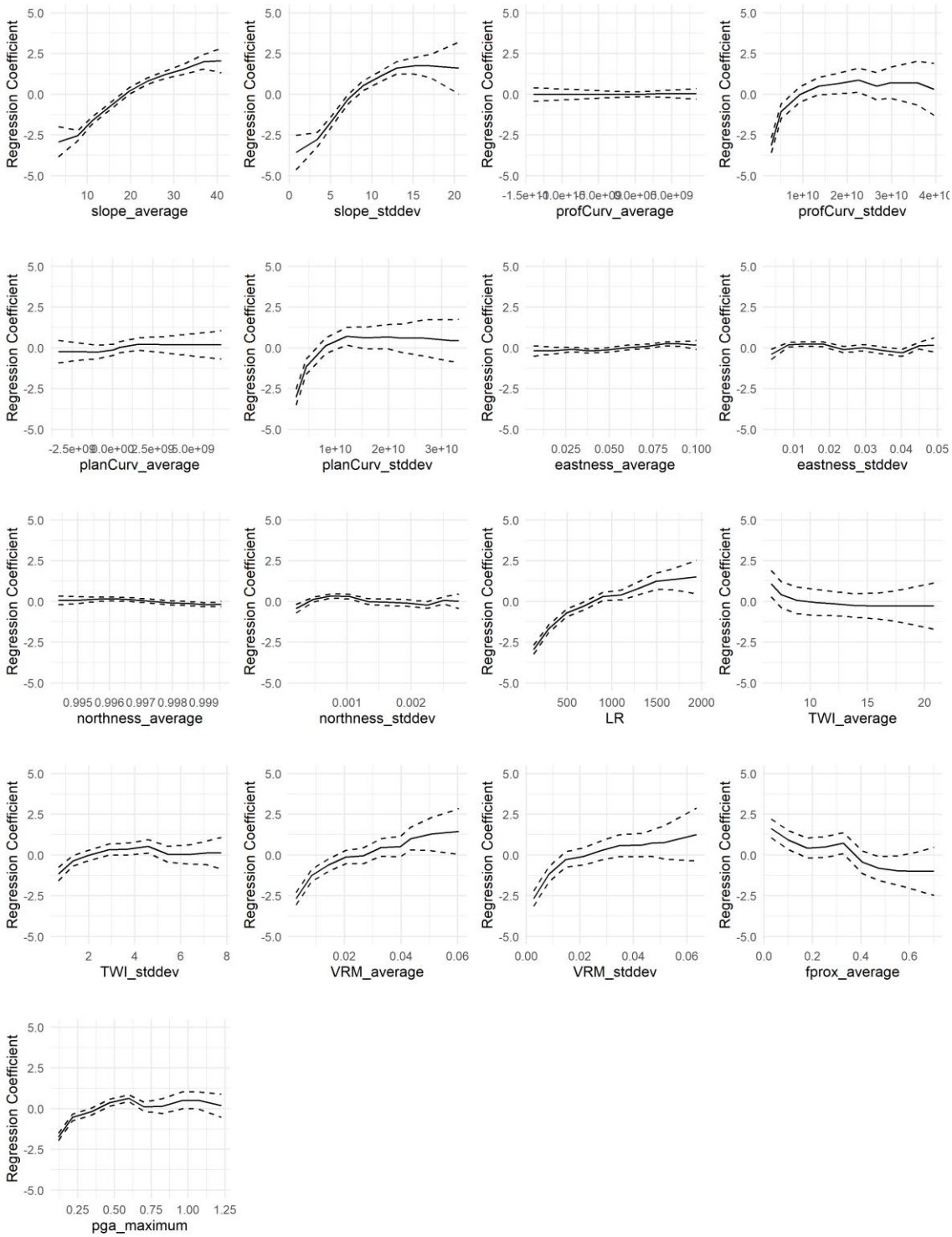

Fig 8 Covariate regression of the predictor variables against the response variable. X-axis values show the predictor value, while the Y-axis represents the regression coefficient. The mean regression coefficient is shown by the middle solid line, meanwhile, the upper and lower dashed lines indicate the confidence interval.

Several predictors on the plot show a strong positive trend, with extremely narrow confidence intervals, including slope, LR, and PGA, indicating high certainty in their positive trend. Even though the VRMs have similar upward trends, they exhibit a wider credible interval and more curved response lines. The positive trend observed across these variables indicates a likely contribution to higher landslide probability, while the

width of the credible intervals reflects the degree of certainty in how strongly the predictor affects the landslide occurrence.

Conversely, the proximity to the active fault shows a mild decreasing trend with a wide credible interval range, which indicates a negative influence on the landslide occurrence, although the relationship is relatively weak. In contrast, the remaining predictors, including the curvatures, aspect variables, and TWIs, show flat-shaped response lines centered around zero. This indicates no meaningful relationship between the predictors with the landslide occurrence and suggests that there is no significant contribution of these variables.

Combining the analysis with other exploratory plots, it can be concluded that slope steepness, LR, and PGA are the variables that have a strongly significant relationship to the landslide occurrence. Additionally, there is no indication of multicollinearity between variables, which would minimize the redundancy within the model. Another variable considered as a consistent input for the model is proximity to the active fault, which, although it has a weaker influence on the landslide, theoretically has significance for earthquake-induced landslide events. Therefore, keeping this variable expected will give an insight into the model.

Although they show a relatively positive influence on the landslide probability, VRMs are removed from the model. These variables were removed due to their potential multicollinearity, which potentially caused redundancy. On the contrary, the unclear relationship shown by the TWIs, aspects, and curvature variables supported the former exploratory methods and strengthened the removal decision of these parameters.

In conclusion, the continuous variables selected as inputs for the final model are slope steepness average, LR, PGA, and proximity to fault. These variables are modeled using a non-linear approach through GAM due to their skewed distribution and to more effectively capture complex patterns within the dataset. On the other hand, categorical variables, including lithology and land cover, were not included in the exploratory plots. Instead, they will be directly evaluated on the final model.

4.2.2. Final Model Development

The model was developed using a random walk (rw) structure to capture the nonlinear relationships between continuous predictor variables and the response variable. In contrast, categorical variables were modeled using an independent and identically distributed (iid) structure, allowing each class to be estimated independently without assuming any order or trend among them. The marginal effect plots shown in Fig 9 illustrate the individual contribution of each predictor variable to the landslide prediction that is captured and estimated by the GAM. They show the estimated effect of each predictor on the log odds of landslide probability. The continuous predictor variables are represented by the solid regression line with the dashed lines indicating the 95% confidence interval, while the categorical effect is represented using point estimates with error bars. Both illustrate the posterior mean and the credible intervals, giving insight into the estimated effect and the uncertainty of each predictor.

Most of the continuous variables show similar behavior to the plot in Section 4.2.1. Covariate Regression, slope steepness, LR, and PGA exhibit an increasing non-linear regression line with a narrow confidence interval. These predictors' regression coefficient plots indicate a strong positive non-linear relationship with the landslide probability and a high level of confidence in their relationship. This outcome aligns with theoretical expectations, as theoretically, the slope steepness and LR are contributors to landslide occurrence, while PGA is the triggering factor for earthquake-induced landslides.

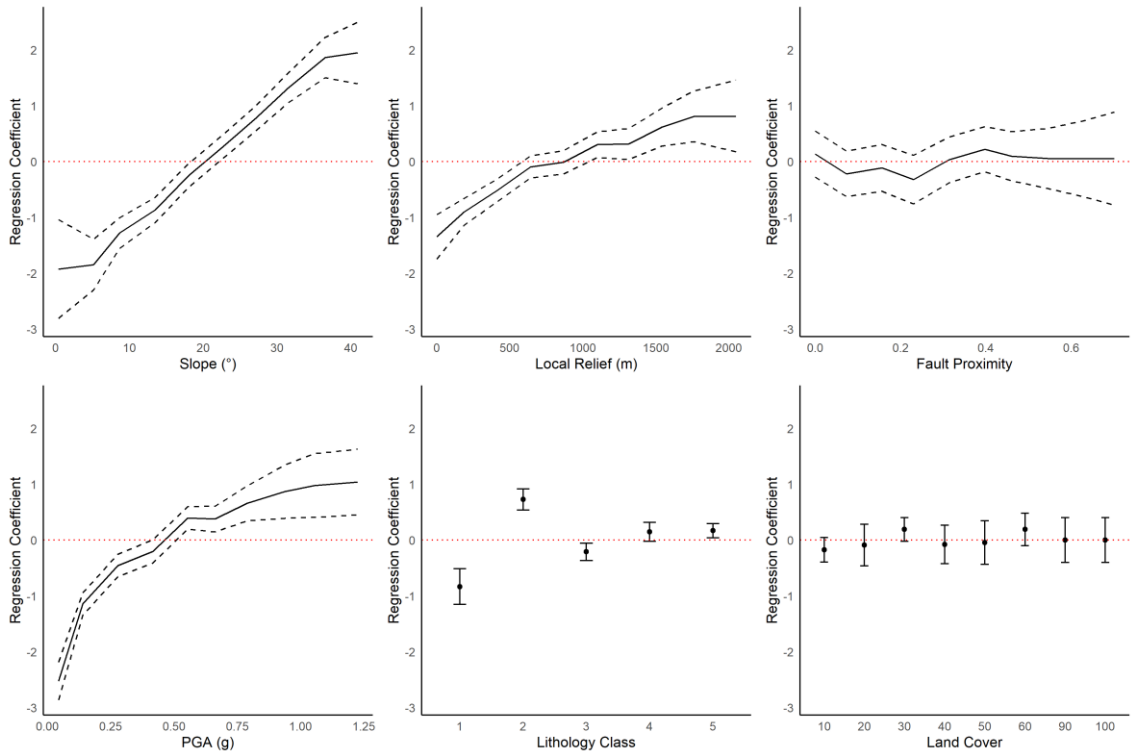

Fig 9 Marginal effect plots of the predictor variable input in GAM. The continuous predictors are treated as non-linear smooth functions while the categorical treated as fixed effects. A positive coefficient indicates a higher contribution to the landslide probability.

However, unlike other predictors, proximity to the active fault shows a relatively flat trend with a narrow confidence interval. Although this variable was theoretically expected to have a negative influence on landslide occurrence, the flat trend suggests that changes in proximity do not significantly affect the predicted landslide probability. The narrow confidence interval reflects that the model is confident in this assessment.

As categorical predictors, both lithology and land cover consist of multiple classes, as previously described in Section 2.3 (Controlling Parameters). However, only a few of these classes showed a notable influence on the model. The class is considered to have a positive influence on landslide probability if its estimated effect lies above the zero mean line, and a negative influence if it lies below. The vertical error bars represent uncertainty around each estimate and function similarly to credible intervals. Shorter bars indicate greater certainty in the estimated effect, while longer bars suggest higher uncertainty.

Among the five lithology classes, Class 2 (volcanic) and 5 (sediment) showed a clear positive influence on the landslide occurrence as indicated by their positive model estimates and relatively narrow error bars, reflecting high confidence in their contribution. Although slightly crossing the zero line, class 4 (ophiolitic) exhibited a positive estimate point and narrow error bar, indicating high confidence and positive influence on the landslide occurrence. Class 1 (plutonic) and Class 3 (metamorphic) showed negative effects, but only Class 3 presents a narrow error bar, suggesting greater certainty in its negative contribution. In contrast, the estimate for Class 1 had a wide error bar, indicating high uncertainty.

As shown in Fig. 2, although both the 2011 and 2023 co-seismic landslide inventories span all five lithological classes, the proportion of each class varies across the two earthquake-affected regions. These spatial differences likely influence the overall predictive strength and consistency of each lithological class

in the model. Nevertheless, the marginal effect plots suggest consistent and confident effects across lithological classes, regardless of their regional distribution.

Opposite to lithology, all land cover classes had estimated effects that crossed the zero line, indicating a statistically insignificant influence on landslide occurrence. However, some of them still show visible trends. For example, land cover class 10 (tree cover) showed a tendency towards a negative effect, while class 30 (grassland) and 60 (bare land) exhibited a positive trend. These results align with theoretical expectations, where the presence of tree cover is known to enhance slope stability by reinforcing soil and reducing surface runoff, whereas grassland and bare land lack such protective vegetation, increasing the likelihood of slope failure.

The relationship between predictors and landslide occurrence is supported by the random effect values presented in Appendix A.2. These random effects are derived from the posterior distribution and reflect the model's ability to adjust the prediction baseline for different groups of predictors by accounting for local conditions. Each random effect comes with a range of likely values, where the posterior mean represents the average estimated effect, and the deviation between the confidence intervals reflects the level of uncertainty.

The random effects provide a detailed understanding of how each predictor influences landslide occurrence across its range of categories. Continuous predictors such as slope steepness, local relief, and PGA show clear increasing trends across their ranges, with the means rising from negative to positive values. These patterns, combined with small deviation values, indicate a strong and confident positive influence on landslide probability. In contrast, proximity to fault exhibits a nearly flat trend around zero with narrow intervals across all bins, suggesting that this variable has no significant effect in the current model.

4.2.3. Performance Evaluation

The model performance was evaluated using the ROC curve, which illustrates the balance between the true positive (sensitivity) and false positive (1-specificity) rate of landslide occurrence. The closer the curve is to the top-left corner of the graph indicates a better model performance, while the closer it is to the midline shows the opposite. It is stated as an AUC value that ranges from 0 to 1. The closer the AUC value is to 1, the better the prediction. On the other hand, a value of 0.5 suggests a random prediction.

As mentioned in Section 3.2 (Landslide Prediction Model with GAM), this study utilized both RCV and SCV techniques to evaluate the model's performance. RCV was used to assess how well the model fits the training data through random sampling, while SCV assessed the model's ability to generalize to spatially independent regions. The spatial distribution of the data splits for each method is visualized in Appendix A.3, and the resulting ROC curves are presented in Fig 10.

The RCV gained a mean AUC of 0.86, suggesting that the model performs very well when the data is randomly divided into training and test data. On the other hand, the SCV achieved a slightly lower mean AUC value of 0.81. This might be due to the difficulty of generating accurate predictions in a completely different area of training and test data. The RCV has a tiny confidence interval, presented as the shaded area, which indicates a small uncertainty in the model's prediction when tested on the random split dataset. Compared to the RCV, the SCV curve has a wider shaded area, which suggests more uncertainty when the model is applied to spatially independent test data. However, the AUC of the SCV remains within an acceptable range to confirm that the model performs well and can make reliable predictions in completely different areas. The relatively high AUC values from both methods show that the chosen input variables and model structure are reliable. The SCV result, in particular, suggests that the input data is general enough

and that the model is not overfitting to specific locations, meaning it can still make good predictions in areas it hasn't trained before.

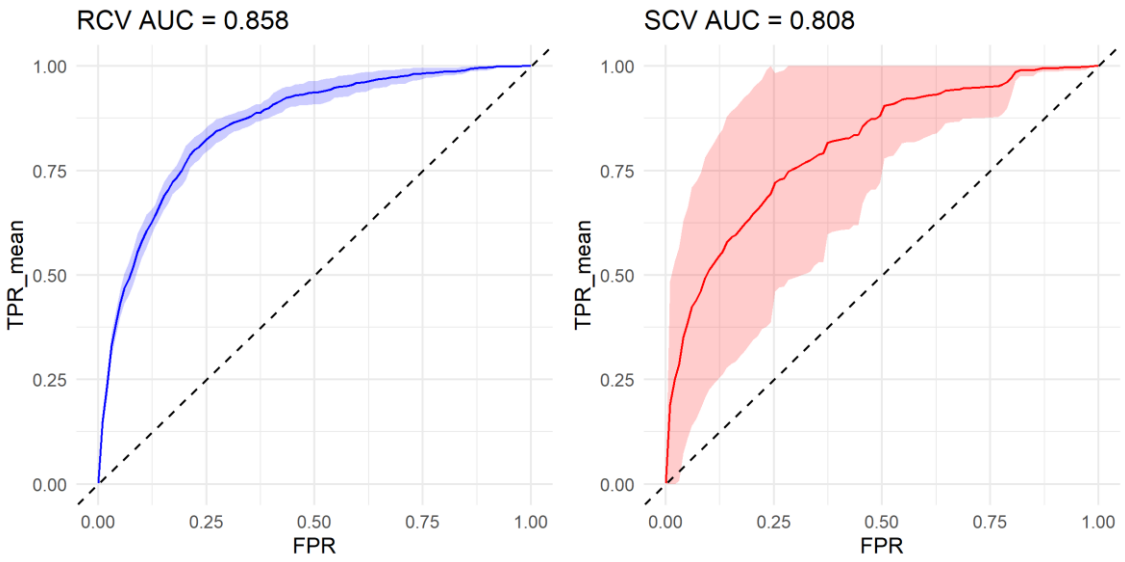

Fig 10 10-fold ROC curve of the RCV (blue, left) and SCV (red, left) technique with the corresponding mean AUC values.

To further evaluate the model performance, confusion maps were created for both RCV and SCV predictions (Fig 11), which spatially displayed the true positive (TP), true negative (TN), false positive (FP), and false negative (FN). To classify the continuous predicted probabilities of each evaluation method into binary outcomes (landslide/no landslide), the Youden Index was applied to determine the optimal threshold. The Youden Index selects the threshold that maximizes the sum of sensitivity and specificity, providing an optimal cut-point that balances true positive and true negative rates for effective classification (Youden, 1950; Luo & and Xiong, 2013).

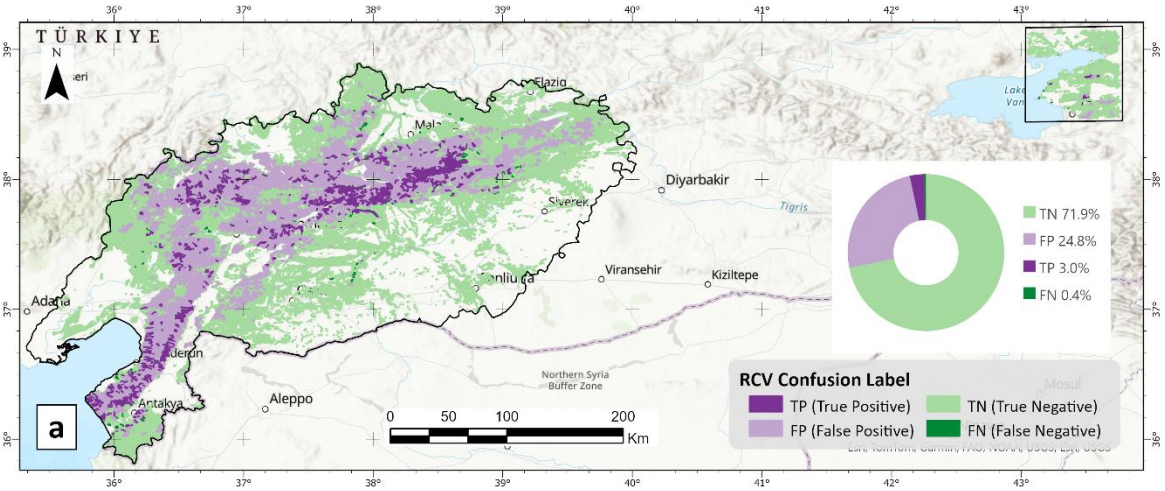

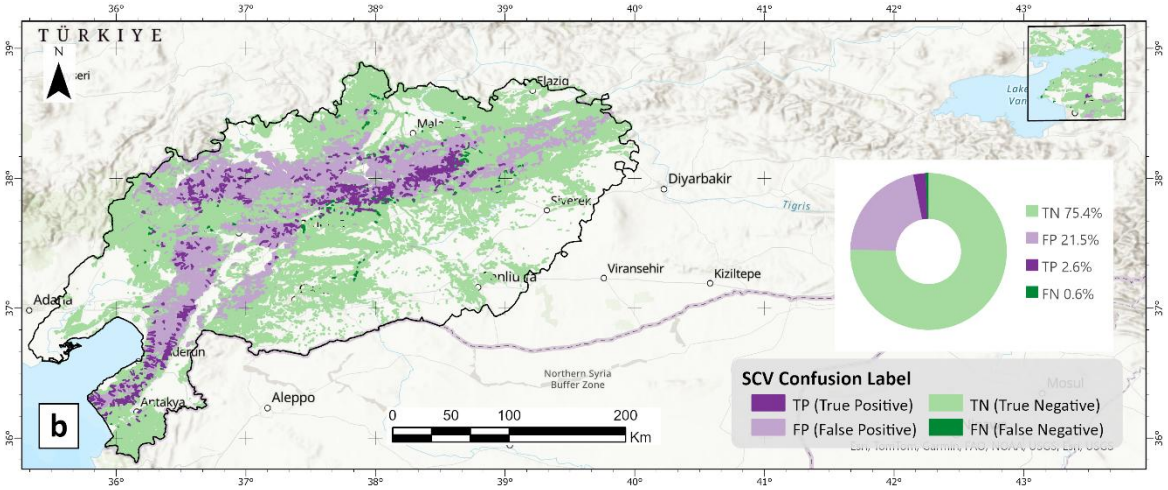

Fig 11 The confusion map of RCV (a) and SCV(b) methods to enhance the ROC and AUC findings.

The SCV confusion map showed a slightly lower TP compared to the RCV. This might be due to the weaker prediction ability, expressed by the lower AUC value of the SCV test. Even so, the overall result and pattern remain consistent. In both cases, TN dominates the study area, reflecting a high number of correctly identified no-landslide slope units. In contrast, FN is the least appear on the map. The presence of FP is concentrated near the high susceptibility zones, which may reflect the area with a high chance of landslide occurrence due to the covariates, despite there being no landslide recorded yet. The spatial distribution of FP illustrated in Fig 11 indicates the model's tendency to overestimate landslide susceptibility in some areas.

4.2.4. Susceptibility Maps

The final landslide susceptibility map was made to verify the spatial distribution of landslide susceptibility based on the combined 2011 and 2023 co-seismic landslide inventory. The mean probability of the fitted values from the GAM model was assigned to each slope unit and visualized continuously with a green-to-red color scale to spatially present susceptibility, as shown in Fig. 12. The green indicates low mean probability, and the red color tells the opposite. Meanwhile, the orange to red color indicates a moderate mean probability value.

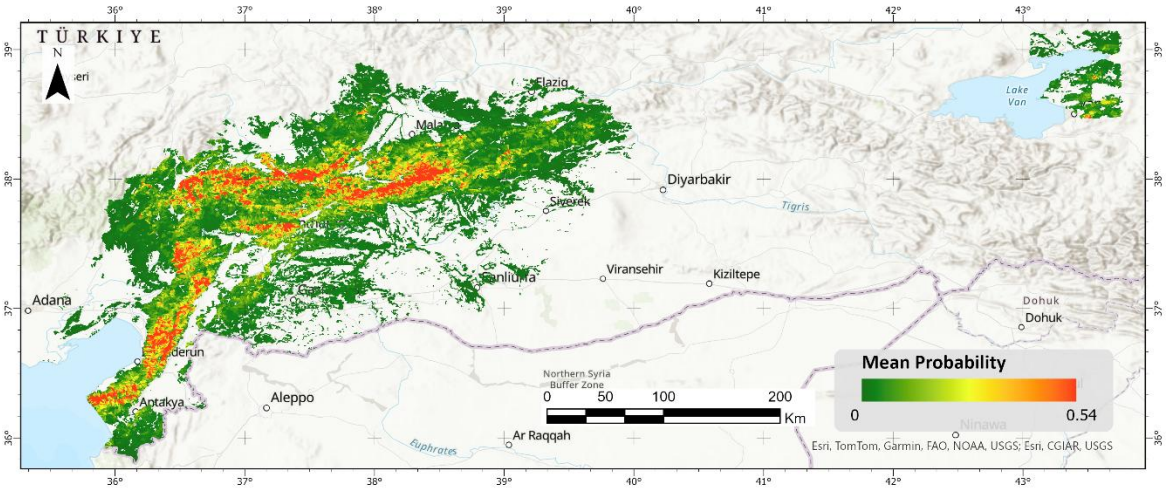

Fig 12 Landslide Susceptibility Map based on co-seismic landslide inventory of 2011 and 2023 earthquake events in Türkiye.

Most of the slope units are colored green, reflecting the lower susceptibility. This dominance of low values suggests the generally stable conditions of many slope units across the study area, particularly in the relatively flatter areas. On the contrary, the susceptibility map highlights clear spatial trends of high-probability zones

with the red color, which are concentrated near the steep topographic regions and fault rupture zones, especially those affected by the 2023 Kahramanmaraş and 2011 Van earthquakes.

To complement the susceptibility map, an uncertainty map was made to visualize the prediction confidence of the model. It was derived from the difference between the 97.5% and 2.5% quantiles of the fitted values for each slope unit. The map and the uncertainty plot are shown in Fig 13. The uncertainty values are illustrated continuously with a greyish-blue-to-yellow color scale. Slope units with lower uncertainty appear in a greyish-blue color, indicating that the model has higher confidence in its predictions for those units. On the other hand, the yellow color marks higher uncertainty.

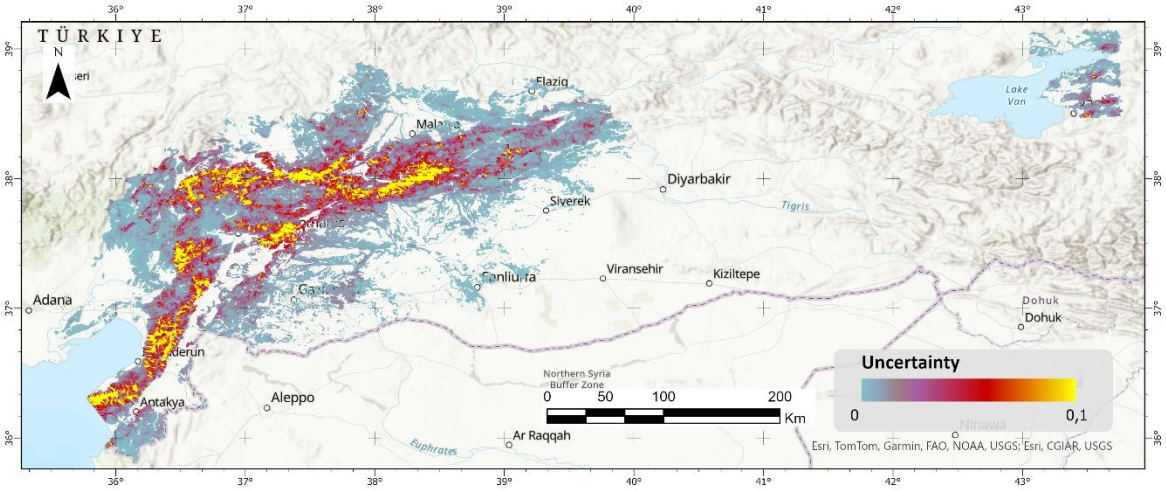

Fig 13 Landslide uncertainty map of the co-seismic landslide susceptibility model.

Overall, the uncertainty map had a similar pattern to the susceptibility map, where the orange to yellow color concentrated in the steep zone, particularly near the rupture line. This indicates that slope units with higher susceptibility values most likely have quite a big uncertainty as well, suggesting that the model is less certain about the prediction. However, the uncertainty pattern doesn't always follow the susceptibility values. Some areas with high mean probability may still have low uncertainty, suggesting high confidence in their prediction. Combining both susceptibility and uncertainty maps provides an extensive view of potential hazards, as the uncertainty map adds a layer of interpretability and further investigation.

4.3. Model Simulation

To assess future landslide susceptibility under different seismic scenarios, the final landslide susceptibility model was simulated using four PGA exceedance probability scenarios over 50 years. This section presents the outcome of the simulation phase of this research, including the landslide susceptibility and uncertainty of each scenario and the susceptibility difference between scenarios. Detailed descriptions are presented sequentially in Sections 4.3.1 and 4.3.2.

4.3.1. Landslide Susceptibility under different seismic hazard scenarios

A spatial simulation was conducted to predict earthquake-induced landslide susceptibility across the entire Türkiye under four seismic hazard scenarios based on the 2%, 10%, 50%, and 68% PGA exceedance probability in 50 years. These scenarios represent different chances of an earthquake happening. The 2% exceedance means a very strong earthquake but is rare, while the 68% tells the opposite. The outcome of the simulation is presented as the landslide susceptibility maps, which are shown in Appendix A.4, except for the 68% scenario in Fig 14.

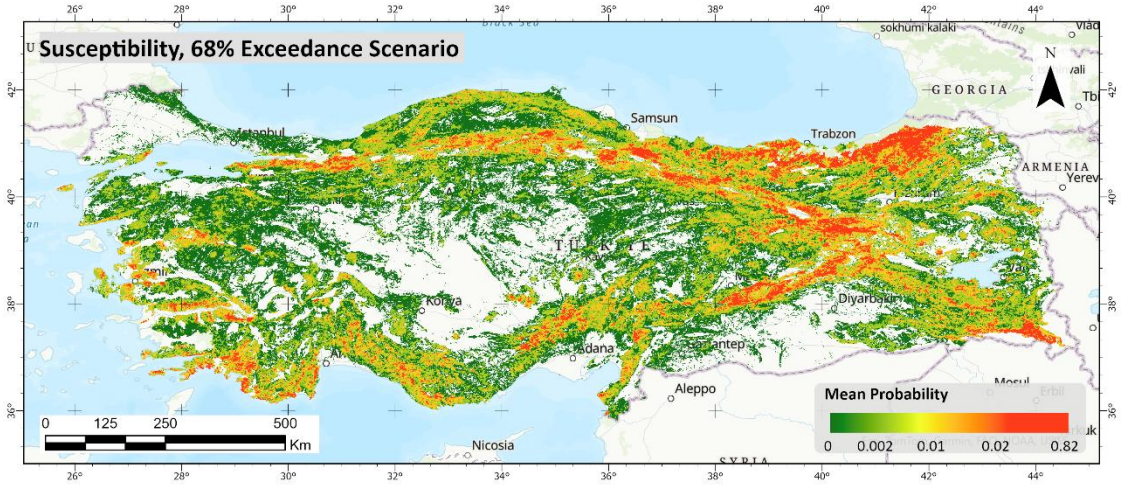

Fig 14 Earthquake-induced landslide susceptibility maps for 68% PGA exceedance probability in 50 years.

The susceptibility values derived from mean probability are illustrated in a uniform green-to-red color scale, ranging from 0 to 0.82 across all scenarios. Focusing on the 68% scenario, the susceptibility value ranges from 0 to 0.3. The high susceptibility slope units, represented by the orange to red color, are primarily clustered along major fault zones and mountainous regions, particularly across northern, eastern, and southwestern Türkiye. On the contrary, the central regions are dominated by lower susceptibility slope units. Nevertheless, as shown in Appendix A.4, the other scenarios exhibit similar spatial patterns, with high-susceptibility slope units consistently clustered along the same regions. However, the susceptibility values within these slope units increase under rarer seismic scenarios. As a result, the 2% exceedance scenario demonstrates a broader extent of high susceptibility compared to the 68% scenario, indicating a heightened landslide risk under more extreme seismic events.

Besides the susceptibility map, the uncertainty map was made to complement the simulation analysis. While the susceptibility maps captured the spatial likelihood of landslide occurrence, the uncertainty maps revealed where the model is more or less confident in those predictions. The uncertainty map under the 68% scenario is displayed in Fig 15, and the rest are in Appendix A.5.

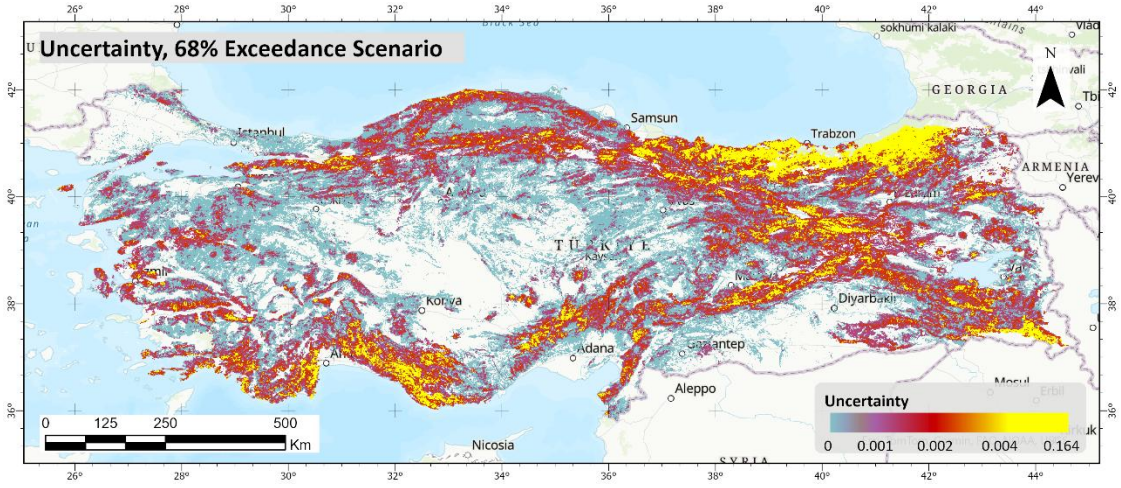

Fig 15 Earthquake-induced landslide uncertainty map for 68% PGA exceedance probability in 50 years.

The uncertainty is derived from the deviation value between the 2.5 and 95 quantiles. Similar to the susceptibility maps, the uncertainty maps are also illustrated on a uniform scale, colored greyish-blue to yellow, ranging from 0 to 0.164. The greyish-blue color represents low uncertainty, while the yellow tells the opposite. Taking a sample of the 68% scenario, the uncertainty value ranges from 0 to 0.12. The map is

dominated by a grey color, indicating that most of the slope units have low uncertainty values. Higher uncertainty values are presented as an orange-to-yellow color, which is clustered near the active faults and mountainous areas. As shown in the appendix, areas with high uncertainty are primarily concentrated near active faults and mountainous regions. However, the uncertainty values within slope units tend to increase under scenarios with lower exceedance probabilities. This is reflected by the emergence and expansion of higher-uncertainty areas, illustrated in orange-to-yellow colors in the uncertainty maps of rarer seismic scenarios.

Visual inspection of the maps reveals that high susceptibility does not always equal to high uncertainty. Some of the high probability areas (red-color slope units in the 68% scenario) show moderate to low uncertainty (greyish-blue color). This difference emphasizes the importance of reporting both maps together as the susceptibility shows where landslides are likely to occur, while uncertainty highlights how much trust can be placed in those predictions.

4.3.2. Susceptibility difference between scenarios

The susceptibility differences were made to evaluate the spatial sensitivity of various seismic scenarios. These maps were generated by subtracting the susceptibility outputs between seismic scenarios, specifically between the rarest (2%) and the most common (68%) scenarios, as well as between consecutive exceedance probabilities: 2% vs. 10%, 10% vs. 50%, and 50% vs. 68%. The difference between 2% and 68% scenarios is displayed in Fig 16, while the rest is in Appendix A.6.

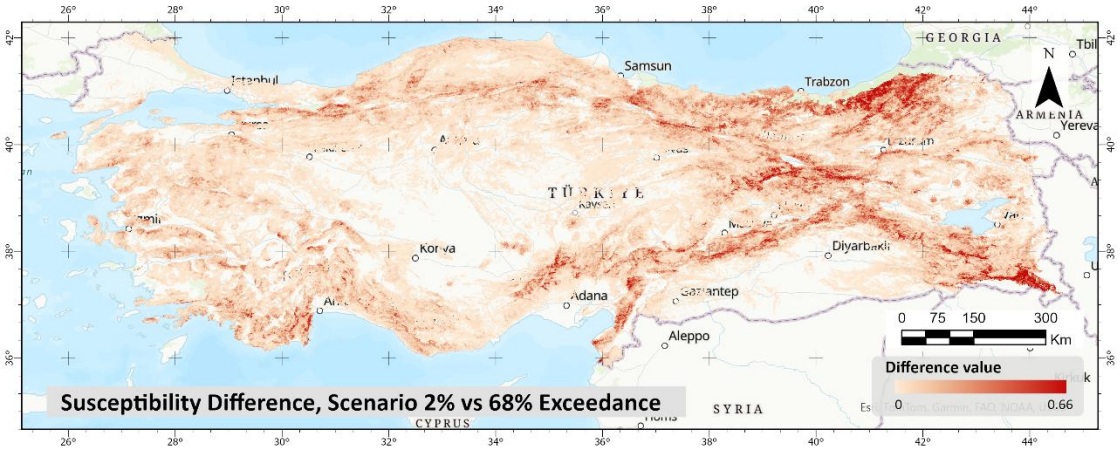

Fig 16 The susceptibility differences between the 2% and 68% scenarios indicate the model's sensitivity to the seismic level change

For comparability, the maps are displayed using a uniform color scale ranging from 0 to 0.66. The light orange color represents the minimum susceptibility difference value between scenarios, and reddish orange shows the opposite. The difference map of the 2% and 68% scenarios was dominated by a light orange color, which indicates that most of the slope units between 2% and 68% have similar susceptibility values. However, there are some high differences concentrated near the NAF and EAF areas, suggesting the susceptibility value of the 2% scenario is way higher than the 68% in a particular area.

Unlike the 2% vs 68% scenarios, the consecutive difference map showed a very limited diversity. Overall, the maps showed a relatively homogeneous light orange color across the pairs, particularly between the 50% and 68% scenarios. Although the differences are not drastic, the consecutive difference map shows a similar pattern, where the higher difference values are gathered near the active fault and mountainous area.

4.4. Earthquake-Induced Landslide Exposure

This section presents the exposure analysis of eight EaR, evaluated under four landslide susceptibility scenarios. The exposure analysis was generated by overlaying the landslide susceptibility and uncertainty with each EaR to quantify the amount of element exposed across different scenarios. Prior to this overlay, both susceptibility and uncertainty values were reclassified into four quantile-based categories. Susceptibility was categorized from very low susceptibility (VLS) to high susceptibility (HS), while uncertainty ranged from very low uncertainty (VLU) to high uncertainty (HU). This classification made it easier to combine susceptibility and uncertainty values for the exposure assessment.

Exposure analysis under different scenarios was aimed at measuring how the change in seismic scenarios could impact the infrastructure and assets across the country. In doing so, the exposure analysis can provide insight into which assets may be vulnerable under varying scenarios. Detailed outcomes of each exposure analysis are presented separately in sections 4.4.1 to 4.4.8.

4.4.1. Road Exposure

Fig 17 and 18 illustrate the exposure of Türkiye's Road network to earthquake-induced landslides under 68% seismic hazard scenarios. The exposure map displayed in Fig 17 is an example of how the EaR is overlaid with the susceptibility slope units to estimate the exposure of a certain EaR. The susceptibility is presented in green to red colors. Meanwhile, the uncertainty is presented as a transparency gradation of each slope unit, where the higher transparency means high uncertainty, and the opaque color means the opposite. The exposure map for other EaR and scenarios is provided in the appendix.

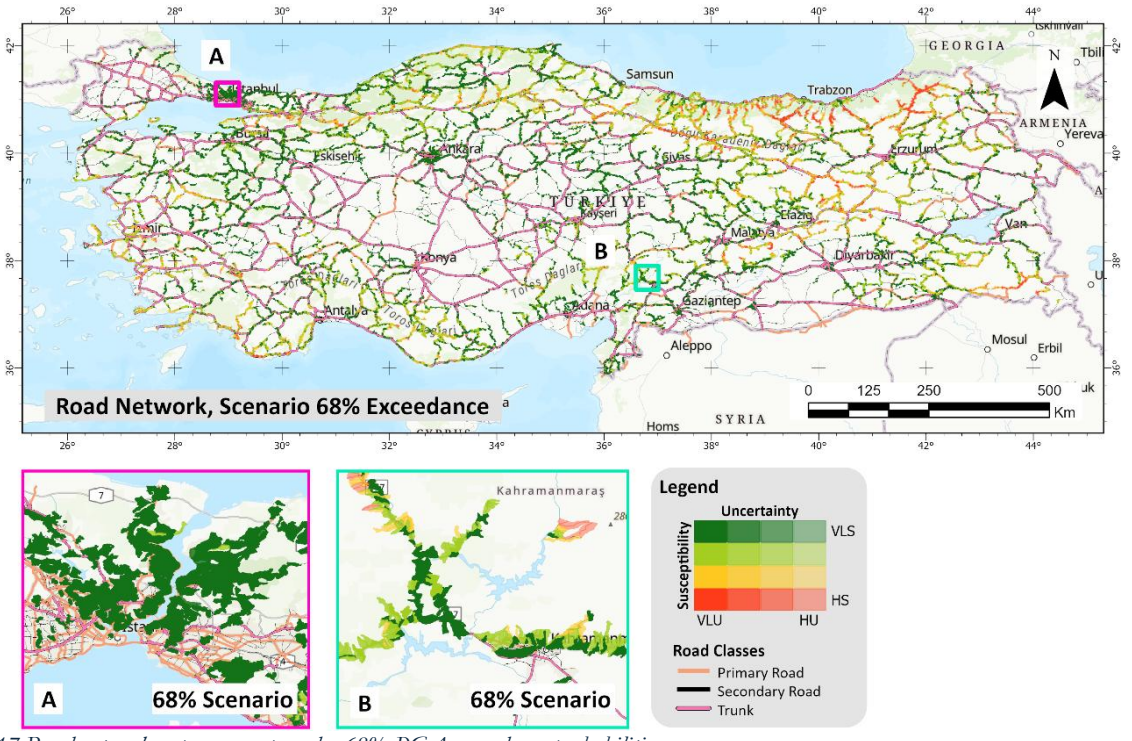

Fig 17 Road network exposure map under 68% PGA exceedance probabilities

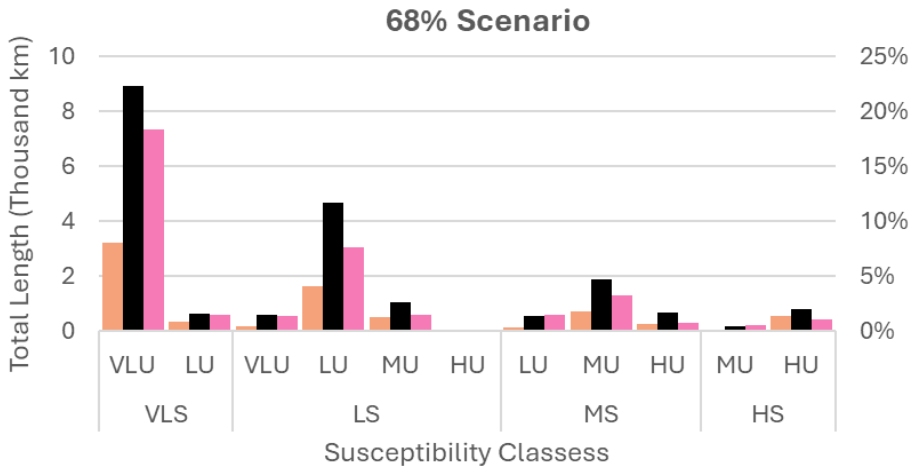

Fig 18 Road network exposure bar plots under 68% PGA exceedance probabilities.

The bars in Fig 18 represent the total length of trunk, primary, and secondary roads intersecting with each susceptibility class (VLS to HS) combined with the uncertainties (VLU to HU). The exposure is expressed in both kilometers and percentage of the length of the road network. Focusing on the 68% scenario, as the most relevant to the real condition, the majority of the road network is exposed to slope units classified as very low susceptibility-very low uncertainty (VLS-VLU), followed by low susceptibility-low uncertainty (LS-LU) and moderate susceptibility-moderate uncertainty (MS-MU). On the other hand, the amount of road exposed to high susceptibility slope units (HS-MU and HS-HU) is very limited, suggesting most of the road network is located in safe areas.

Besides the 68% scenario, other scenarios were assessed and provided in Appendix A.7. Overall, the changes in the scenario resulted in different exposure patterns on the road network. For example, opposite to the 68%, most of the roads in the 2% scenario are exposed to the HS-HU class, while their exposure to the lower susceptibility classes is limited.

Generally, the secondary roads show the highest exposure levels in every class combination, demonstrated by their highest black-colored bar in each class. In contrast, primary roads show significantly lower exposure than secondary or trunk roads across all scenarios. For example, in the VLS-VLU class, the secondary road exposure reaches more than 20% of the total length, followed by the trunk (>15%) and primary road (<10%). It reflects the spatial extent of the road class in the datasets, where the secondary road distribution dominates the dataset, followed by the trunk and primary roads.

4.4.2. Railway Exposure

Fig 19 presents the exposure of Türkiye's railway network to earthquake-induced landslide susceptibility across the 68% exceedance probability scenario. The bar graphs display the total length of railway lines intersecting with different susceptibility–uncertainty class combinations. Exposure is shown in both kilometers and as a percentage of the overall railway network.

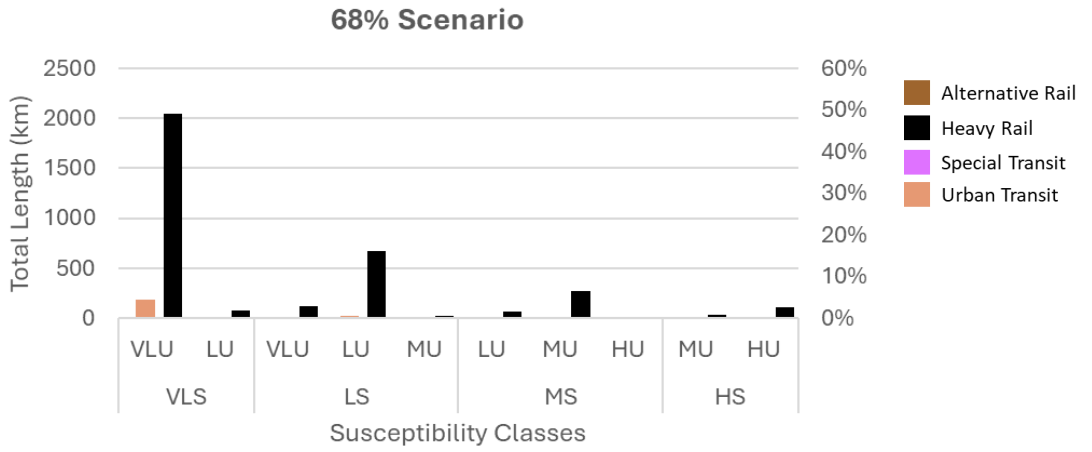

Fig 19 Railway exposure bar plots under 68% PGA exceedance probabilities.

Compared to other linear infrastructure types, railway exposure is relatively low in absolute numbers, reflecting the smaller total extent of the railway system in Türkiye. However, even with limited length, exposure in critical zones can pose high operational and safety risks. Generally, heavy rail has the highest exposure levels in every class combination, followed by urban transit. In contrast, alternative rail and special transit don't really show on the bar plot, indicating their small spatial distribution.

Under the 68% exceedance scenario, the overall exposure levels are at very low to low susceptibility levels. Its exposure to moderate to high susceptibility classes is very limited, suggesting most of the railway is distributed in safer areas. Besides the 68% scenario, railway exposure under different scenarios is assessed and provided in Appendix A.8. Each scenario results in a different exposure pattern, for example, in the 2% scenario, half of the heavy rail exposed to moderate to high susceptibility, while the 50% and 10% scenario shows more diverse exposure distribution.

4.4.3. Gas Pipeline Exposure

Fig 20 shows the exposure of Türkiye's gas pipeline network to earthquake-induced landslides under 68% seismic hazard scenarios. The plots display the total length of pipelines that intersect with slope units categorized by combining landslide susceptibility and uncertainty classes. The exposure is presented in both km and percentage of the total network.

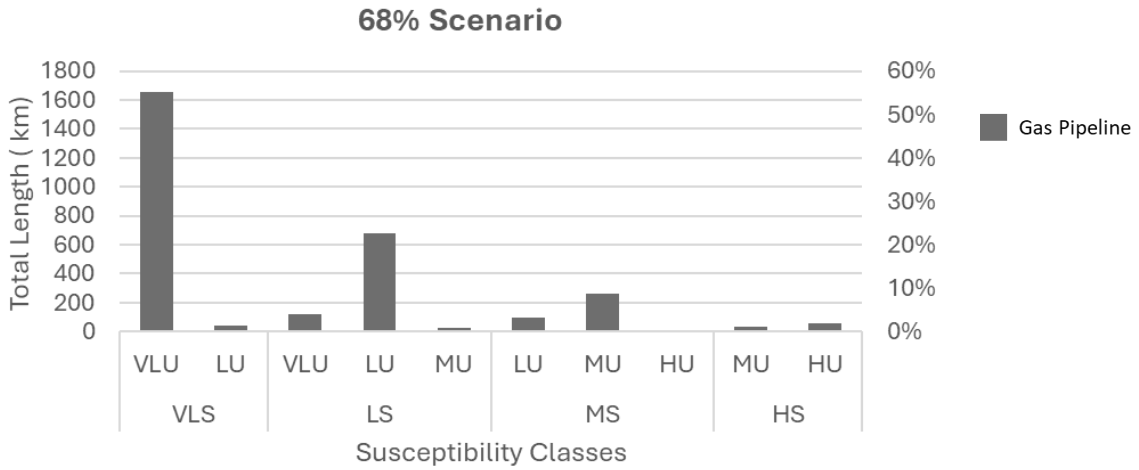

Fig 20 Gas pipeline exposure bar plots under 68% PGA exceedance probabilities.

Focusing on the 68% scenario, over half of the gas pipeline is exposed to the very low to low susceptibility classes, suggesting most of the gas pipeline is laid in safer areas. Even so, more than 10% of the pipeline is

exposed to moderate to high susceptibility classes, which may become a concern. Since gas pipelines are high-value and high-risk infrastructure, even minimal exposure to hazardous terrain could lead to serious consequences.

Exposure under 2%, 10%, and 50% was also assessed and provided in Appendix A.8. Opposite to the 68% scenario, the 2% scenario shows a significant amount of moderate to high susceptibility slope units. Although such events are rare, the extent of exposure under this scenario could pose serious concerns for infrastructure safety and disaster preparedness. On the other hand, the exposure distribution under the 10% and 50% scenarios is more varied. Even so, the 10% is dominated by moderate to high classes, while the 50% shows greater exposure in the lower susceptibility classes.

4.4.4. Electricity Network Exposure

Fig 21 presents the exposure of Türkiye's electricity transmission lines to earthquake-induced landslides under four seismic hazard scenarios. The charts show the total length of exposed electricity lines in thousands of kilometers, grouped by combinations of landslide susceptibility and uncertainty classes. This analysis helps to understand how much of the electricity network is located in areas that are potentially at risk under different landslide susceptibility scenarios.

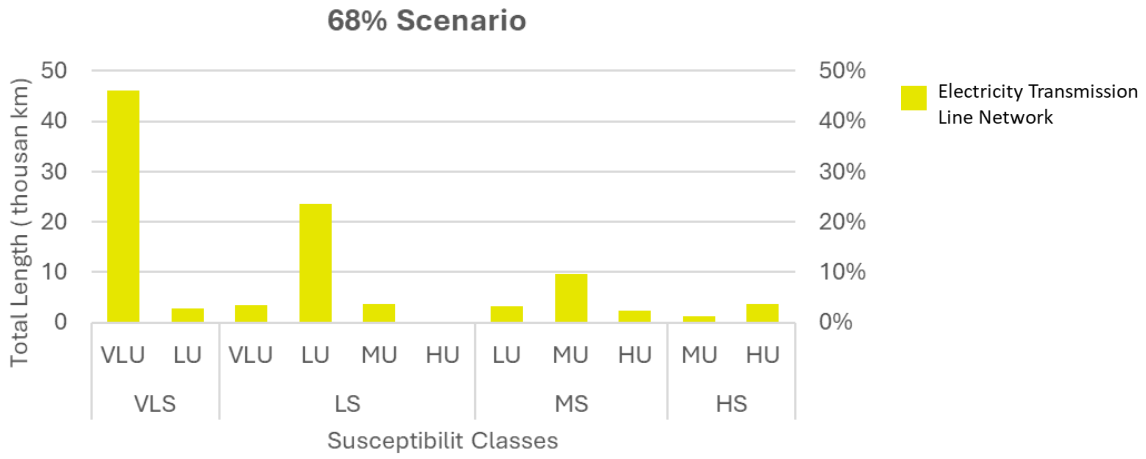

Fig 21 Electricity transmission line exposure bar plots under 68% PGA exceedance probabilities.

Focusing on the 68% scenario, half of the electricity line is located within very low susceptibility classes, and gradually decreases as susceptibility gets higher. Over 10% of electricity networks are exposed to moderate susceptibility slope units, and only less than 10% are in the higher classes. Despite its limited exposure, the number of electricity lines intersected with moderate to high susceptibility may become a concern, as this infrastructure is one of the most crucial infrastructures in the country.

Besides the 68% scenario, railway exposure under different scenarios is assessed and provided in Appendix A.10. The exposure trends are varied depending on the scenarios. For example, the electricity network exposure in the 2% scenario is gradually increased as susceptibility gets higher. Meanwhile, although most of the line was exposed to moderate to high susceptibility classes, the 10% scenario didn't show a constant increase as the 2% scenario did. On the other hand, the 50% scenario shows a similar decreasing trend to the 68% scenario. However, the distribution amount is more even, resulting in a higher amount of exposure in moderate to high susceptibility classes.

4.4.5. Agriculture exposure

Fig 22 exhibits the exposure of agricultural land to earthquake-induced landslide susceptibility across four different seismic hazard scenarios. The chart breaks down the total agricultural area exposed to susceptibility, combined with the uncertainty, allowing an understanding of both potential impact and prediction reliability. The exposures are presented in both thousand hectares and percentages, making it easier to compare and analyze.

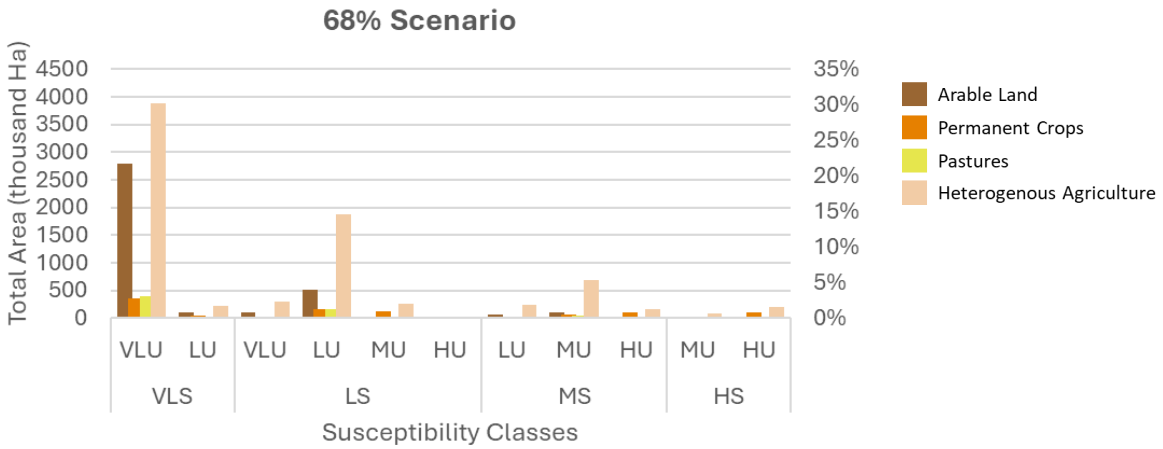

Fig 22 Agriculture area exposure bar plots under 68% PGA exceedance probabilities.

The 68% exceedance scenario is particularly useful for guiding planning decisions. In this scenario, a major portion of the agricultural area is exposed to low to very low susceptibility classes, approximately ranging from 2,500 to 4,500 ha or around 20% - 35% of the total agricultural area. In contrast, its exposure to moderate to high susceptibility classes is less than 10% of the total area.

The agricultural area exposure under other scenarios was assessed and provided in Appendix A.11. Despite the different scenarios, the general exposure pattern can be observed. Overall, the number of agricultural areas exposed to the high susceptibility classes decreases as the exceedance probability increases. As a result, most of the high susceptibility exposure is concentrated in the 2% scenario, while the 68% scenario is dominated by exposure in the very low susceptibility classes.

Generally, heterogeneous agriculture shows the highest exposure levels in every class combination, demonstrated by its highest peach-colored bar in each class. In contrast, pastures show lower exposure than other agricultural types across all scenarios. For example, in the VLS-VLU class, the heterogeneous agriculture exposure reaches over 25% of the total area, followed by arable land with more than 20%. Meanwhile, both pastures and permanent contribute less than 10%. It reflects the spatial extent of the agricultural type in the datasets, where heterogeneous agriculture and arable land occupy a larger proportion of the total land cover, while pastures and permanent crops are more limited in extent.

4.4.6. Commercial and Industrial Area Exposure

Fig 23 displays the exposure of commercial and industrial areas to earthquake-induced landslide susceptibility under the four seismic hazard scenarios. The exposure is presented in hectares and categorized into combinations of susceptibility and uncertainty classes, offering a detailed picture of potential hazard implications for economically important zones. Compared to the industrial area, the commercial area proportion within the dataset is nearly negligible, as most of the commercial areas are built in densely populated areas, which have relatively stable terrain.

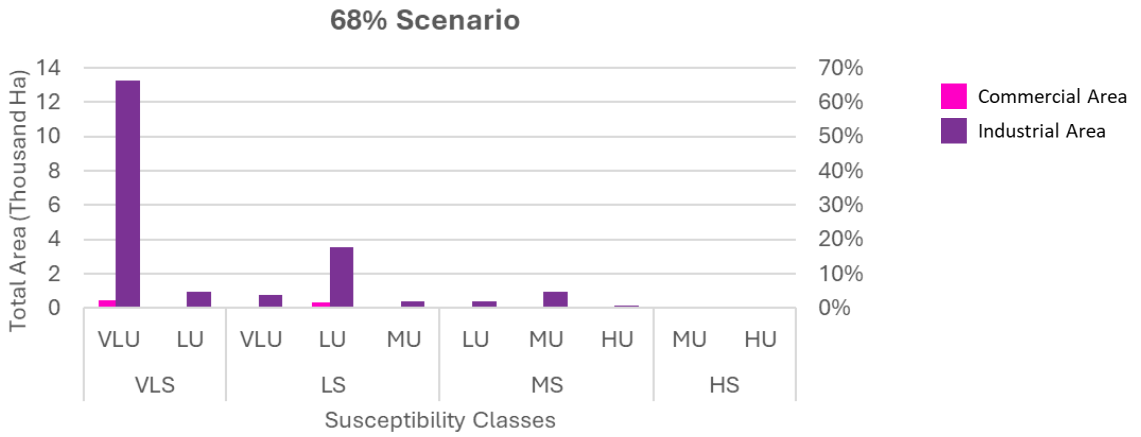

Fig 23 Commercial and industrial area exposure bar plots under 68% PGA exceedance probabilities.

Focusing on the 68% scenario, the major distribution of industrial area was exposed to the VLS-VLU class, which was almost 60% of the total area, followed by LS-LU and MS-MU. In contrast, the spatial distribution of the commercial area was very limited, less than 1000 ha in every susceptibility-uncertainty class, and only appeared in very low to low susceptibility classes.

Besides the 68% scenario, the exposure under other scenarios was assessed and provided in Appendix A.12. Each scenario shows a different exposure pattern, depending on the susceptibility classes intersected with the commercial and industrial areas. In general, the exposure under the 2% scenario is dominated by moderate to high susceptibility classes, where more than 25% of the commercial area is exposed to both MS-MU and HS-HU classes. On the other hand, most of the areas are exposed to low to moderate susceptibility classes in the 10% scenario and very low to low susceptibility classes in the 50% scenario. The findings could be relevant for land-use regulation and industrial development planning. However, areas with moderate to high susceptibility and overlapping uncertainty may need more detailed site-specific investigations before any decision-making. Additionally, as commercial and industrial areas are tied closely to economic resilience, ensuring their protection could reduce long-term disruption in the aftermath of future seismic events.

4.4.7. Building Exposure

Fig 24 presents the exposure of buildings to earthquake-induced landslide susceptibility under the four seismic hazard scenarios. The graphs show the number of exposed buildings, in thousands, across combinations of susceptibility (VLS to HS) and uncertainty (VLU to HU) classes. This provides an overview of how potential hazard levels may affect built-up areas.

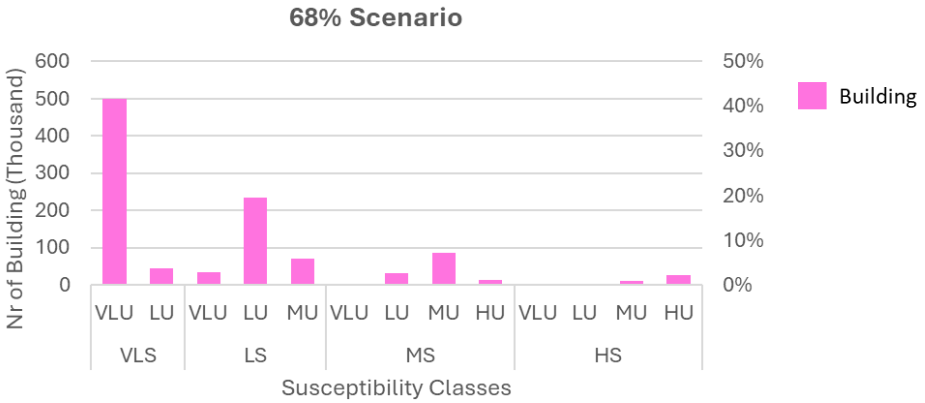

Fig 24 Bar plots of the building feature exposure bar plots under 68% PGA exceedance probabilities.

Other exposure analyses under other scenarios are assessed and provided in Appendix A.13. The exposure trends are varied across scenarios. For instance, under the 2% exceedance scenario, more than 50% of buildings are located within the HS-HU class, with very limited exposure in the lower classes. In contrast, the 10% scenario shows a more balanced distribution, though the highest exposure still falls within the MS-MU class with over 30% exposure. The 50% scenario, on the other hand, is primarily concentrated in the very low to low susceptibility classes, with less than 5% of buildings exposed to high susceptibility zones. These findings emphasize the importance of integrating landslide susceptibility into urban planning and housing policies. Identifying where buildings are located in high-susceptibility slope units can support better land-use decisions, prioritize refinement programs, and reduce disaster impact on residential communities in the long term.

4.4.8. Critical Infrastructure Exposure

Fig 25 displays the exposure of critical infrastructure to earthquake-induced landslide susceptibility across the four seismic hazard scenarios, including transportation, education, government, bank, health, and emergency services infrastructures. The graph summarizes the number of exposed critical infrastructure features intersecting with each susceptibility and uncertainty class combination.

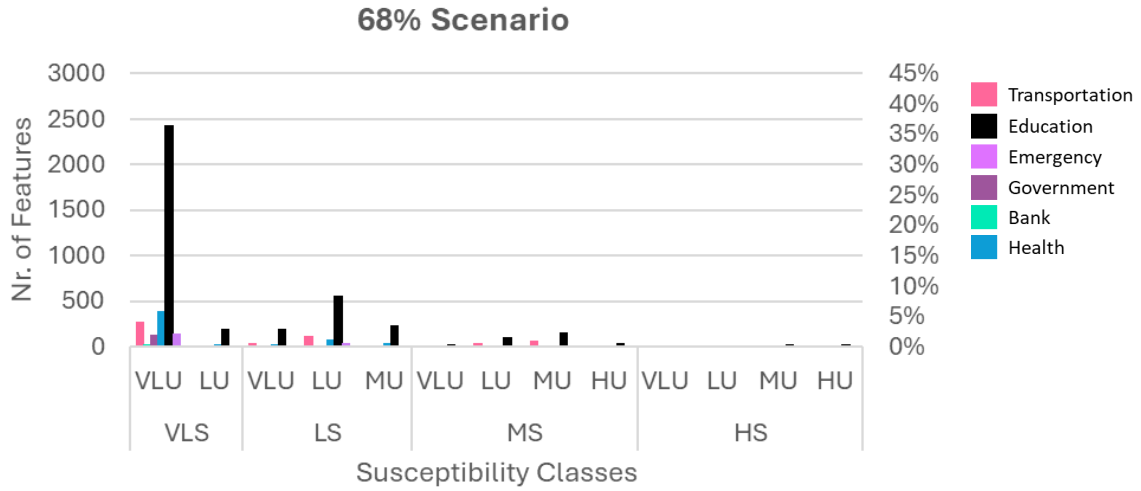

Fig 25 Bar plots of critical infrastructure exposure bar plots under 68% PGA exceedance probabilities.

Focusing on the 68% scenario, the highest number of exposed critical infrastructure features is found in the very low to low susceptibility classes. Meanwhile, its exposure within moderate to high susceptibility is limited. Overall, education infrastructure dominates the spatial distribution of critical infrastructure, as its exposure number is the highest in every susceptibility-uncertainty class. In contrast, the spatial distribution of the remaining critical infrastructure types is limited, as the exposed number is less than 500 features in each class.

The exposure of critical infrastructure under different scenarios was assessed and provided in Appendix A.14. As with other EaRs, the overall exposure patterns are varied across scenarios. In the exposure under the 2% scenario, the number of critical infrastructures exposed to moderate and high susceptibility classes is similar, while exposure within the lower classes is limited. In contrast, the 10% scenario shows the lowest exposure in the very low susceptibility class, followed by a gradual decrease in exposure from low to high susceptibility. Similarly, a decreasing trend is also observed in the 50% where most of the critical infrastructure is concentrated in the very low and low susceptibility classes, with minimal exposure to higher susceptibility zones.

5. DISCUSSION

This research aimed to model earthquake-induced landslides across Türkiye and assess their potential impact under different seismic hazard scenarios. The study utilized a data-driven approach using the landslides triggered by the 2011 Van and 2023 Kahramanmaras earthquakes. The overall workflow was structured into four main components, including exploratory data analysis, model development, scenario-based simulation, and exposure assessment.

5.1. Exploratory and Model Development Phase

In the initial exploratory phase, 17 continuous variables were assessed, derived from 12 controlling parameters commonly associated with landslide susceptibility. The exploratory analysis showed that slope steepness, LR, and PGA were the strongest factors influencing landslide occurrence. These predictors demonstrated statistically positive relationships with landslide occurrences. Proximity to active faults also showed a mild negative influence, which aligns with physical expectations and previous studies (W. Chen et al., 2014; Basharat et al., 2016; Shafique, 2020) showing a high landslide concentration near fault zones.

The final model retained four continuous variables, including slope steepness, LR, PGA, and proximity to faults, alongside the lithology and land cover. The susceptibility model was constructed using a GAM framework, allowing it to capture non-linear relationships between predictors and the probability of landslide occurrence. The decision to treat these variables as non-linear smooth functions was appropriate, as their influence on landslide probability is not necessarily linear across their entire range.

Although this data-driven approach provided useful insights, it also has some important limitations. One of the main issues is the imbalance in the landslide inventories used. The 2011 Van earthquake inventory included only 42 slope units with landslides, while the 2023 Kahramanmaras earthquake had over 1,000. Because of this large difference, the Van inventory had very little influence during both the exploratory analysis and the model development. As a result, the model may not fully capture the conditions in the Van region and could treat them as outliers.

Another limitation is related to the slope units. Using slope units as the mapping unit is practical, especially for handling different data sources and scales. However, this approach simplifies the terrain and aggregates the characteristics of the covariates into each slope unit, which may miss localized high-risk features like isolated steep patches or localized lithology. As a result, the model might underestimate susceptibility in some areas. This limitation is especially noticeable in the marginal effects of categorical variables like land cover (see Fig. 9), where most land cover types appear to have an uncertain or weak influence on landslide susceptibility. This may be because land cover features often vary over small areas, making them difficult to capture accurately when data is averaged across large slope units. As a result, important surface conditions that affect slope stability may be lost during this generalization process.

Additionally, this model does not include the dynamic and time-related processes involved in landslides, such as gradual slope weakening over time (progressive failure) (Ai et al., 2022), material fatigue from repeated stress (Preisig et al., 2015), or delayed landslide responses after an earthquake (Song et al., 2022). Capturing these types of behaviors would require more complex models, such as physically based models, which were beyond the scope of this study. As a result, the model focuses only on the conditions present at the time of the earthquake, without considering how slopes may change or deteriorate over time.

5.2. Model simulations

In this simulation, the fitted model structure was applied to new data by changing only the PGA values while keeping all other predictors constant. This allowed the model to estimate susceptibility under each seismic scenario using the same learned relationships from the original training process. More specifically, to assess potential landslide risk in future earthquakes, PGA values were extracted from Türkiye's national seismic hazard maps and used to simulate four different seismic scenarios. These values were used as dynamic inputs for model simulation while keeping all other covariates constant. This substitution enabled a scenario-based assessment of landslide susceptibility to reasonable future earthquake intensities.

The results showed that high-susceptibility areas remained concentrated along Türkiye's major fault zones and mountainous terrain. As shown in Fig. 14 and Appendix A.4, susceptibility values increase and become more spatially concentrated as PGA intensity rises. This pattern supports the underlying assumption that landslide susceptibility generally increases with higher levels of ground-shaking (Khazai & Sitar, 2004), which is also reflected by the PGA covariance regression in Fig. 9. This is also supported by the difference between the scenarios, where areas with higher difference values are primarily concentrated near active fault zones, and it tends to be more pronounced as the paired scenario reflects more intense earthquakes.

Projecting the model across Türkiye also introduced limitations. The model was trained using data from only two earthquake events, which represent specific environmental and geological conditions. Applying the model to a much broader landscape increases uncertainty, as many areas may possess very different terrain, lithology, or land cover not captured in the training data. This limitation is compounded by the incomplete spatial coverage of some predictor datasets. For example, lithology data were missing in certain parts of the country, resulting in no-data areas in the simulation outputs.

Nonetheless, this challenge is common for data-driven prediction. For example, despite its near-real-time landslide hazard assessment, the USGS global empirical model for near-real-time assessment of seismic-induced landslides also relies on sparse and incomplete landslide inventories, particularly in data-scarce regions (Jesse et al., 2018). Despite these constraints, it remains a valuable tool for identifying broad patterns of hazard. Although the use of a more comprehensive and spatially distributed landslide inventory would undoubtedly enhance the model prediction, limited data availability is a common constraint in data-driven landslide modeling. In this context, the current approach remains a reasonable and practical compromise.

5.3. Exposure

To complement the susceptibility analysis, the study estimated the exposure of several infrastructures under the four seismic scenarios. This analysis comes with several limitations. First, exposure was calculated based on slope units, which are relatively large spatial areas. While this is practical for regional-scale analysis, it does not provide the exact location where a landslide might occur or how far it might extend. As a result, the analysis only estimates how much infrastructure overlaps with susceptible slopes, not whether the landslide would actually reach and damage it. This limitation is important, as real landslide impacts often depend on the runout distance. Without runout modeling, the exposure estimates can only represent possible hazard zones rather than actual damage. More detailed impact assessments would require physically based models that simulate landslide movement, which were beyond the scope of this study.

Second, the availability and resolution of some EaR datasets also affect the results. In some areas, especially rural or rapidly changing regions, the EaR data may be outdated or incomplete, making it difficult to

accurately estimate exposure. In addition, missing or low-quality predictor data in certain regions may reduce the reliability of the susceptibility map, which influences the exposure estimates.

Despite these limitations, the exposure analysis still provides useful insights into which infrastructures are most often located in high-susceptibility zones across different seismic scenarios. It helps identify priority areas for disaster preparedness and risk reduction. The findings also offer a starting point for integrating landslide risk into broader national-scale earthquake risk planning and spatial decision-making.

6. RECOMMENDATION & CONCLUSION

6.1. Recommendation

This study provides a national-scale assessment of earthquake-induced landslide susceptibility and exposure using a data-driven modeling approach. While the results offer useful insights, the model also has some limitations that may affect its future applicability. Based on these limitations, several recommendations can be made to support future research and improve the applicability of similar models.

First, improving the spatial resolution and completeness of predictors and infrastructure datasets is essential, as it would enhance the quality of both susceptibility and exposure maps. High-resolution predictors can better capture terrain variability, allowing the model to detect local conditions that may influence landslide susceptibility. Similarly, improved infrastructure data in rural or rapidly developing areas would provide more reliable exposure estimates.

Second, although physically based runout modeling is not practical at a national scale due to its high data and computational cost, future studies could explore hybrid approaches as simplified alternatives. These approaches combine the strengths of data-driven susceptibility models with simplified runout estimation methods, such as empirical rules (Roman Quintero et al., 2024) or GIS-based tools like flow=R (Horton et al., 2011) and Topflowdf (Scheild & Rickenmann, 2011). While not as detailed as full physical simulations, these methods can still estimate potential landslide travel distances. This would make the exposure assessment more realistic by identifying not just where landslides may be triggered, but also where they are likely to reach. Incorporating even basic runout logic would be especially valuable in densely populated or infrastructure-critical areas.

Lastly, promoting open data sharing and collaborative research across institutions would help address the limited availability of earthquake-induced landslide inventories and fill gaps in national datasets. Partnerships between researchers, government institutions, and data providers can help improve inventory coverage, ensure consistent data quality, support the development of more comprehensive landslide inventories, and improve the consistency and quality of national datasets. Establishing common data standards and encouraging the sharing of methodologies would make it easier to compare and combine results from different studies and regions. In the long term, such collaboration would not only enhance the reliability of future models but also contribute to building a unified national framework. This would give decision-makers a stronger foundation for risk-informed development planning, emergency preparedness, and decision-making at both regional and national levels.

6.2. Conclusion

This study developed a national-scale assessment of earthquake-induced landslide susceptibility and exposure in Türkiye using a data-driven approach. Utilizing the GAM framework, the model was built by integrating landslide inventories from the 2011 Van and 2023 Kahramanmaras earthquakes with geospatial predictors. The model was then used to simulate future landslide susceptibility based on four PGA exceedance scenarios derived from the national seismic hazard map. An exposure assessment was conducted to estimate the potential overlap between susceptible areas and critical infrastructure. Among the predictors, slope steepness, LR, and PGA were identified as the most influential predictors. Across the different seismic scenarios, susceptibility values get higher as the PGA intensity rises, and exposure results show various exposure patterns across scenarios. These outcomes reflect the strong role of PGA in shaping earthquake-induced landslide susceptibility.

The findings of this research provide a useful starting point for understanding the spatial distribution of co-seismic landslides and their potential impact across Türkiye. By using seismic hazard maps to simulate different future earthquake scenarios, the model provides a flexible tool that can support long-term planning and disaster preparedness. The use of slope units also enables the practical integration of varied datasets, helping ensure consistency across a large and complex study area. Although simplified, the model still offers meaningful insights into where landslides are more likely to happen, and which infrastructures may be exposed. This kind of information can support decision-making in disaster risk reduction and land-use planning.

Further research should focus on improving data quality, exploring simplified runout modeling, and building modular frameworks that allow for easier updates and broader applications. Enhancing data resolution and promoting collaborative data sharing will be essential for improving model reliability and usability. By addressing these areas, future research can deliver more detailed and practical tools to support earthquake-induced landslide risk management in earthquake-prone regions.

6.3. AI Statement

During the writing process of this research, Grammarly and ChatGPT were used to prevent grammatical errors and improve fluency. All suggestions provided by these tools were carefully reviewed, edited, and used by the author, who is responsible for the final output of this research.

LIST OF REFERENCES

ADRC. (2023). *Report on Turkey-Syria Earthquakes*. Asian Disaster Reduction Center (ADRC). https://www.adrc.asia/publications/disaster_report/pdf/2023/ADRC_Report_Turkey-Syria_Earthquakes_202309.pdf

Ahmed, M., Tanyas, H., Huser, R., Dahal, A., Titti, G., Borgatti, L., Francioni, M., & Lombardo, L. (2023). Dynamic rainfall-induced landslide susceptibility: A step towards a unified forecasting system. *International Journal of Applied Earth Observation and Geoinformation*, *125*, 103593. https://doi.org/10.1016/j.jag.2023.103593

Ai, Z., Zhang, H., Wu, S., Jiang, C., Yan, Q., & Ren, Z. (2022). Study on the slope dynamic stability considering the progressive failure of the slip surface under earthquake. *Frontiers in Earth Science*, *10*. https://doi.org/10.3389/feart.2022.981503

Akkar, S., Azak, T., Çan, T., Çeken, U., Demircioğlu Tümsa, M. B., Duman, T. Y., Erdik, M., Ergintav, S., Kadirioğlu, F. T., Kalafat, D., Kale, Ö., Kartal, R. F., Kekovalı, K., Kılıç, T., Özalp, S., Altuncu Poyraz, S., Şeşetyan, K., Tekin, S., Yakut, A., … Zülfikar, Ö. (2018). Evolution of seismic hazard maps in Turkey. *Bulletin of Earthquake Engineering*, *16*(8), 3197–3228. https://doi.org/10.1007/s10518-018-0349-1

Allstadt, K. E., Jibson, R. W., Thompson, E. M., Massey, C. I., Wald, D. J., Godt, J. W., & Rengers, F. K. (2018). Improving near-real-time coseismic landslide models: Lessons learned from the 2016 Kaikōura, New Zealand, earthquake. *Bulletin of the Seismological Society of America*, *108*(3B), 1649–1664. Scopus. https://doi.org/10.1785/0120170297

Alvioli, M., Marchesini, I., Reichenbach, P., Rossi, M., Ardizzone, F., Fiorucci, F., & Guzzetti, F. (2016). Automatic delineation of geomorphological slope units with <tt>r.slopeunits v1.0</tt> and their optimization for landslide susceptibility modeling. *Geoscientific Model Development*, *9*(11), 3975–3991. https://doi.org/10.5194/gmd-9-3975-2016

Alvioli, M., Poggi, V., Peresan, A., Scaini, C., Tamaro, A., & Guzzetti, F. (2024). A scenario-based approach for immediate post-earthquake rockfall impact assessment. *Landslides*, *21*(1), 1–16. https://doi.org/10.1007/s10346-023-02127-2

Ayalew, L., & Yamagishi, H. (2005). The application of GIS-based logistic regression for landslide susceptibility mapping in the Kakuda-Yahiko Mountains, Central Japan. *Geomorphology*, *65*(1), 15–31. https://doi.org/10.1016/j.geomorph.2004.06.010

Basharat, M., Shah, H. R., & Hameed, N. (2016). Landslide susceptibility mapping using GIS and weighted overlay method: A case study from NW Himalayas, Pakistan. *Arabian Journal of Geosciences*, *9*(4), 292. https://doi.org/10.1007/s12517-016-2308-y

Bird, J. F., & Bommer, J. J. (2004). Earthquake losses due to ground failure. *Engineering Geology*, *75*(2), 147–179. https://doi.org/10.1016/j.enggeo.2004.05.006

Bray, J. D., & Travasarou, T. (2007). Simplified Procedure for Estimating Earthquake-Induced Deviatoric Slope Displacements. *Journal of Geotechnical and Geoenvironmental Engineering*, *133*(4), 381–392. https://doi.org/10.1061/(ASCE)1090-0241(2007)133:4(381)

Brenning, A. (2012). Spatial cross-validation and bootstrap for the assessment of prediction rules in remote sensing: The R package sperrorest. *2012 IEEE International Geoscience and Remote Sensing Symposium*, 5372–5375. https://doi.org/10.1109/IGARSS.2012.6352393

Caccavale, M., Matano, F., & Sacchi, M. (2017). An integrated approach to earthquake-induced landslide hazard zoning based on probabilistic seismic scenario for Phlegrean Islands (Ischia, Procida and Vivara), Italy. *Geomorphology*, *295*, 235–259. https://doi.org/10.1016/j.geomorph.2017.07.010

Çaglayan, M. A., & Yurtseven, A. (1998). 1/100.000 scaled Turkey Geology maps. *Burgaz A-3 and A-4, Edirne B-2, B-3, Kırklareli B-4, B-5, B-6 and C-6 Sheets*, *20*, 21.

Chen, W., Li, W., Hou, E., Zhao, Z., Deng, N., Bai, H., & Wang, D. (2014). Landslide susceptibility mapping based on GIS and information value model for the Chencang District of Baoji, China. *Arabian Journal of Geosciences*, *7*(11), 4499–4511. https://doi.org/10.1007/s12517-014-1369-z

Chen, X., Ran, H., Zhou, Q., & Zhou, B. (2017). Local Terrain Relief: An Important Factor Influencing the Generation of Large Earthquake-Triggered Landslides. In M. Mikoš, N. Casagli, Y. Yin, & K. Sassa (Eds.), *Advancing Culture of Living with Landslides* (pp. 15–21). Springer International Publishing. https://doi.org/10.1007/978-3-319-53485-5_3

Chen, Z., & Wang, G. (2023). Comparison of empirically-based and physically-based analyses of coseismic landslides: A case study of the 2016 Kumamoto earthquake. *Soil Dynamics and Earthquake Engineering*, *172*, 108009. https://doi.org/10.1016/j.soildyn.2023.108009

Cheng, Q., Tian, Y., Lu, X., Huang, Y., & Ye, L. (2021). Near-real-time prompt assessment for regional earthquake-induced landslides using recorded ground motions. *Computers & Geosciences*, *149*, 104709. https://doi.org/10.1016/j.cageo.2021.104709

Chigira, M., & Yagi, H. (2006). Geological and geomorphological characteristics of landslides triggered by the 2004 Mid Niigta prefecture earthquake in Japan. *Engineering Geology*, *82*(4), 202–221. https://doi.org/10.1016/j.enggeo.2005.10.006

Conforti, M., Pascale, S., Robustelli, G., & Sdao, F. (2014). Evaluation of prediction capability of the artificial neural networks for mapping landslide susceptibility in the Turbolo River catchment (northern Calabria, Italy). *CATENA*, *113*, 236–250. https://doi.org/10.1016/j.catena.2013.08.006

Deniz Ekinci. (2012). The Mountains of Turkey. *ResearchGate*. https://www.researchgate.net/publication/383148961_THE_MOUNTAINS_OF_TURKEY

Francesco Caleca, Luigi Lombardo, Stefan Steger, Hakan Tanyas, Federico Raspini, Ashok Dahal, Constantinos Nefros, Mihai Ciprian Mărgărint, Vincent Drouin, Mateja Jemec-Auflič, Alessandro Novellino, Marj Tonini, Marco Loche, Nicola Casagli, & Veronica Tofani. (2025). Pan-European Landslide Risk Assessment: From Theory to Practice. *Reviews of Geophysics*, *63*(1). https://doi.org/10.1029/2023RG000825

Gerstenberger, M. C., Marzocchi, W., Allen, T., Pagani, M., Adams, J., Danciu, L., Field, E. H., Fujiwara, H., Luco, N., Ma, K.-F., Meletti, C., & Petersen, M. D. (2020). Probabilistic Seismic Hazard Analysis at Regional and National Scales: State of the Art and Future Challenges. *Reviews of Geophysics*, *58*(2), e2019RG000653. https://doi.org/10.1029/2019RG000653

Ghasemian, B., Shahabi, H., Shirzadi, A., Al-Ansari, N., Jaafari, A., Kress, V. R., Geertsema, M., Renoud, S., & Ahmad, A. (2022). A Robust Deep-Learning Model for Landslide Susceptibility Mapping: A Case Study of Kurdistan Province, Iran. *Sensors*, *22*(4), Article 4. https://doi.org/10.3390/s22041573

Gorum, T. (2016). 23 Ekim 2011 Van Depreminin Tetiklediği Heyelanlar. *TÜRK COĞRAFYA DERGİSİ*. https://doi.org/10.17211/tcd.69854

Gorum, T., Fan, X., van Westen, C. J., Huang, R. Q., Xu, Q., Tang, C., & Wang, G. (2011). Distribution pattern of earthquake-induced landslides triggered by the 12 May 2008 Wenchuan earthquake. *Geomorphology*, *133*(3–4), 152–167. Scopus. https://doi.org/10.1016/j.geomorph.2010.12.030

Görüm, T., Tanyas, H., Karabacak, F., Yılmaz, A., Girgin, S., Allstadt, K. E., Süzen, M. L., & Burgi, P. (2023). Preliminary documentation of coseismic ground failure triggered by the February 6, 2023 Türkiye earthquake sequence. *Engineering Geology*, *327*, 107315. https://doi.org/10.1016/j.enggeo.2023.107315

He, Q., Wang, M., & Liu, K. (2021). Rapidly assessing earthquake-induced landslide susceptibility on a global scale using random forest. *Geomorphology*, *391*, 107889. https://doi.org/10.1016/j.geomorph.2021.107889

Herold, M., Latham ,J. S., Di Gregorio ,A., & and Schmullius, C. C. (2006). Evolving standards in land cover characterization. *Journal of Land Use Science*, *1*(2–4), 157–168. https://doi.org/10.1080/17474230601079316

Horton, P., Jaboyedoff, M., Zimmermann, M., Mazotti, B., & Longchamp, C. (2011). Flow-r, a model for debris flow susceptibility mapping at a regional scale – some case studies. *Italian Journal of Engineering Geology and Environment*, 875–884. https://doi.org/10.4408/IJEGE.2011-03.B-095

Jesse, M. A. N., Hamburger, M. W., Allstadt, K., Wald, D. J., Robeson, S. M., Tanyas, H., Hearne, M., & Thompson, E. M. (2018). A Global Empirical Model for Near-Real-Time Assessment of Seismically Induced Landslides. *Journalof Geophysical Research: Earth Surface*, *123*, 1835–1859. https://doi.org/10.1029/2017JF004494

Johnston, E. C., Davenport, F. V., Wang, L., Caers, J. K., Muthukrishnan, S., Burke, M., & Diffenbaugh, N. S. (2021). Quantifying the Effect of Precipitation on Landslide Hazard in Urbanized and Non-Urbanized Areas. *Geophysical Research Letters*, *48*(16), e2021GL094038. https://doi.org/10.1029/2021GL094038

Karakas, G., Nefesliogl u, H. A., Kocaman, S., Buyukdemircioglu, M., Yurur, T., & Gokceoglu, C. (2021). Derivation of earthquake-induced landslide distribution using aerial photogrammetry: The January 24, 2020, Elazig (Turkey) earthquake. *Landslides*, *18*(6), 2193–2209. https://doi.org/10.1007/s10346-021-01660-2

Karakas, G., Unal, E. O., Cetinkaya, S., Ozcan, N. T., Karakas, V. E., Can, R., Gokceoglu, C., & Kocaman, S. (2024). Analysis of landslide susceptibility prediction accuracy with an event-based inventory: The 6 February 2023 Turkiye earthquakes. *Soil Dynamics and Earthquake Engineering*, *178*, 108491. https://doi.org/10.1016/j.soildyn.2024.108491

Keefer, D. K. (2000). Statistical analysis of an earthquake-induced landslide distribution—The 1989 Loma Prieta, California event. *Engineering Geology*, *58*(3), 231–249. https://doi.org/10.1016/S0013-7952(00)00037-5

Khazai, B., & Sitar, N. (2004). Evaluation of factors controlling earthquake-induced landslides caused by Chi-Chi earthquake and comparison with the Northridge and Loma Prieta events. *Engineering Geology*, *71*(1), 79–95. https://doi.org/10.1016/S0013-7952(03)00127-3

Kritikos, T., Robinson, T. R., & Davies, T. R. H. (2015). Regional coseismic landslide hazard assessment without historical landslide inventories: A new approach. *Journal of Geophysical Research: Earth Surface*, *120*(4), 711–729. https://doi.org/10.1002/2014JF003224

Kuhn, M. (2008). Building Predictive Models in R Using the caret Package. *Journal of Statistical Software*, *28*, 1–26. https://doi.org/10.18637/jss.v028.i05

Kutner, M., Nachtsheim, C., & Neter, J. (2004). Applied Linear Regression Model. In *Technometrics* (Vol. 26). https://doi.org/10.2307/1269508

Lee, E. M., Fookes, P. G., & Hart, A. B. (2016). Landslide issues associated with oil and gas pipelines in mountainous terrain. *Quarterly Journal of Engineering Geology and Hydrogeology*, *49*(2), 125–131. https://doi.org/10.1144/qjegh2016-020

Lee, S., & Min, K. (2001). Statistical analysis of landslide susceptibility at Yongin, Korea. *Environmental Geology*, *40*(9), 1095–1113. https://doi.org/10.1007/s002540100310

Lima, P., Steger, S., Glade, T., & Murillo-García, F. G. (2022). Literature review and bibliometric analysis on data-driven assessment of landslide susceptibility. *Journal of Mountain Science*, *19*(6), 1670–1698. https://doi.org/10.1007/s11629-021-7254-9

Luo, J., & and Xiong, C. (2013). Youden Index and Associated Cut-Points for Three Ordinal Diagnostic Groups. *Communications in Statistics - Simulation and Computation*, *42*(6), 1213–1234. https://doi.org/10.1080/03610918.2012.661906

Mai, P. M., Aspiotis, T., Aquib, T. A., Cano, E. V., Castro-Cruz, D., Espindola-Carmona, A., Li, B., Li, X., Liu, J., Matrau, R., Nobile, A., Palgunadi, K. H., Ribot, M., Parisi, L., Suhendi, C., Tang, Y., Yalcin, B., Avşar, U., Klinger, Y., & Jónsson, S. (2023). The Destructive Earthquake Doublet of 6 February 2023 in South-Central Türkiye and Northwestern Syria: Initial Observations and Analyses. *The Seismic Record*, *3*(2), 105–115. https://doi.org/10.1785/0320230007

Marchesini, I., Althuwaynee, O., Santangelo, M., Alvioli, M., Cardinali, M., Mergili, M., Reichenbach, P., Peruccacci, S., Balducci, V., Agostino, I., Esposito, R., & Rossi, M. (2024). National-scale assessment of railways exposure to rapid flow-like landslides. *Engineering Geology*, *332*, 107474. https://doi.org/10.1016/j.enggeo.2024.107474

Melgar, D., Taymaz, T., Ganas, A., Crowell, B., Öcalan, T., Kahraman, M., Tsironi, V., Yolsal-Çevikbilen, S., Valkaniotis, S., Irmak, T. S., Eken, T., Erman, C., Özkan, B., Dogan, A. H., & Altuntaş, C. (2023). Sub- and super-shear ruptures during the 2023 Mw 7.8 and Mw 7.6 earthquake doublet in SE Türkiye. *Seismica*, *2*(3), Article 3. https://doi.org/10.26443/seismica.v2i3.387

Moreno, M., Steger, S., Tanyas, H., & Lombardo, L. (2023). Modeling the area of co-seismic landslides via data-driven models: The Kaikōura example. *Engineering Geology*, *320*, 107121. https://doi.org/10.1016/j.enggeo.2023.107121

Mousavi, S. M., Omidvar, B., Ghazban, F., & Feyzi, R. (2011). Quantitative risk analysis for earthquake-induced landslides—Emamzadeh Ali, Iran. *Engineering Geology*, *122*(3), 191–203. https://doi.org/10.1016/j.enggeo.2011.05.010

Nakanishi, R., & Takemura, S. (2023). *Development of a simple offshore ground motion prediction equation based on S-net data and residual analysis to reveal site effects*. https://doi.org/10.21203/rs.3.rs-3663651/v1

Nowicki, M. A., Wald, D. J., Hamburger, M. W., Hearne, M., & Thompson, E. M. (2014). Development of a globally applicable model for near real-time prediction of seismically induced landslides. *Engineering Geology*, *173*, 54–65. https://doi.org/10.1016/j.enggeo.2014.02.002

Ojomo, O., Rathje, E. M., Wang, P., Lavrendiatis, G., Zimmaro, P., Asimaki, D., & Stewart, J. P. (2024). Regional earthquake-induced landslide assessments for use in seismic risk analyses of distributed gas infrastructure systems. *Engineering Geology*, *340*, 107664. https://doi.org/10.1016/j.enggeo.2024.107664

Omine, H., Hayashi, T., Yashiro, H., & Fukushima, S. (2008, October 12). *Seismic risk analysis method using both PGA and PGV*. The 14th World Conference on Earthquake Engineering, Beijing. https://www.iitk.ac.in/nicee/wcee/article/14_07-0161.pdf

Preisig, G., Gischig, V., Eberhardt, E., & Hungr, O. (2015, May). Hydromechanical versus seismic fatigue in progressive failure of deep-seated landslides. *13th International Congress of Rock Mechanics*. ISRM, Montréal, Canada. https://doi.org/10.13140/RG.2.1.2565.0081

Qin, Y., Zhang, D., Zheng, W., Yang, J., Chen, G., Duan, L., Liang, S., & Peng, H. (2023). Interaction of earthquake-triggered landslides and local relief: Evidence from the 2008 Wenchuan earthquake. *Landslides*, *20*(4), 757–770. https://doi.org/10.1007/s10346-022-01996-3

Robin, X., Turck, N., Hainard, A., Tiberti, N., Lisacek, F., Sanchez, J.-C., & Müller, M. (2011). pROC: An open-source package for R and S+ to analyze and compare ROC curves. *BMC Bioinformatics*, *12*(1), 77. https://doi.org/10.1186/1471-2105-12-77

Robinson, T. R., Rosser, N. J., Davies, T. R. H., Wilson, T. M., & Orchiston, C. (2018). Near-Real-Time Modeling of Landslide Impacts to Inform Rapid Response: An Example from the 2016 Kaikōura, New Zealand, Earthquake. *Bulletin of the Seismological Society of America*, *108*(3B), 1665–1682. https://doi.org/10.1785/0120170234

Roman Quintero, D. C., Ortiz Contreras, J. D., Tapias Camacho, M. A., & Oviedo-Ocaña, E. R. (2024). Empirical Estimation of Landslide Runout Distance Using Geometrical Approximations in the Colombian North–East Andean Region. *Sustainability*, *16*(2), Article 2. https://doi.org/10.3390/su16020793

Rue, H., Martino, S., & Chopin, N. (2009). Approximate Bayesian Inference for Latent Gaussian models by using Integrated Nested Laplace Approximations. *Journal of the Royal Statistical Society Series B: Statistical Methodology*, *71*(2), 319–392. https://doi.org/10.1111/j.1467-9868.2008.00700.x

Sappington, J. M., Longshore, K. M., & Thompson, D. B. (2007). Quantifying Landscape Ruggedness for Animal Habitat Analysis: A Case Study Using Bighorn Sheep in the Mojave Desert. *The Journal of Wildlife Management*, *71*(5), 1419–1426. https://doi.org/10.2193/2005-723

Scheild, C., & Rickenmann, D. (2011). Topflowdf—A simple gis based model to simulate debris-flow runout on the fan. *Italian Journal of Engineering Geology and Environment*, 253–262. https://doi.org/10.4408/IJEGE.2011-03.B-030

Schmidt, K. M., & Montgomery, D. R. (1995). Limits to relief. *Science*, *270*(5236), 617–620.

Shafique, M. (2020). Spatial and temporal evolution of co-seismic landslides after the 2005 Kashmir earthquake. *Geomorphology*, *362*, 107228. https://doi.org/10.1016/j.geomorph.2020.107228

Shao, X., Ma, S., Xu, C., Cheng, J., & Xu, X. (2023). Seismically-induced landslide probabilistic hazard mapping of Aba Prefecture and Chengdu Plain region, Sichuan Province, China for future seismic scenarios. *Geoscience Letters*, *10*(1), 55. https://doi.org/10.1186/s40562-023-00307-5

Shao, X., & Xu, C. (2022). Earthquake-induced landslides susceptibility assessment: A review of the state-of-the-art. *Natural Hazards Research*, *2*(3), 172–182. https://doi.org/10.1016/j.nhres.2022.03.002

Song, C., Yu, C., Li, Z., Utili, S., Frattini, P., Crosta, G., & Peng, J. (2022). Triggering and recovery of earthquake accelerated landslides in Central Italy revealed by satellite radar observations. *Nature Communications*, *13*(1), 7278. https://doi.org/10.1038/s41467-022-35035-5

Sreejaya, K. P., Raghukanth, S. T. G., Gupta, I. D., Murty, C. V. R., & Srinagesh, D. (2022). Seismic hazard map of India and neighbouring regions. *Soil Dynamics and Earthquake Engineering*, *163*, 107505. https://doi.org/10.1016/j.soildyn.2022.107505

Tanyas, H., Rossi, M., Alvioli, M., van Westen, C. J., & Marchesini, I. (2019). A global slope unit-based method for the near real-time prediction of earthquake-induced landslides. *Geomorphology*, *327*, 126–146. Scopus. https://doi.org/10.1016/j.geomorph.2018.10.022

Tanyaş, H., van Westen, C. J., Allstadt, K. E., Anna Nowicki Jessee, M., Görüm, T., Jibson, R. W., Godt, J. W., Sato, H. P., Schmitt, R. G., Marc, O., & Hovius, N. (2017). Presentation and Analysis of a Worldwide Database of Earthquake-Induced Landslide Inventories. *Journal of Geophysical Research: Earth Surface*, *122*(10), 1991–2015. https://doi.org/10.1002/2017JF004236

Tatar, O., Sözbilir, H., Koçbulut, F., Bozkurt, E., Aksoy, E., Eski, S., Özmen, B., Alan, H., & Metin, Y. (2020). Surface deformations of 24 January 2020 Sivrice (Elazığ)–Doğanyol (Malatya) earthquake (Mw = 6.8) along the Pütürge segment of the East Anatolian Fault Zone and its comparison with Turkey's 100-year-surface ruptures. *Mediterranean Geoscience Reviews*, *2*(3), 385–410. https://doi.org/10.1007/s42990-020-00037-2

Tetteh, F. K., Abbey, S. J., Booth, C. A., & Nukah, P. D. (2025). Current Understanding and Uncertainties Associated with Climate Change and the Impact on Slope Stability: A Systematic literature review. *Natural Hazards Research*. https://doi.org/10.1016/j.nhres.2025.01.011

Türkeş, M. (1996). Spatial and Temporal Analysis of Annual Rainfall Variations in Turkey. *International Journal of Climatology*, *16*(9), 1057–1076. https://doi.org/10.1002/(SICI)1097-0088(199609)16:9<1057::AID-JOC75>3.0.CO;2-D

U. S. Geological Survey. (2023a). *M 7.5—Elbistan earthquake, Kahramanmaras earthquake sequence*. https://earthquake.usgs.gov/earthquakes/eventpage/us6000jlqa/executive

U. S. Geological Survey. (2023b). *M 7.8—Pazarcik earthquake, Kahramanmaras earthquake sequence*. https://earthquake.usgs.gov/earthquakes/eventpage/us6000jllz/executive

USGS. (2019). *Earthquake Hazards 101—The Basics*. https://www.usgs.gov/programs/earthquake-hazards/science/earthquake-hazards-101-basics

Utkucu, M. (2013). 23 October 2011 Van, Eastern Anatolia, earthquake (MW7.1) and seismotectonics of Lake Van area. *Journal of Seismology*, *17*(2), 783–805. https://doi.org/10.1007/s10950-012-9354-z

Uzielli, M., Nadim, F., Lacasse, S., & Kaynia, A. M. (2008). A conceptual framework for quantitative estimation of physical vulnerability to landslides. *Engineering Geology*, *102*(3), 251–256. https://doi.org/10.1016/j.enggeo.2008.03.011

Valavi, R., Elith, J., Lahoz-Monfort, J. J., & Guillera-Arroita, G. (2019). blockCV: An r package for generating spatially or environmentally separated folds for k-fold cross-validation of species distribution models. *Methods in Ecology and Evolution*, *10*(2), 225–232. https://doi.org/10.1111/2041-210X.13107

van Westen, C. J., van Asch, T. W. J., & Soeters, R. (2006). Landslide hazard and risk zonation—Why is it still so difficult? *Bulletin of Engineering Geology and the Environment*, *65*(2), 167–184. https://doi.org/10.1007/s10064-005-0023-0

Vandana, Dadhich, H. K., Mittal, H., & Mishra, O. P. (2024). Ground motion prediction equation for NW Himalaya and its surrounding region. *Quaternary Science Advances*, *13*, 100136. https://doi.org/10.1016/j.qsa.2023.100136

Varnes, D. J. (1978). Slope Movement Types and Processes. *Transportation Research Board Special Report*, 11–33.

Wang, Y., Ling, Y., Chan, T. O., & Awange, J. (2024). High-resolution earthquake-induced landslide hazard assessment in Southwest China through frequency ratio analysis and LightGBM. *International Journal of Applied Earth Observation and Geoinformation*, *131*, 103947. https://doi.org/10.1016/j.jag.2024.103947

Wasowski, J., Keefer, D. K., & Lee, C.-T. (2011). Toward the next generation of research on earthquake-induced landslides: Current issues and future challenges. *Engineering Geology*, *122*(1), 1–8. https://doi.org/10.1016/j.enggeo.2011.06.001

Wikipedia. (2025). 2023 Turkey–Syria earthquakes. In *Wikipedia*. https://en.wikipedia.org/w/index.php?title=2023_Turkey%E2%80%93Syria_earthquakes&oldid=1293232923#cite_note-AFPFeb224-111

Wood, S. N., & Augustin, N. H. (2002). GAMs with integrated model selection using penalized regression splines and applications to environmental modelling. *Ecological Modelling*, *157*(2), 157–177. https://doi.org/10.1016/S0304-3800(02)00193-X

Woodard, J. B., Mirus, B. B., Wood, N. J., Allstadt, K. E., Leshchinsky, B. A., & Crawford, M. M. (2024). Slope Unit Maker (SUMak): An efficient and parameter-free algorithm for delineating slope units to improve landslide modeling. *Natural Hazards and Earth System Sciences*, *24*(1), 1–12. https://doi.org/10.5194/nhess-24-1-2024

Xi, C., Lombardo, L., Hu, X., & Tanyas, H. (2024). Co-seismic hillslope weakening. *Engineering Geology*, *338*, 107607. https://doi.org/10.1016/j.enggeo.2024.107607

Xi, C., Tanyas, H., Lombardo, L., He, K., Hu, X., & Jibson, R. W. (2024). Estimating weakening on hillslopes caused by strong earthquakes. *Communications Earth & Environment*, *5*(1), 1–14. https://doi.org/10.1038/s43247-024-01256-3

Yılmaz, A., Görüm, T., Tanyas, H. (in preparation). Landslides and hillslope displacements caused by the February 6, 2023 Türkiye earthquake sequence

Youden, W. J. (1950). Index for rating diagnostic tests. *Cancer*, *3*(1), 32–35. https://doi.org/10.1002/1097-0142(1950)3:1<32::AID-CNCR2820030106>3.0.CO;2-3

Zhang, B., Yu, Y., Li, X., & Wang, Y. (2022). Ground motion prediction equation for the average horizontal component of PGA, PGV, and 5% damped acceleration response spectra at periods ranging from 0.033 to 8.0s in southwest China. *Soil Dynamics and Earthquake Engineering*, *159*, 107297. https://doi.org/10.1016/j.soildyn.2022.107297

Zhang, K., Wang, S., Bao, H., & Zhao, X. (2019). Characteristics and influencing factors of rainfall-induced landslide and debris flow hazards in Shaanxi Province, China. *Natural Hazards and Earth System Sciences*, *19*(1), 93–105. https://doi.org/10.5194/nhess-19-93-2019

APPENDIX

A.1 Seismic Hazard Map

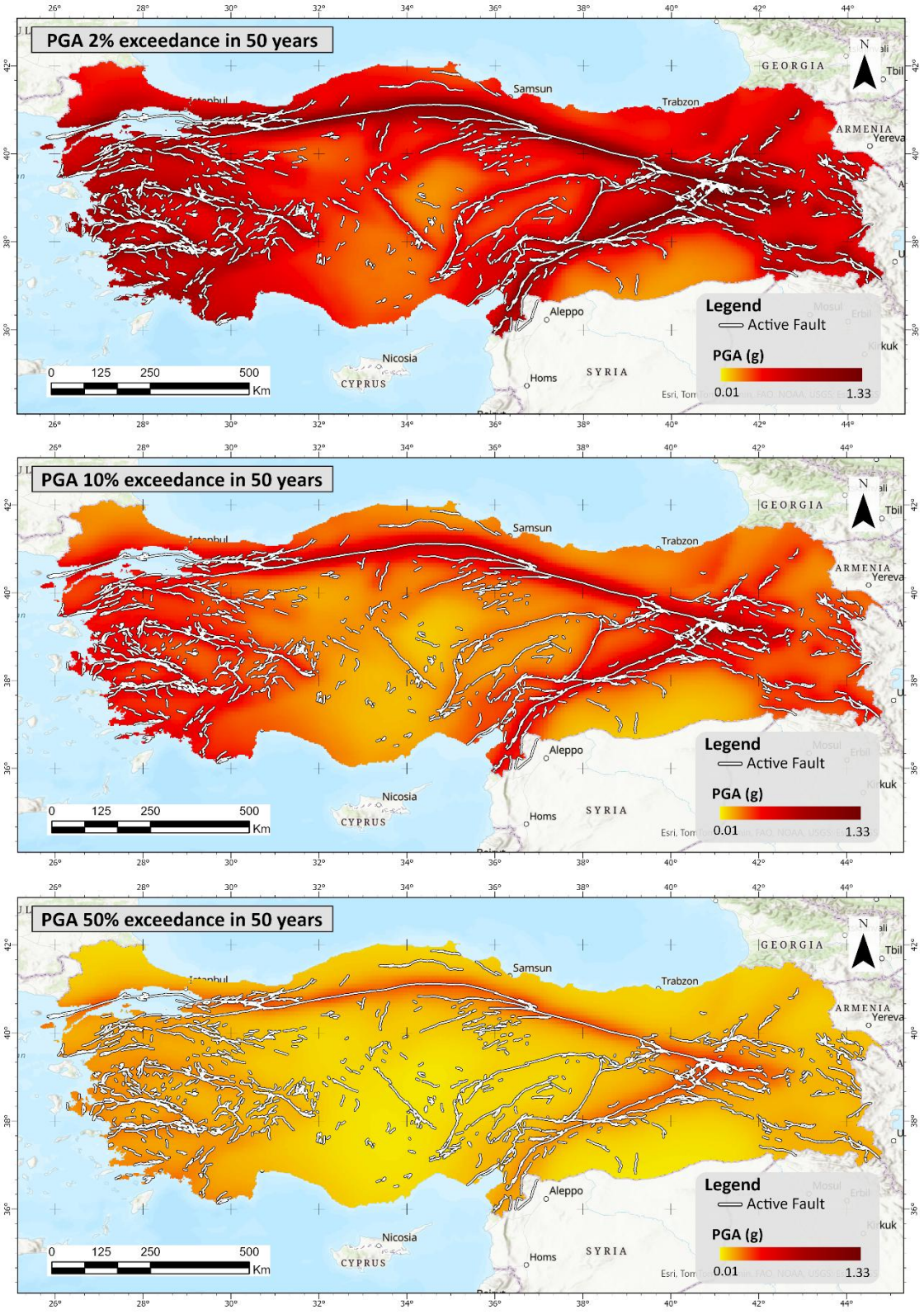

Figure 1 PGA 2%, 10%, and 50% exceedance probability in 50 years, derived from Türkiye's seismic hazard map

A.2 Random Effect Value

Tab 1 The random effect value of the model represents the relationship between the predictors and landslide occurrence

	RANDOM EFFECTS IN THE GAM				
	Mean	**Sd**	**0.025sq**	**0.5sq**	**0.975sq**
Slope average					
1	-1.92	0.45	-2.81	-1.92	-1.04
2	-1.85	0.23	-2.30	-1.85	-1.39
3	-1.28	0.14	-1.55	-1.28	-1.01
4	-0.86	0.12	-1.09	-0.86	-0.64
5	-0.25	0.11	-0.46	-0.25	-0.04
6	0.26	0.11	0.05	0.26	0.47
7	0.77	0.11	0.55	0.77	0.99
8	1.32	0.13	1.05	1.32	1.58
9	1.86	0.18	1.50	1.86	2.22
10	1.95	0.28	1.40	1.95	2.50
Local Relief					
1	-1.35	0.20	-1.74	-1.35	-0.95
2	-0.90	0.12	-1.14	-0.90	-0.66
3	-0.51	0.10	-0.72	-0.51	-0.31
4	-0.09	0.10	-0.29	-0.09	0.10
5	-0.01	0.11	-0.22	-0.01	0.20
6	0.30	0.12	0.08	0.30	0.53
7	0.32	0.14	0.04	0.32	0.60
8	0.62	0.17	0.28	0.62	0.95
9	0.81	0.23	0.36	0.81	1.27
10	0.82	0.33	0.17	0.82	1.46
PGA (g)					
1	-2.53	0.17	-2.86	-2.53	-2.19
2	-1.14	0.10	-1.34	-1.14	-0.94
3	-0.46	0.10	-0.66	-0.46	-0.26
4	-0.20	0.11	-0.41	-0.20	0.01
5	0.40	0.10	0.20	0.40	0.60
6	0.38	0.12	0.15	0.38	0.61
7	0.66	0.16	0.35	0.66	0.97
8	0.87	0.24	0.39	0.87	1.35
9	0.98	0.29	0.41	0.98	1.55
10	1.04	0.30	0.45	1.04	1.63
Proximity to Fault					
1	0.14	0.21	-0.27	0.14	0.55
2	-0.22	0.21	-0.63	-0.22	0.19
3	-0.11	0.21	-0.53	-0.11	0.30
4	-0.32	0.22	-0.76	-0.32	0.12
5	0.03	0.21	-0.38	0.03	0.44
6	0.22	0.21	-0.18	0.22	0.63
7	0.10	0.22	-0.34	0.10	0.54
8	0.06	0.27	-0.48	0.06	0.59
9	0.05	0.35	-0.62	0.05	0.73
10	0.05	0.42	-0.78	0.05	0.89
Lithology					
Plutonic	-0.83	0.16	-1.15	-0.83	-0.51
Volcanic	0.73	0.10	0.54	0.73	0.91
Metamorphic	-0.21	0.08	-0.37	-0.21	-0.05
Ophiolitic	0.15	0.09	-0.02	0.15	0.32
Sedimentary	0.17	0.06	0.04	0.17	0.29

	RANDOM EFFECTS IN THE GAM				
	Mean	**Sd**	**0.025sq**	**0.5sq**	**0.975sq**
Land use					
Tree cover	-0.17	0.11	-0.39	-0.17	0.05
Shrubland	-0.09	0.19	-0.46	-0.09	0.28
Grassland	0.19	0.11	-0.02	0.19	0.40
Cropland	-0.08	0.18	-0.42	-0.08	0.27
Built-up	-0.04	0.20	-0.43	-0.04	0.35
Bare land	0.19	0.15	-0.10	0.19	0.48
Herbaceous wetland	0.00	0.20	-0.40	0.00	0.40

A.3 Spatially illustrated RCV and SCV fold

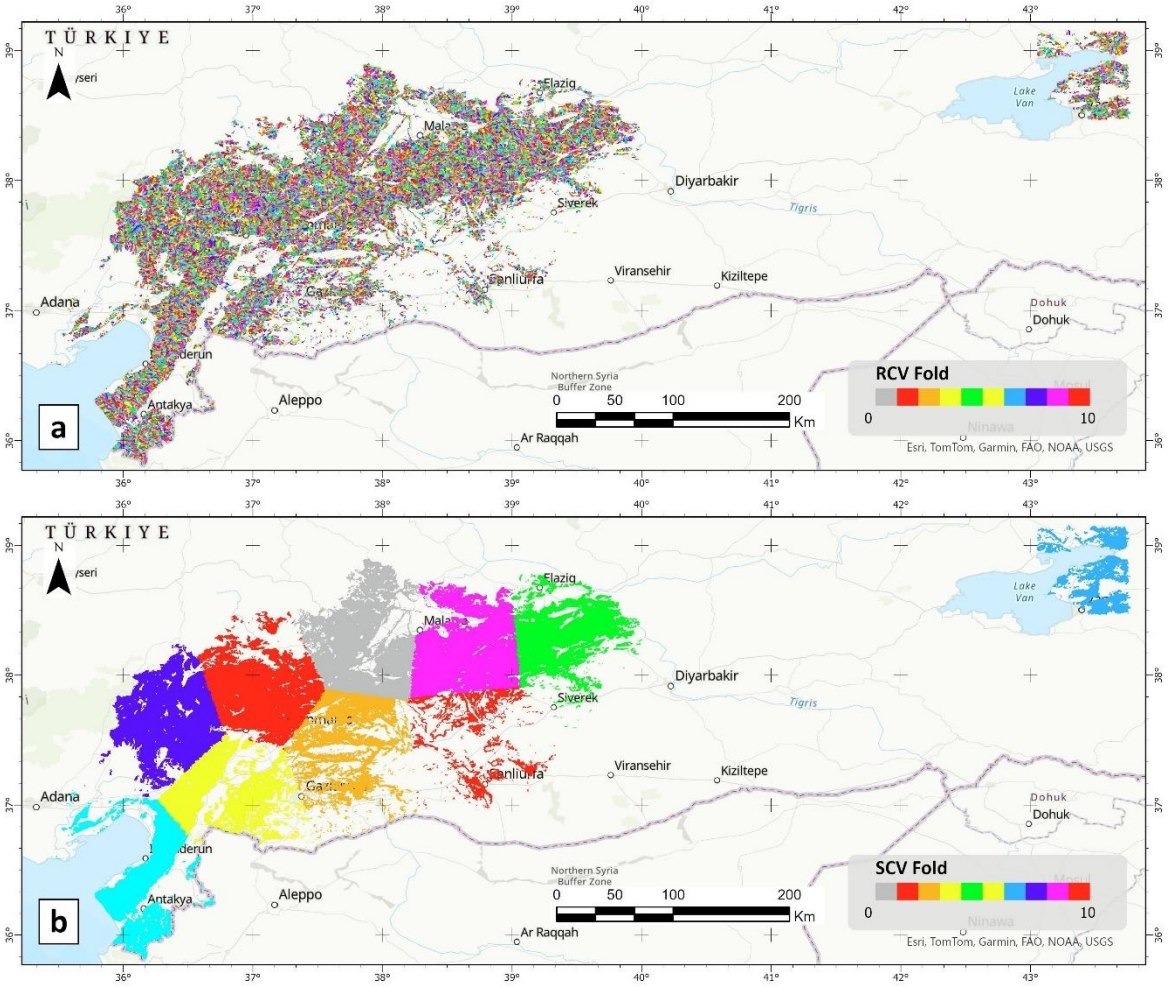

Figure 2 The spatial distribution of the data split for both RCV (a) and SCV(b) methods. Each fold is presented in different colors as shown in the legend.

A.4 Model Simulation – Susceptibility

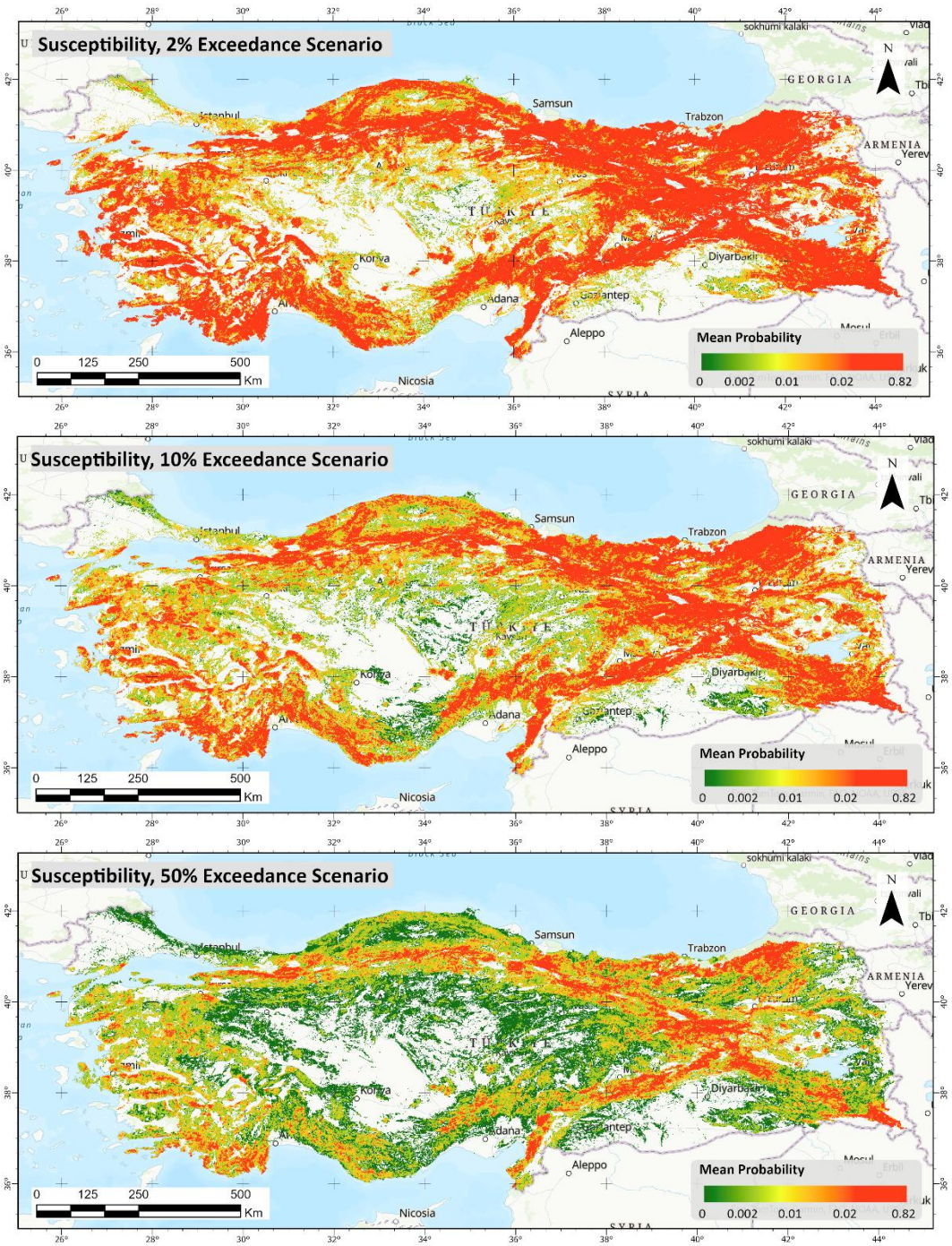

Figure 3 Earthquake-induced landslide susceptibility maps for 2%, 10%, and 50% PGA exceedance probability in 50 years

A.5 Model Simulation – Uncertainty

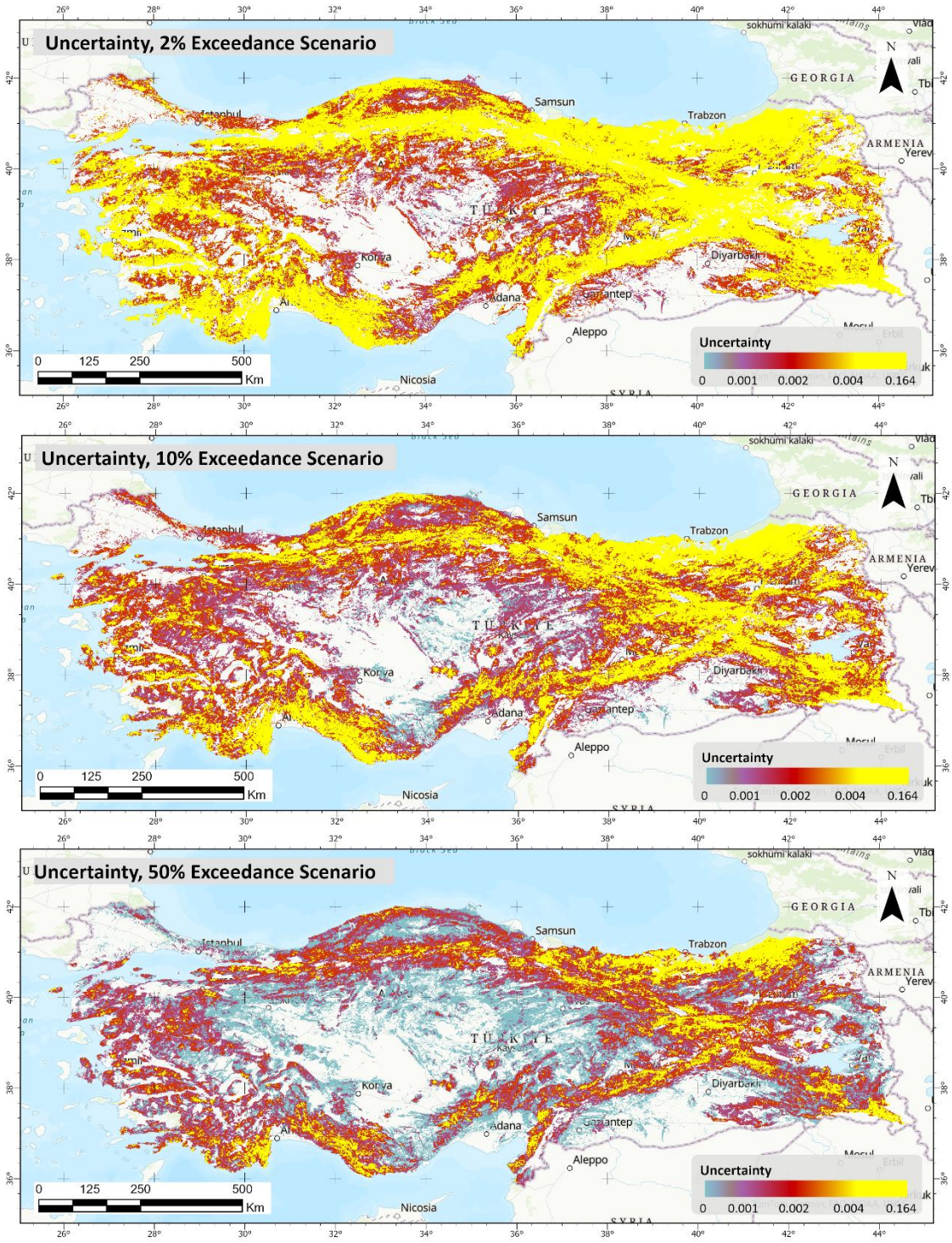

Figure 4 Earthquake-induced landslide uncertainty maps for 2%, 10%, and 50% PGA exceedance probability in 50 years

A.6 Model Simulation – Difference

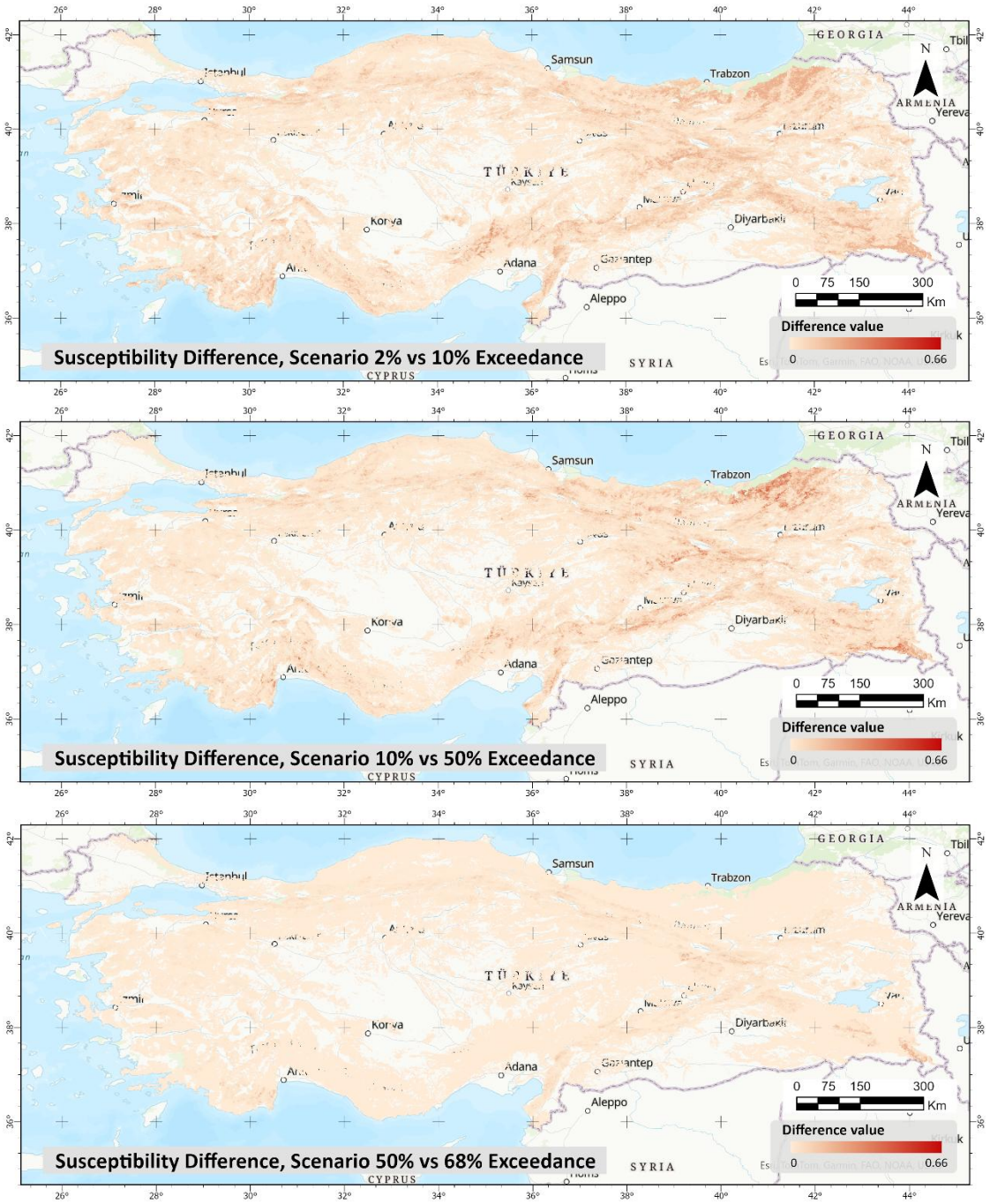

Figure 5 The susceptibility differences between 2% and 10% scenarios, 10% and 50% scenarios, and 50% and 68% scenarios.

A.7 Road Exposure

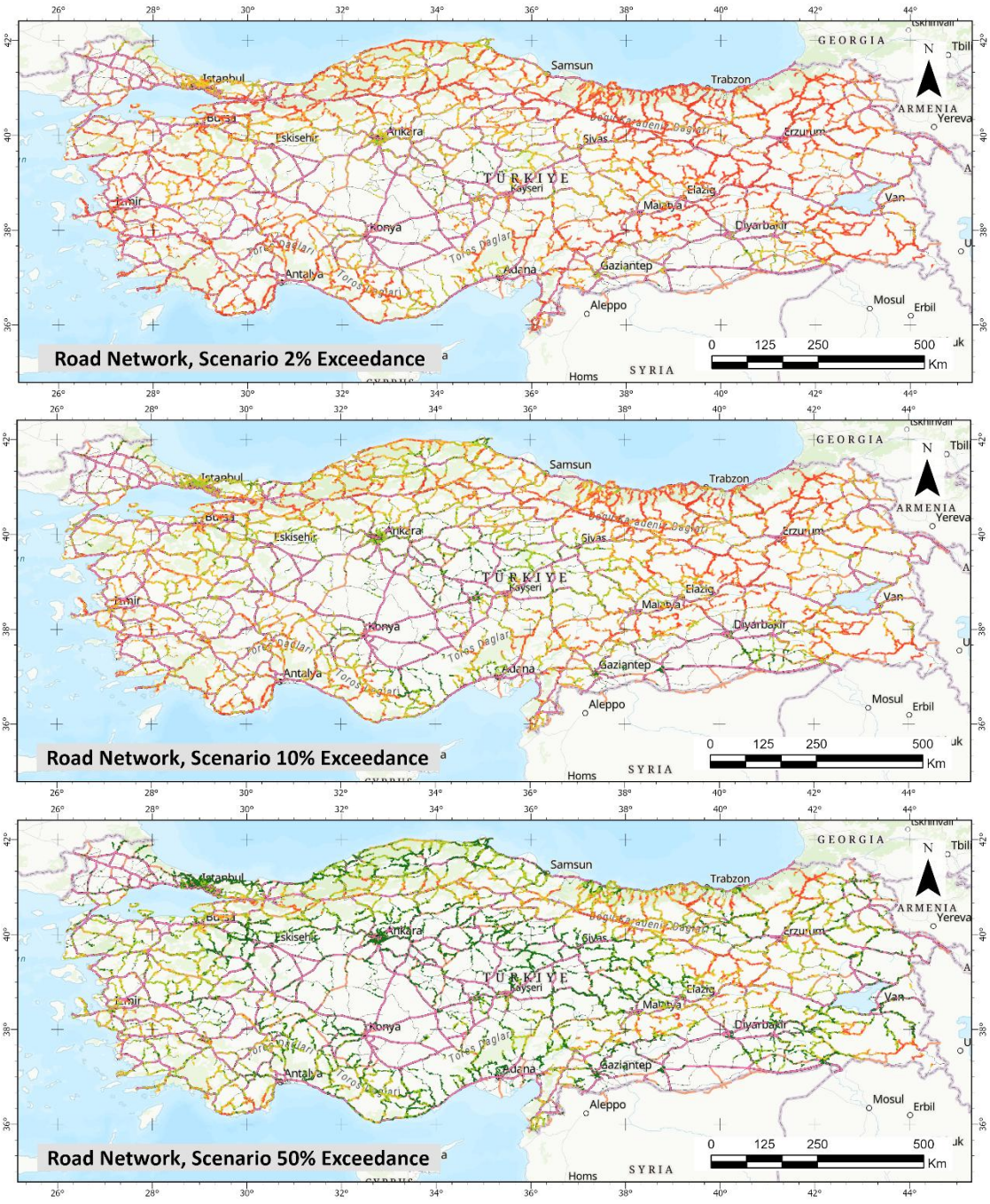

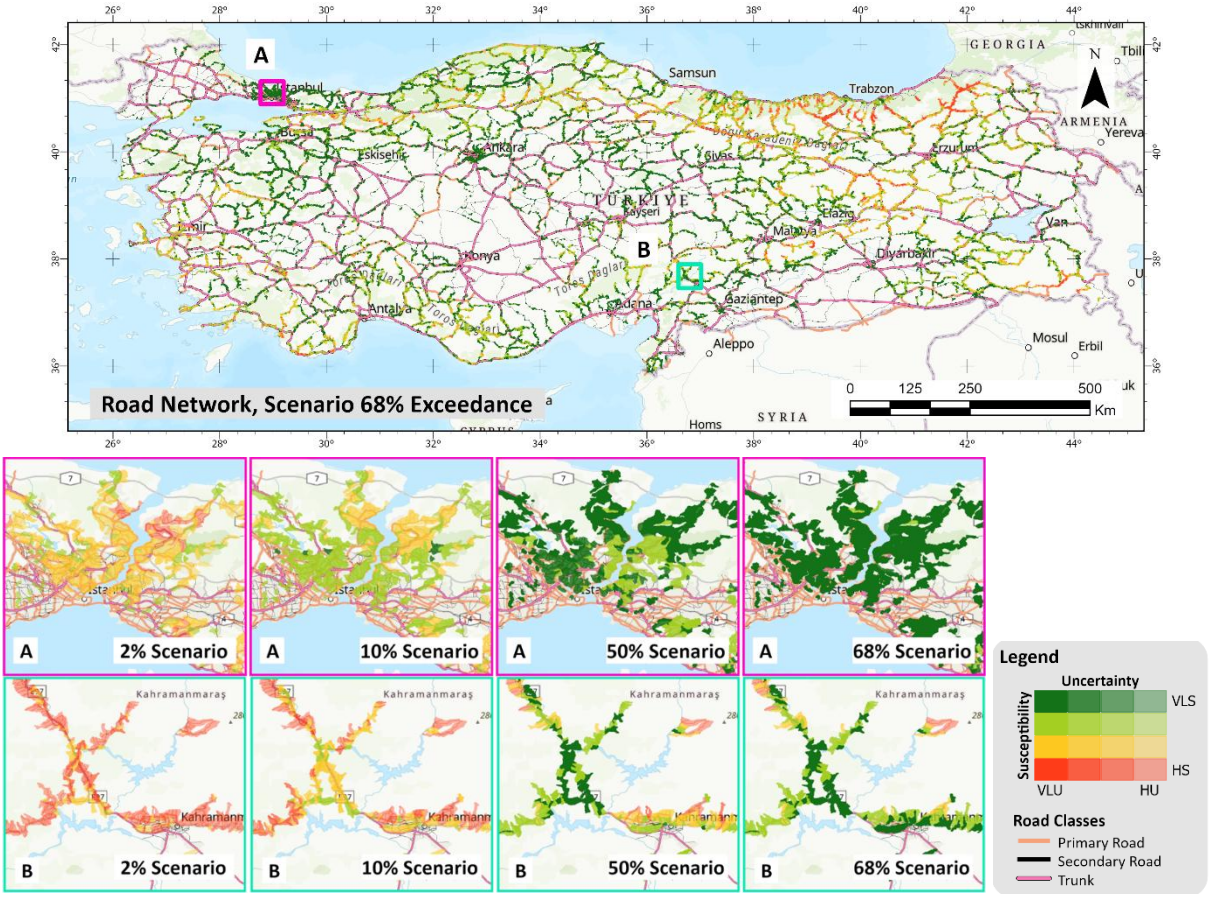

Figure 6 Road network exposure map under 2%, 10%, 50%, and 68% PGA exceedance probabilities

Tab 2 The length of the road network exposed to susceptibility under 2%, 10%, 50%, and 68% PGA exceedance probabilities

68% Scenario	VLS		LS				MS			HS		Grand Total
	VLU	LU	VLU	LU	MU	HU	LU	MU	HU	MU	HU	
Primary	3229	337	167	1642	491		146	723	277	42	542	7596
Secondary	8907	626	600	4653	1035		542	1879	689	178	817	19926
Trunk	7359	591	569	3043	600	3	571	1311	290	202	405	14941
Grand Total	19494	1554	1336	9339	2126	3	1259	3912	1256	422	1763	42463

50% Scenario	VLS		LS				MS			HS		Grand Total
	VLU	LU	VLU	LU	MU	HU	LU	MU	HU	MU	HU	
Primary	2063	522	245	1879	477		329	980	285	108	709	7596
Secondary	5986	822	909	5027	1005		993	2664	700	434	1387	19926
Trunk	4972	639	865	3613	653	3	839	1864	314	392	787	14941
Grand Total	13021	1983	2019	10519	2135	3	2161	5508	1298	934	2883	42463

10% Scenario	VLS		LS			MS			HS		Grand Total
	VLU	LU	VLU	LU	MU	LU	MU	HU	MU	HU	
Primary	179	152	82	1392	428	291	1982	492	354	2246	7596
Secondary	664	387	255	4007	850	1088	5244	894	1131	5405	19926
Trunk	521	289	155	3288	653	909	4257	678	670	3522	14941
Grand Total	1363	828	492	8687	1931	2288	11483	2064	2155	11172	42463

2% Scenario	VLS			LS				MS			HS		Grand Total
	VLU	LU	MU	VLU	LU	MU	HU	LU	MU	HU	MU	HU	
Primary	7	18			428	348		69	1765	648	216	4097	7596
Secondary	33	54	0	6	1295	758		286	5101	1351	752	10291	19926
Trunk	24	18		1	1030	688	1	240	4154	1163	455	7168	14941
Grand Total	64	90	0	6	2753	1794	1	595	11020	3162	1423	21556	42463

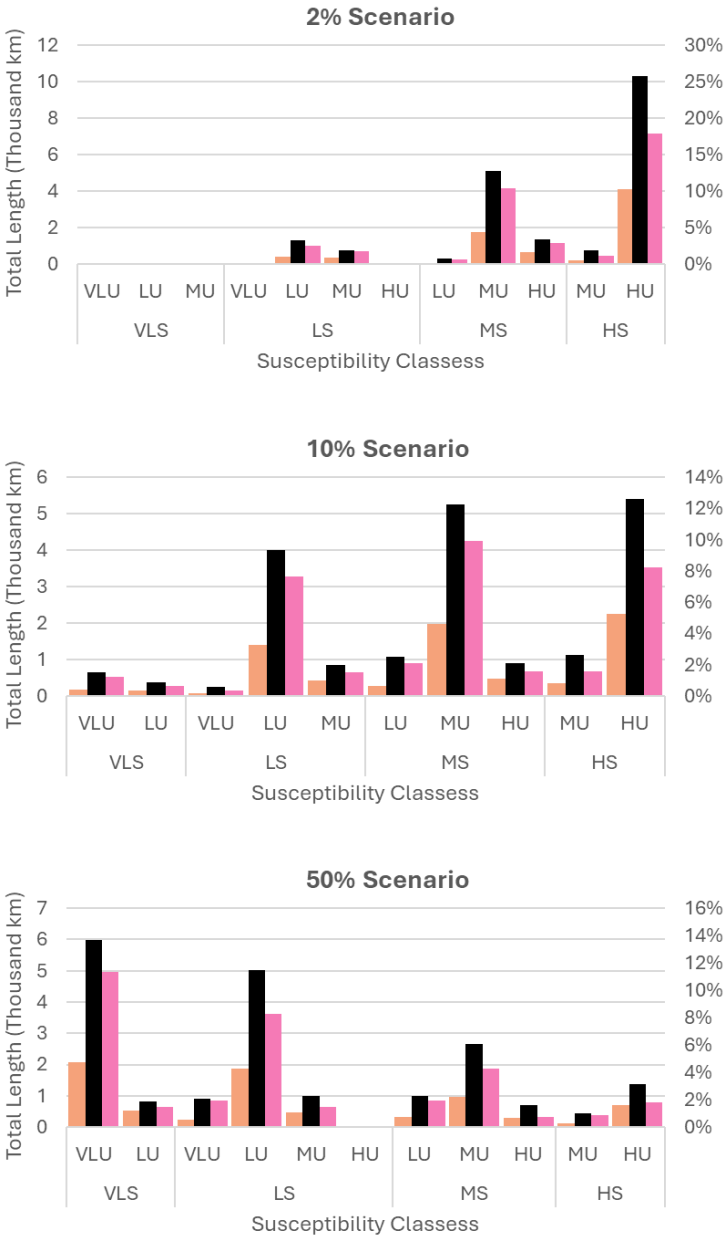

Figure 7 Road network exposure bar plots under 2%, 10%, and 50% PGA exceedance probabilities

A.8 Railway Exposure

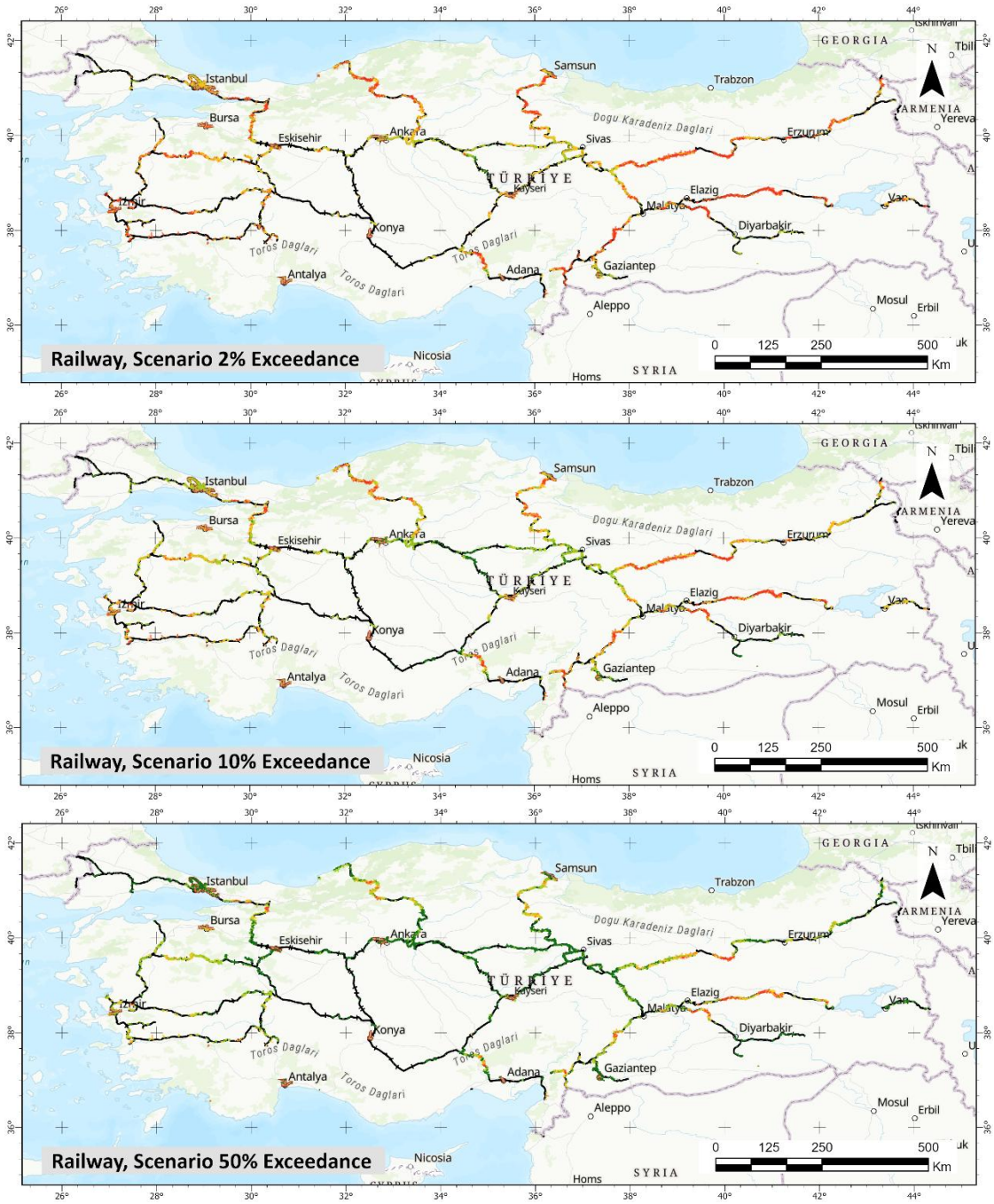

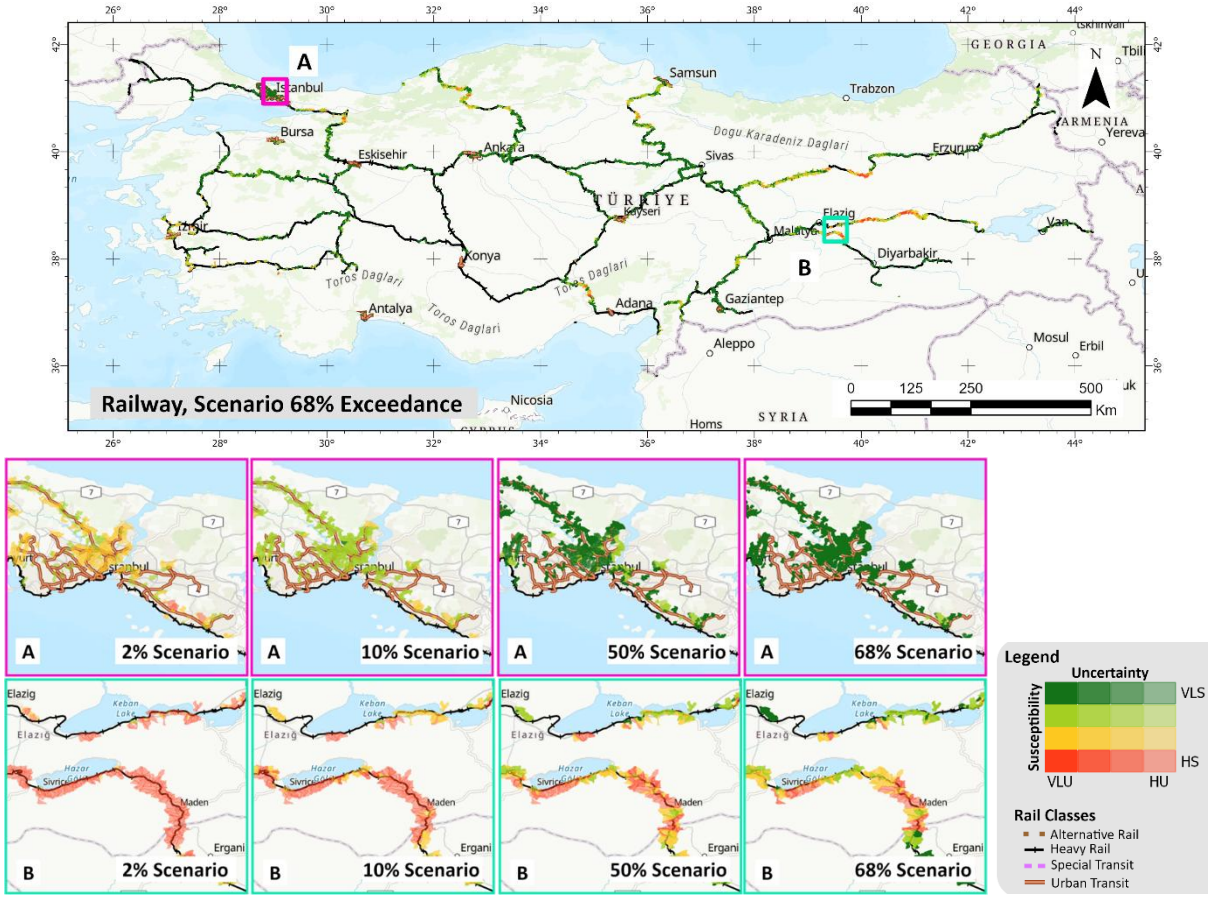

Figure 8 Railway exposure map under 2%, 10%, 50%, and 68% PGA exceedance probabilities

Tab 3 The length of the railway exposed to susceptibility under 2%, 10%, 50%, and 68% PGA exceedance probabilities

68% scenario	VLS		LS			MS			HS		Grand Total
	VLU	LU	VLU	LU	MU	LU	MU	HU	MU	HU	
Special Transit	3.31			0.10							3.42
Urban Transit	178.19	7.93		24.60	6.07	0.76	1.34				218.89
Alternative Rail	2.82									0.64	3.46
Heavy Rail	2049.61	73.44	123.75	672.28	17.92	68.20	274.52	6.63	36.36	109.44	3432.15
Grand Total	2233.94	81.37	123.75	696.99	23.99	68.96	275.86	6.63	36.36	110.08	3657.93

50% Scenario	VLS		LS			MS			HS		Grand Total
	VLU	LU	VLU	LU	MU	LU	MU	HU	MU	HU	
Special Transit	0.06	1.62		1.74							3.42
Urban Transit	90.79	74.60	0.41	36.21	6.08	1.24	9.55				218.89
Alternative Rail	1.29	1.53								0.64	3.46
Heavy Rail	1462.30	106.58	136.04	850.36	21.41	175.40	376.55	7.61	94.73	201.19	3432.15
Grand Total	1554.44	184.32	136.45	888.31	27.49	176.63	386.10	7.61	94.73	201.83	3657.93

10% Scenario	VLS		LS			MS			HS		Grand Total
	VLU	LU	VLU	LU	MU	LU	MU	HU	MU	HU	
funicular				0.94	1.47		1.01				3.42
Urban Transit	2.31	5.31		119.69	40.81		34.33	8.07	2.05	6.32	218.89
Alternative Rail				2.82						0.64	3.46
Heavy Rail	178.03	87.05	102.43	949.38	78.30	218.64	929.65	39.97	177.36	671.35	3432.15
Grand Total	180.34	92.35	102.43	1072.83	120.58	218.64	964.98	48.04	179.42	678.31	3657.93

2% Scenario	VLS		LS			MS			HS		Grand Total
	VLU	LU	VLU	LU	MU	LU	MU	HU	MU	HU	
funicular							3.01	0.31		0.10	3.42
Urban Transit				24.52	41.70		100.58	27.35	0.56	24.17	218.89
Alternative Rail					1.29		1.53			0.64	3.46
Heavy Rail	6.00	22.04	2.90	323.44	185.59	101.74	1070.59	182.41	128.78	1408.67	3432.15
Grand Total	6.00	22.04	2.90	347.96	228.58	101.74	1175.71	210.07	129.34	1433.59	3657.93

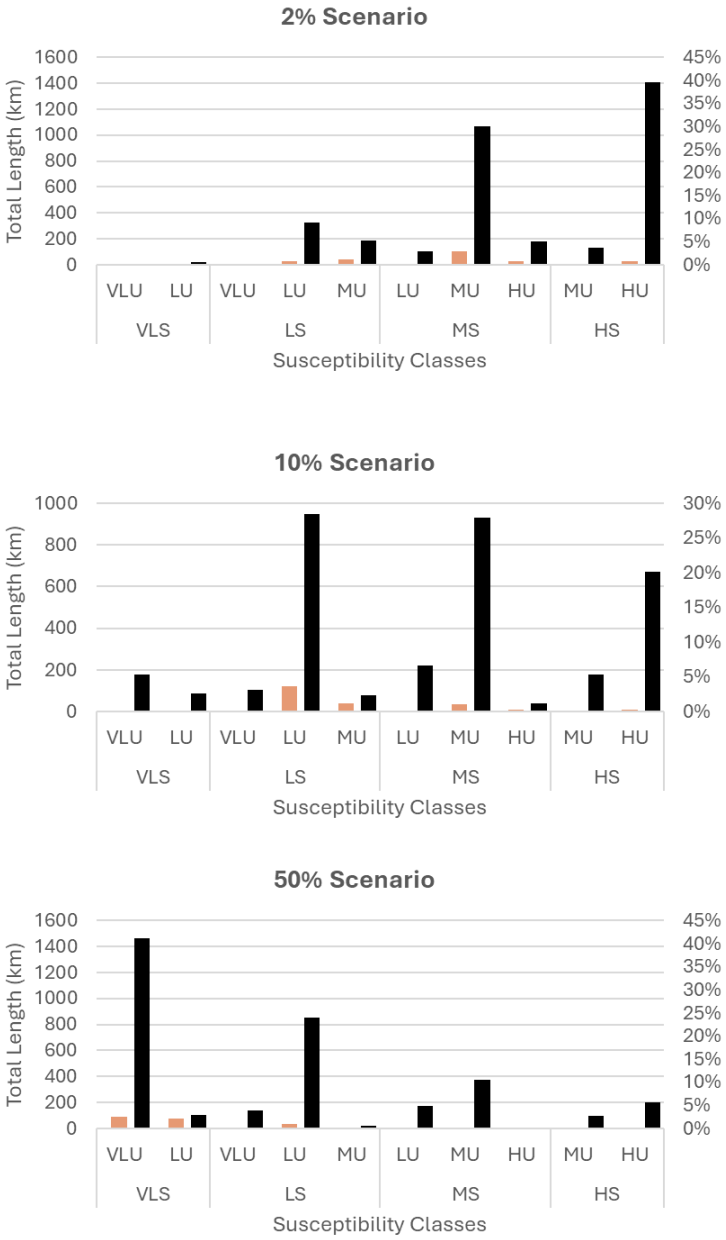

Figure 9 Railway exposure bar plots under 2%, 10%, and 50% PGA exceedance probabilities

A.9 Gas Pipeline Exposure

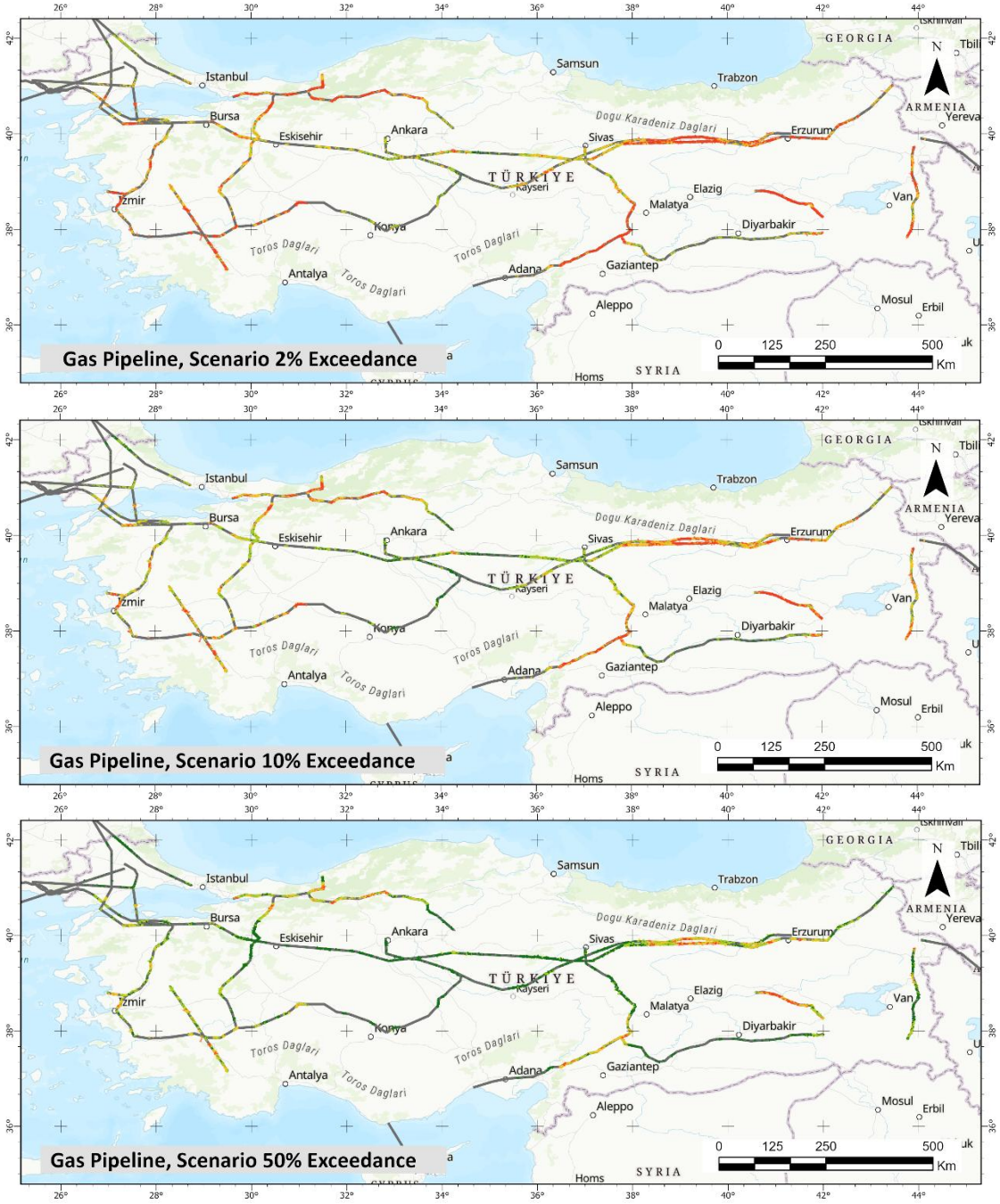

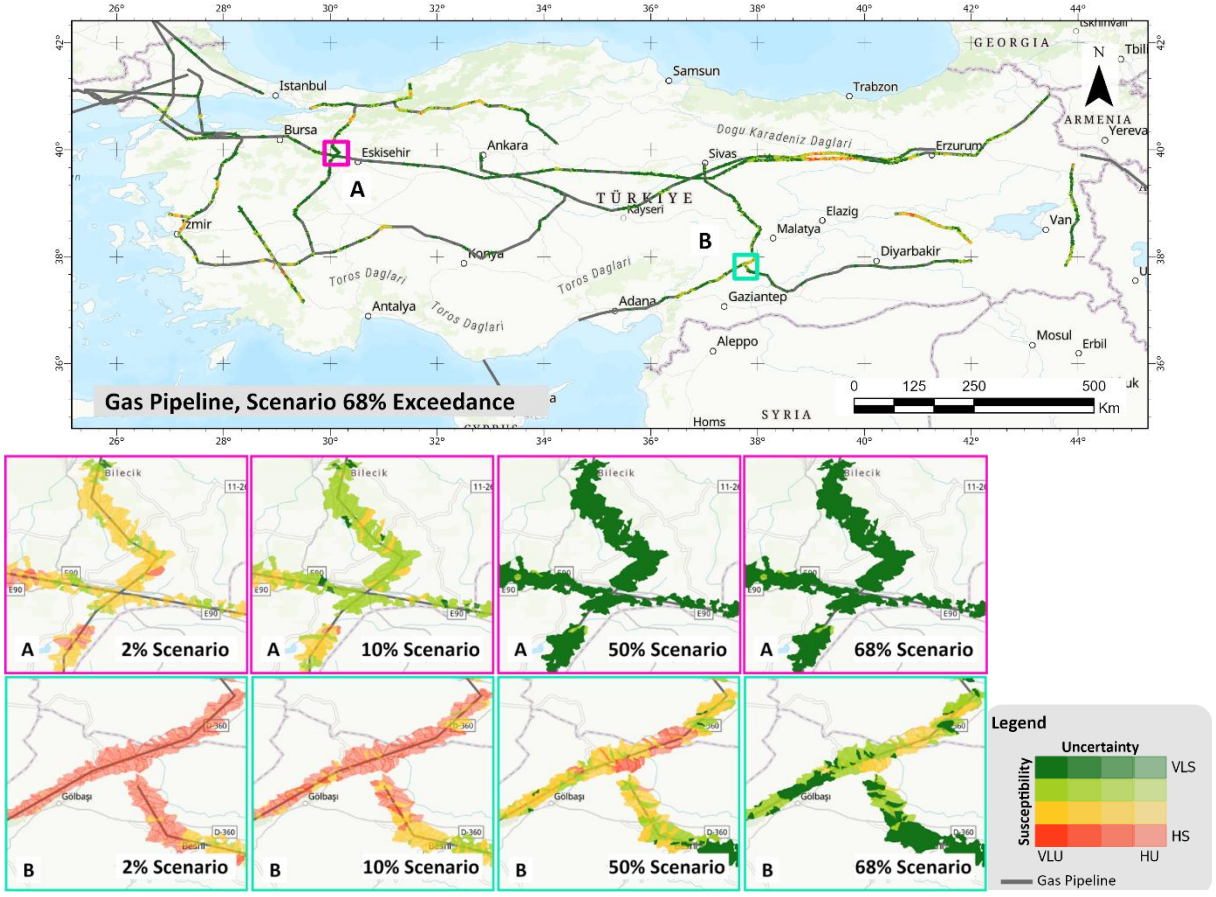

Figure 10 Gas pipeline exposure map under 2%, 10%, 50%, and 68% PGA exceedance probabilities

Tab 4 The length of the gas pipeline exposed to susceptibility under 2%, 10%, 50%, and 68% PGA exceedance probabilities

	VLS		LS			MS			HS	
	VLU	LU	VLU	LU	MU	LU	MU	HU	MU	HU
68% Scenario	1657	39	118	678	21	94	265	2	33	55
50% Scenario	1120	57	131	686	21	248	444	3	94	157
10% Scenario	164	62	48	684	91	151	857	21	204	680
2% Scenario	11	17	6	255	143	42	822	126	79	1459

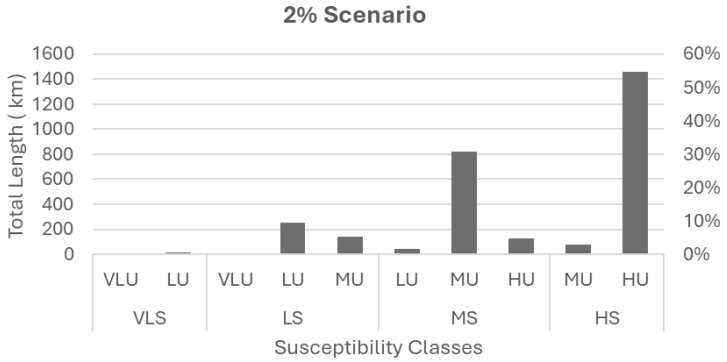

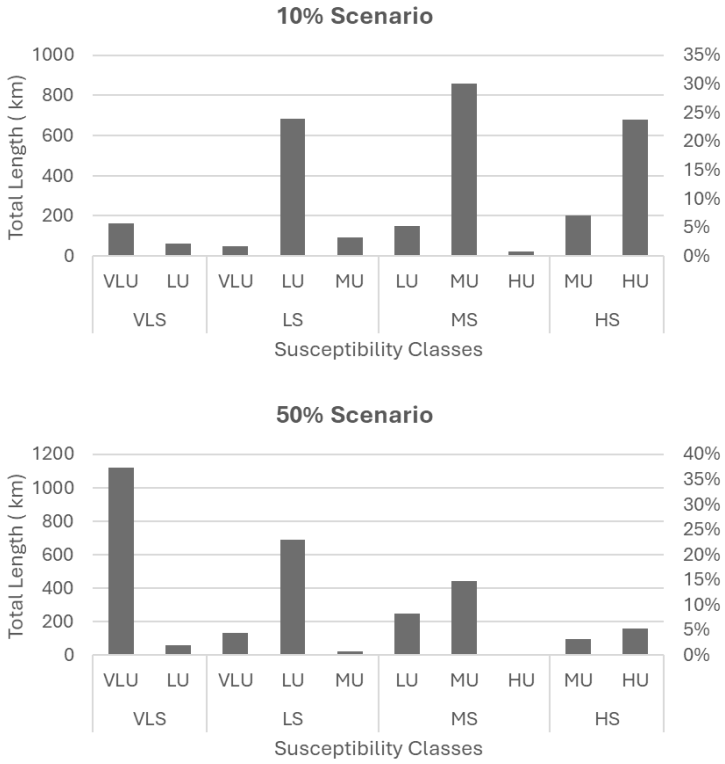

Figure 11 Gas Pipeline exposure bar plots under 2%, 10%, and 50% PGA exceedance probabilities

A.10 Electricity Network Exposure

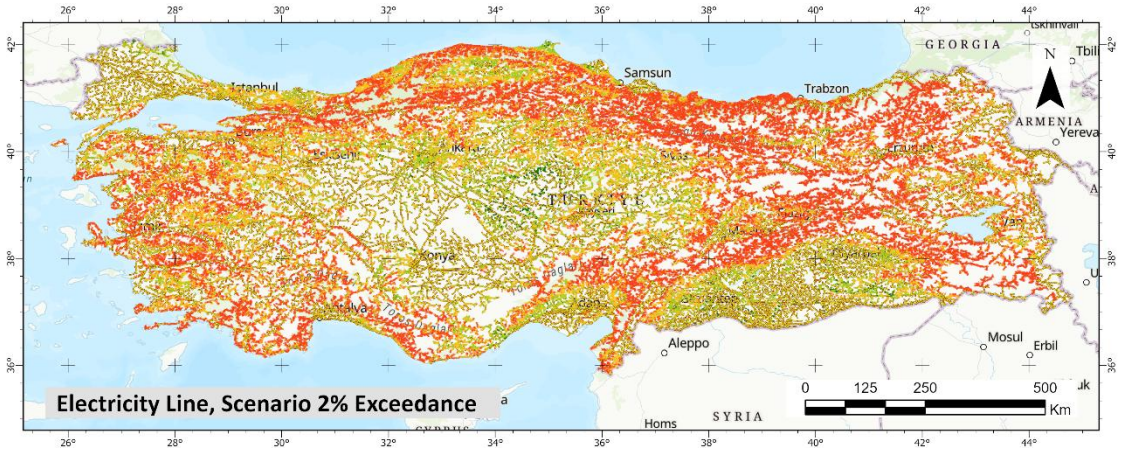

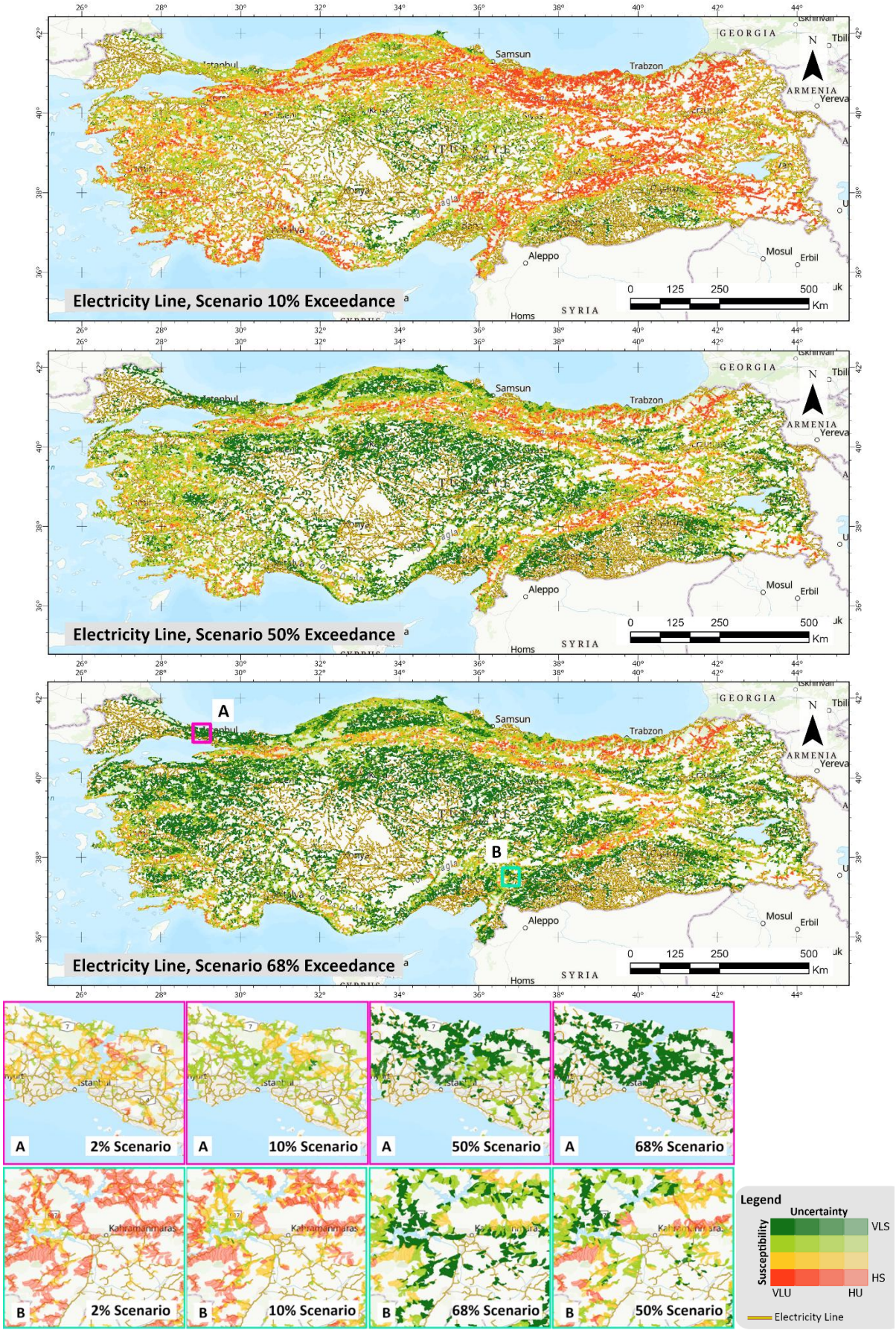

Figure 12 Electricity network line exposure map under 2%, 10%, 50%, and 68% PGA exceedance probabilities

Tab 5 The length of the electricity network line exposed to susceptibility under 2%, 10%, 50%, and 68% PGA exceedance probabilities

	VLS			LS				MS			HS	
	VLU	LU	MU	VLU	LU	MU	HU	LU	MU	HU	MU	HU
68% Scenario	46193	2700	0	3429	23640	3617	1	3146	9625	2473	1173	3758
50% Scenario	31368	3054	0	4846	26152	3567	1	5553	13697	2611	2459	6448
10% Scenario	3732	1733	0	1243	20023	3192	0	5968	27847	3237	6064	26716
2% Scenario	186	381	0	39	6699	3552	0	1492	26524	5566	3745	51570

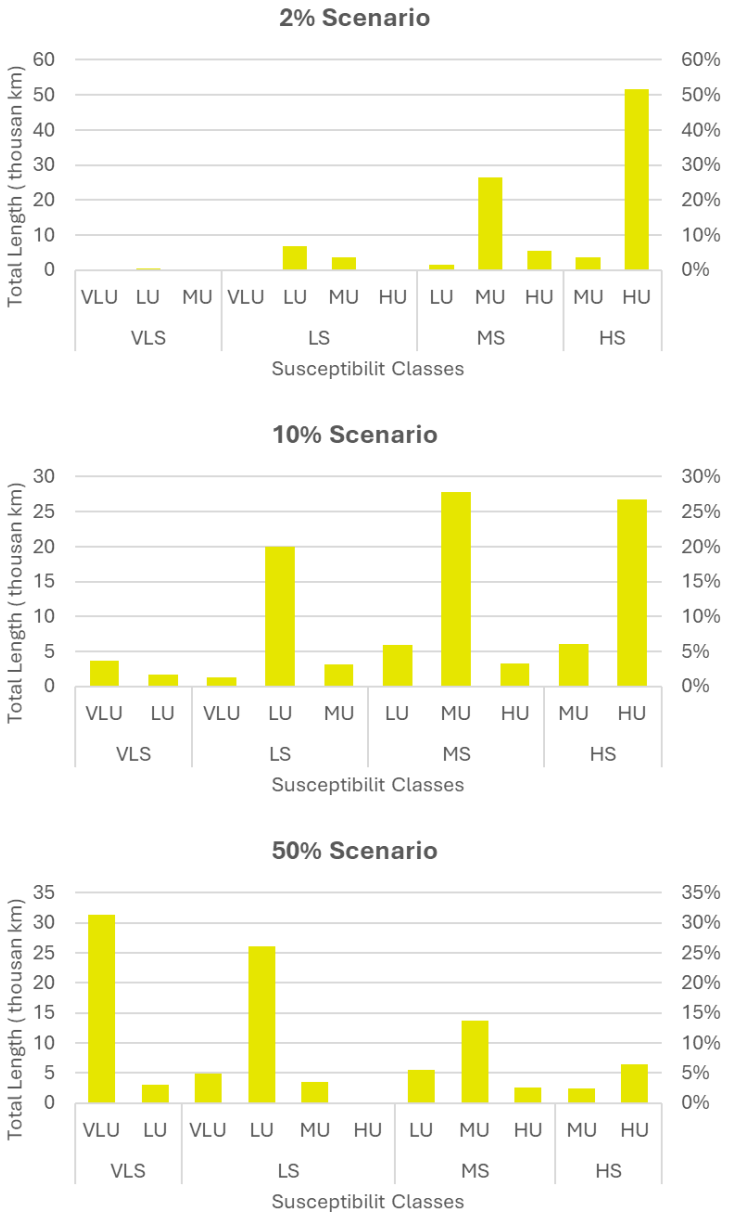

Figure 13 Electricity network line exposure bar plots under 2%, 10%, and 50% PGA exceedance probabilities

A.11 Agriculture Exposure

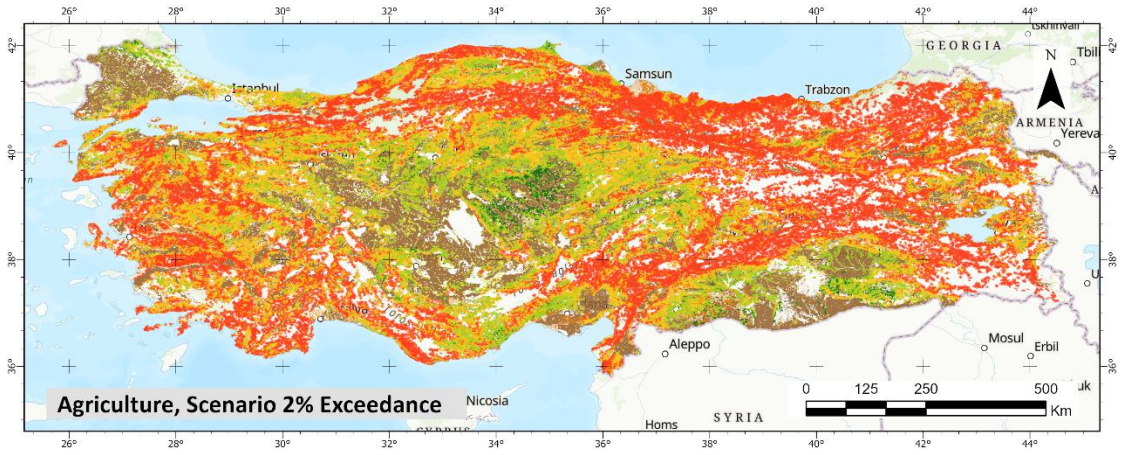

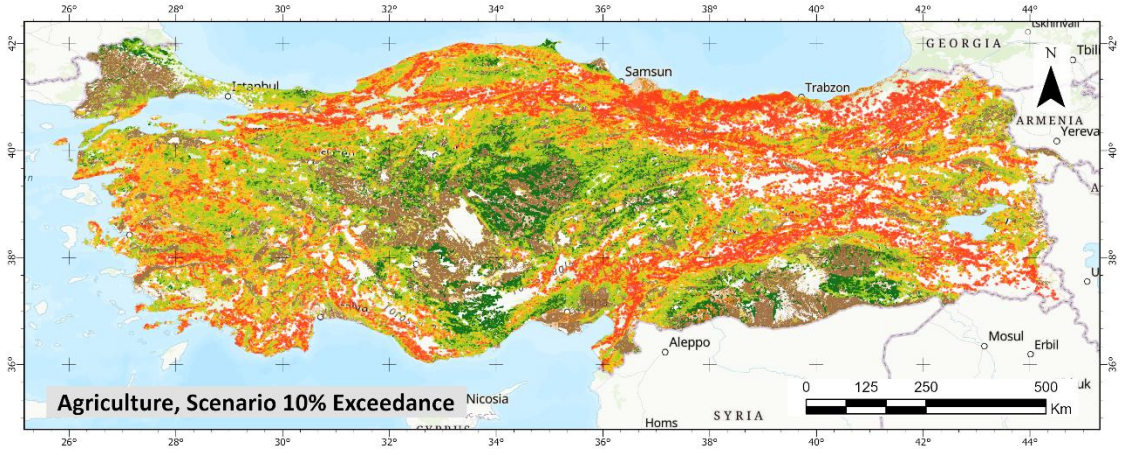

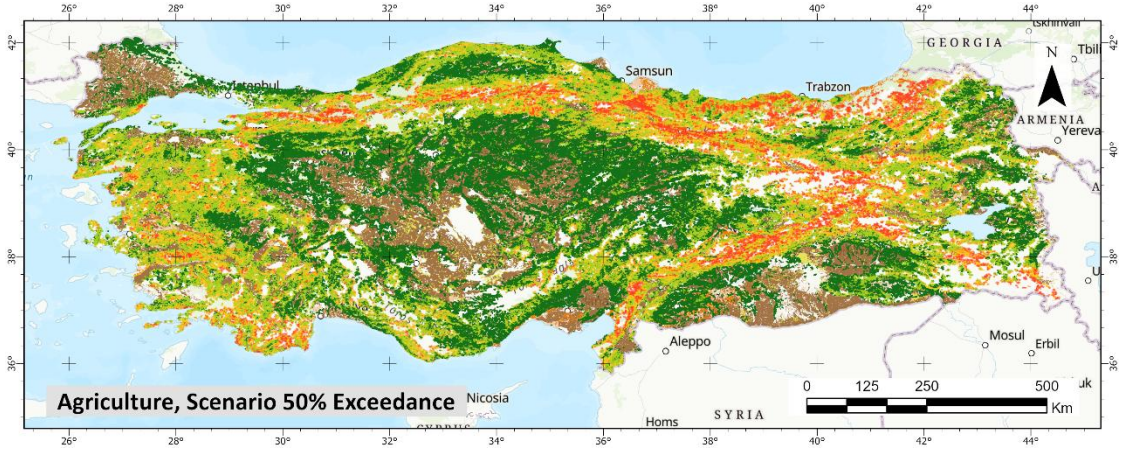

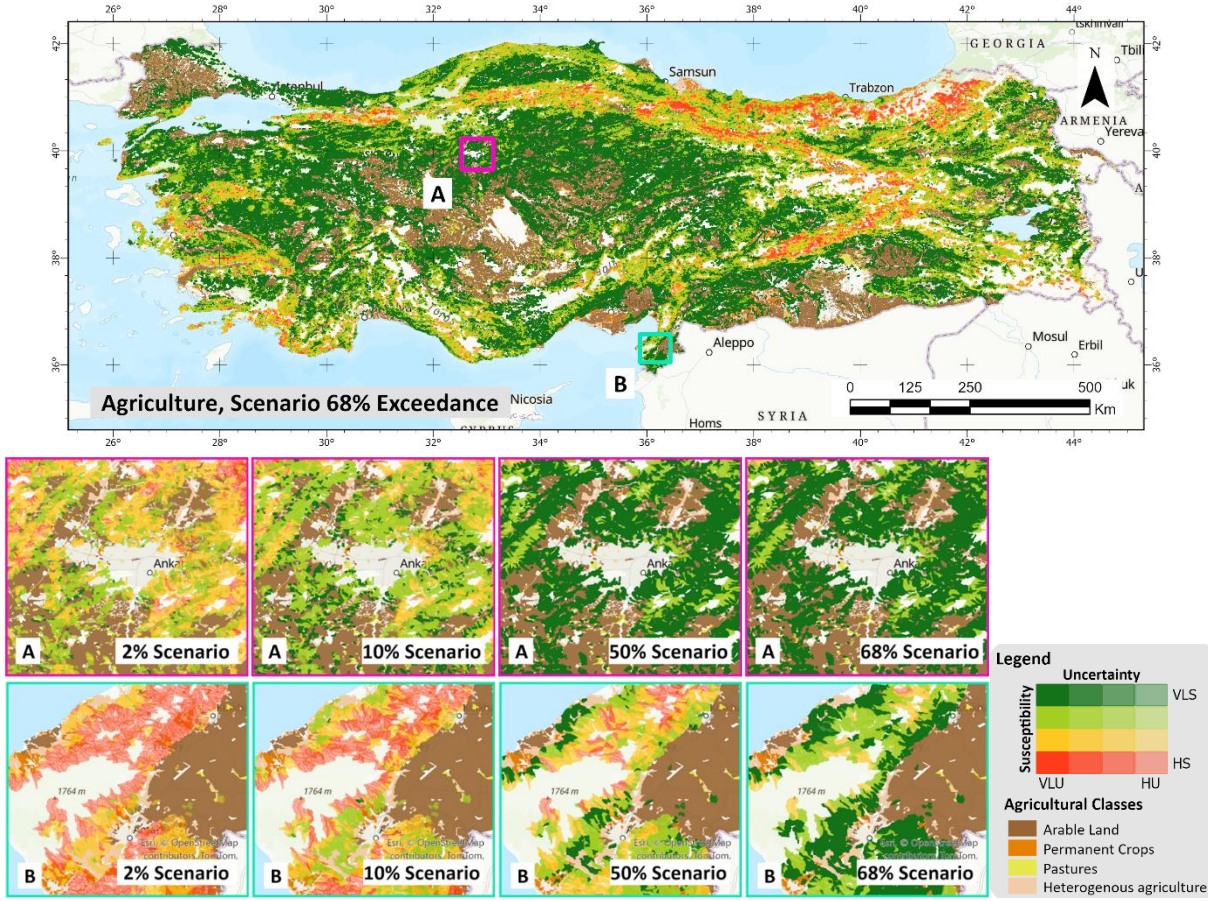

Figure 14 Agriculture areas exposure map under 2%, 10%, 50%, and 68% PGA exceedance probabilities

Tab 6 The amount of the agricultural areas exposed to susceptibility under 2%, 10%, 50%, and 68% PGA exceedance probabilities

68% Scenario	VLS		LS				MS			HS		Grand Total
	VLU	LU	VLU	LU	MU	HU	LU	MU	HU	MU	HU	
Arable Land	2798163	91430	100090	506861	28571		58377	94198	4884	7777	7232	3697584
Permanent Crops	358457	47365	23403	163055	117974		21727	69751	109117	11470	98705	1021026
Pastures	397480	30062	27355	155243	26107		17475	48092	15914	2329	14203	734261
Heterogenous Agri	3892171	223590	294488	1880268	261411	132	231032	681770	151266	74569	203113	7893809
Grand Total	7446271	392448	445337	2705427	434064	132	328612	893811	281180	96144	323254	13346679

50% Scenario	VLS		LS				MS			HS		Grand Total
	VLU	LU	VLU	LU	MU	HU	LU	MU	HU	MU	HU	
Arable Land	2182433	125777	166775	792638	36413		120903	218050	5327	23919	25348	3697584
Permanent Crops	201429	49834	61524	179199	116444		59238	104932	109431	22818	116176	1021026
Pastures	331058	31517	23676	172684	27342		28030	73613	16053	10067	20220	734261
Heterogenous Agri	2608987	236405	411015	2079015	255858	132	496864	1061205	161072	182154	401102	7893809
Grand Total	5323908	443534	662990	3223536	436057	132	705035	1457800	291883	238958	562846	13346679

10% Scenario	VLS		LS			MS			HS		Grand Total
	VLU	LU	VLU	LU	MU	LU	MU	HU	MU	HU	
Arable Land	447994	168806	76112	1262474	176459	215475	951652	50473	98026	250112	3697584
Permanent Crops	28267	23502	4448	167652	38086	56944	179595	75831	51868	394833	1021026
Pastures	73483	17299	9673	146718	33046	31371	210491	28665	27923	155592	734261
Heterogenous Agri	344136	149393	109433	1662277	230997	523183	2291282	242260	483696	1857150	7893809
Grand Total	893880	359001	199666	3239121	478588	826973	3633020	397230	661514	2657687	13346679

2% Scenario	VLS			LS				MS			HS		Grand Total
	VLU	LU	MU	VLU	LU	MU	HU	LU	MU	HU	MU	HU	
Arable Land	29988	55419		2694	664926	303704	105	79800	1354459	237614	105286	863587	3697584
Permanent Crops	551	3503		194	47655	35601	0	6712	212192	68390	19998	626230	1021026
Pastures	6412	6413		1017	90992	29606	6	13106	186904	49089	21724	328991	734261
Heterogenous Agri	15776	35245	11	2380	551266	280438	94	129085	2264561	409293	321300	3884359	7893809
Grand Total	52727	100581	11	6285	1354840	649349	205	228704	4018116	764386	468308	5703167	13346679

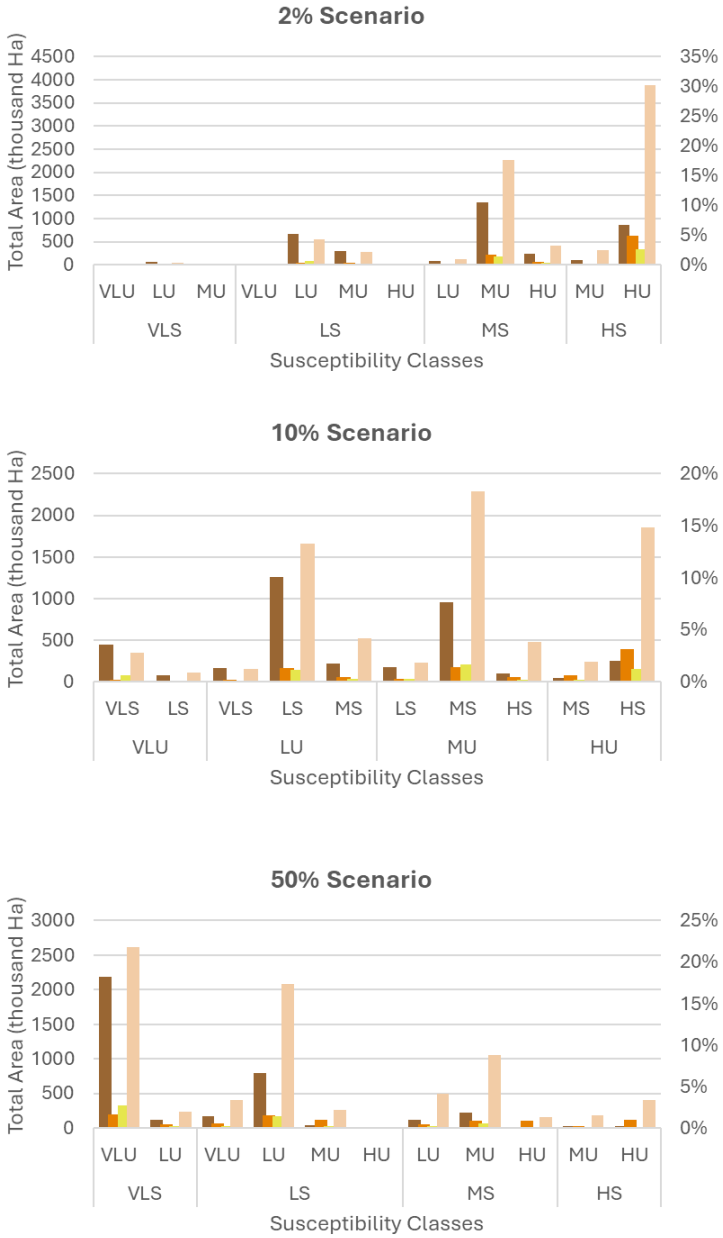

Figure 15 Agriculture areas exposure bar plots under 2%, 10%, 50%, and 68% PGA exceedance probabilities

A.12 Commercial and Industrial Exposure

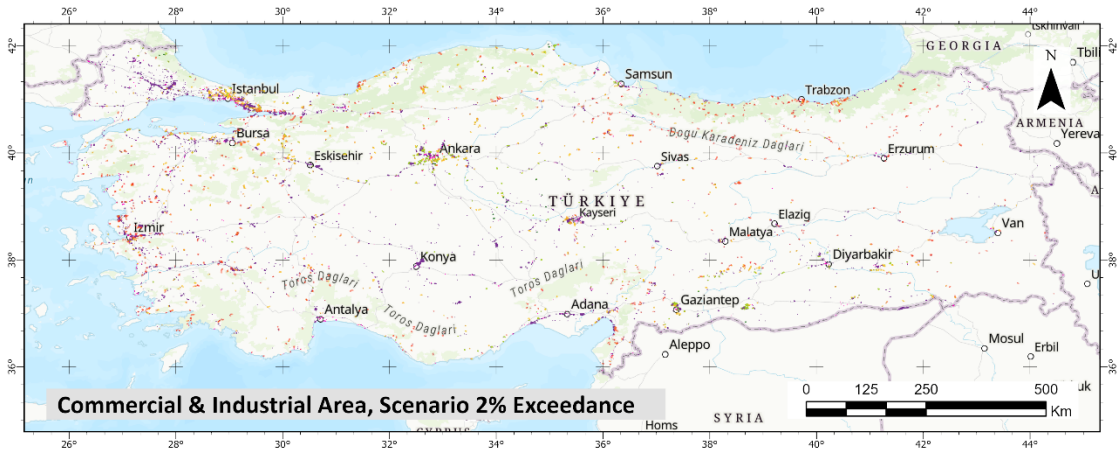

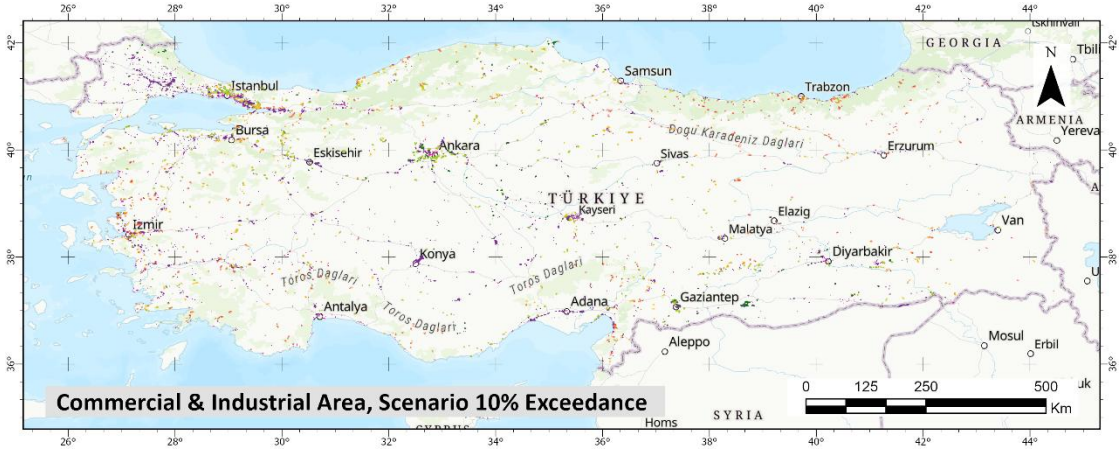

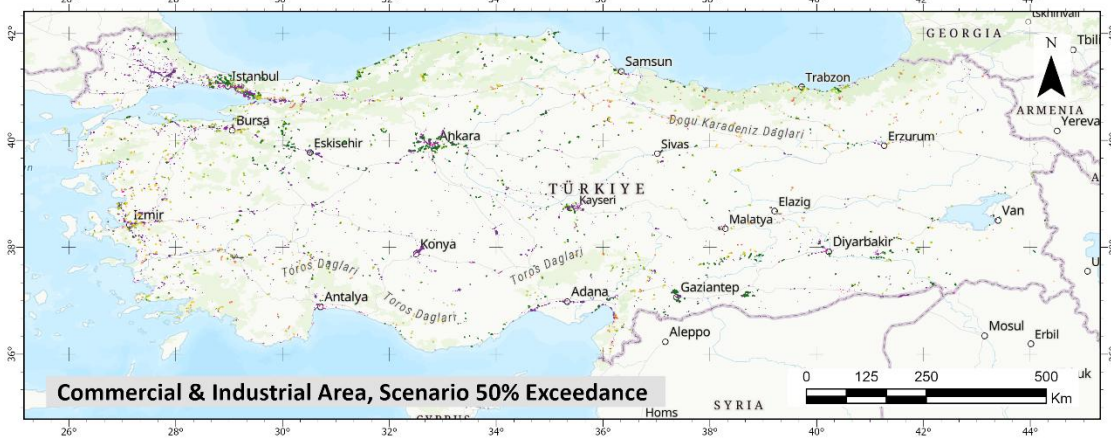

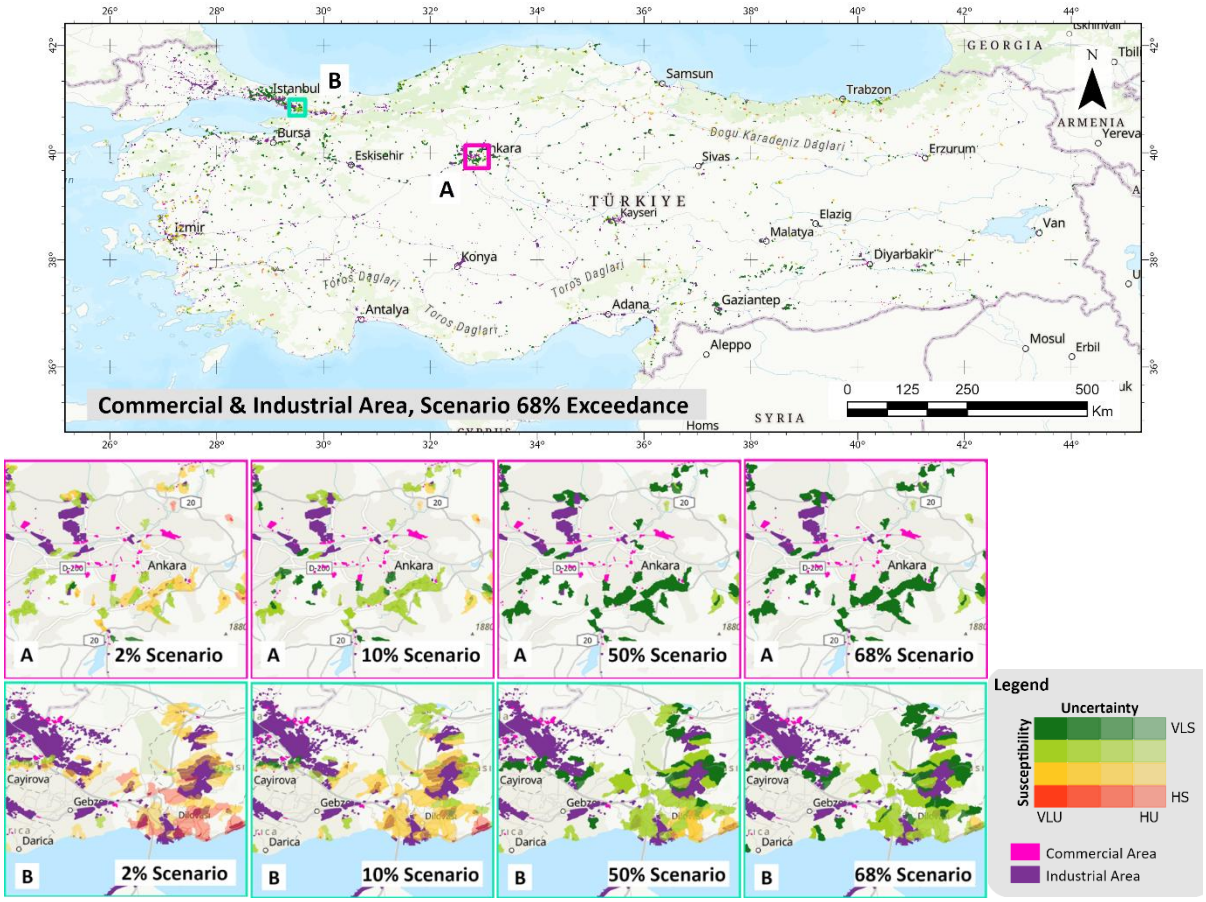

Figure 16 Commercial and industrial areas exposure map under 2%, 10%, 50%, and 68% PGA exceedance probabilities

Tab 7 The amount of the commercial and industrial areas exposed to susceptibility under 2%, 10%, 50%, and 68% PGA exceedance probabilities

68% Scenario	VLS		LS			MS			HS		Grand Total
	VLU	LU	VLU	LU	MU	LU	MU	HU	MU	HU	
Commercial	419.3	12.0	25.7	302.0	7.2	12.6	36.3	5.8	1.5	1.5	823.9
Industrial	13228.4	927.1	766.6	3524.0	406.8	403.5	916.6	133.2	41.6	54.8	20402.6
Grand Total	13647.8	939.0	792.2	3826.1	414.0	416.1	953.0	139.0	43.2	56.3	21226.6

50% Scenario	VLS		LS			MS			HS		Grand Total
	VLU	LU	VLU	LU	MU	LU	MU	HU	MU	HU	
Commercial	315.3	39.6	32.1	330.2	7.0	29.0	58.8	5.6	4.5	1.9	823.9
Industrial	9353.9	1165.3	969.6	5449.7	500.0	1058.3	1482.9	132.6	126.5	164.0	20402.6
Grand Total	9669.2	1204.9	1001.6	5779.8	507.0	1087.3	1541.6	138.2	131.0	165.9	21226.6

10% Scenario	VLS		LS			MS			HS		Grand Total
	VLU	LU	VLU	LU	MU	LU	MU	HU	MU	HU	
Commercial	15.9	41.2	7.7	308.8	101.2	6.3	273.6	14.9	1.7	52.7	823.9
Industrial	2104.2	495.0	147.0	6297.4	1729.2	851.7	5709.9	575.4	406.1	2086.8	20402.6
Grand Total	2120.1	536.2	154.7	6606.2	1830.3	858.0	5983.5	590.2	407.9	2139.5	21226.6

2% Scenario	VLS		LS			MS			HS		Grand Total
	VLU	LU	VLU	LU	MU	LU	MU	HU	MU	HU	
Commercial		1.2		79.5	110.3	8.0	347.1	110.0	2.9	165.0	823.9
Industrial	49.4	32.0	1.5	3492.7	1319.8	204.7	6840.1	1805.8	302.5	6354.1	20402.6
Grand Total	49.4	33.2	1.5	3572.1	1430.1	212.7	7187.2	1915.8	305.4	6519.1	21226.6

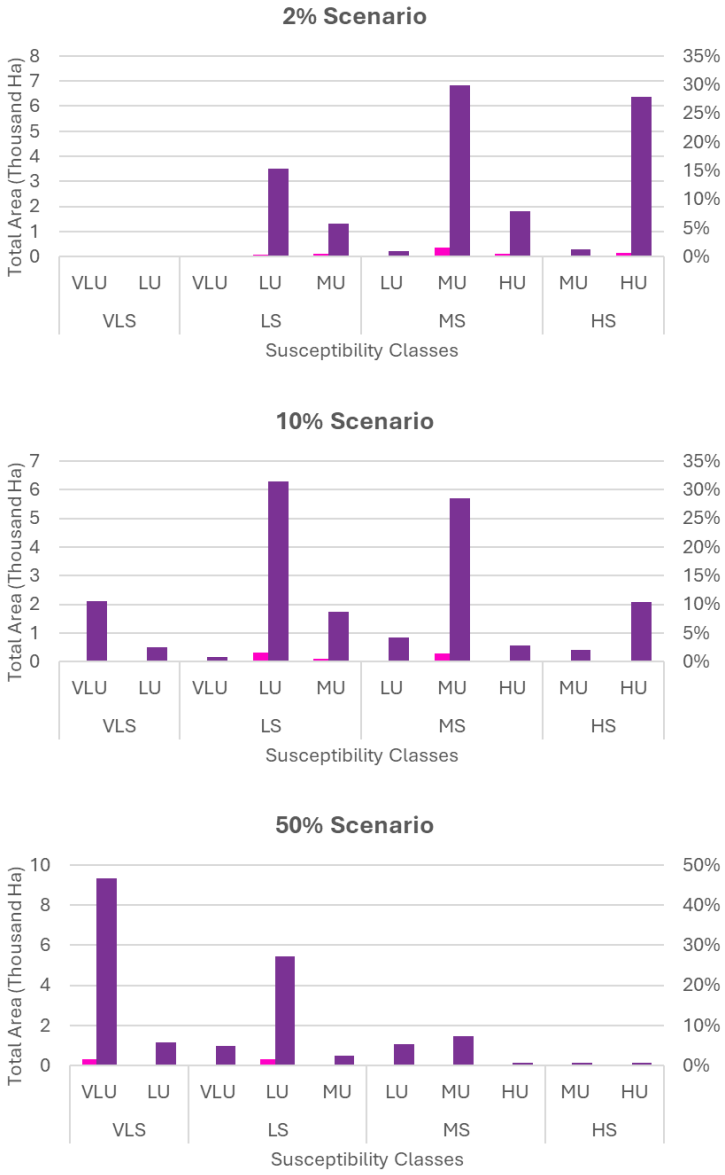

Figure 17 Commercial and industrial areas exposure bar plots under 2%, 10%, and 50% PGA exceedance probabilities

A.13 Building Exposure

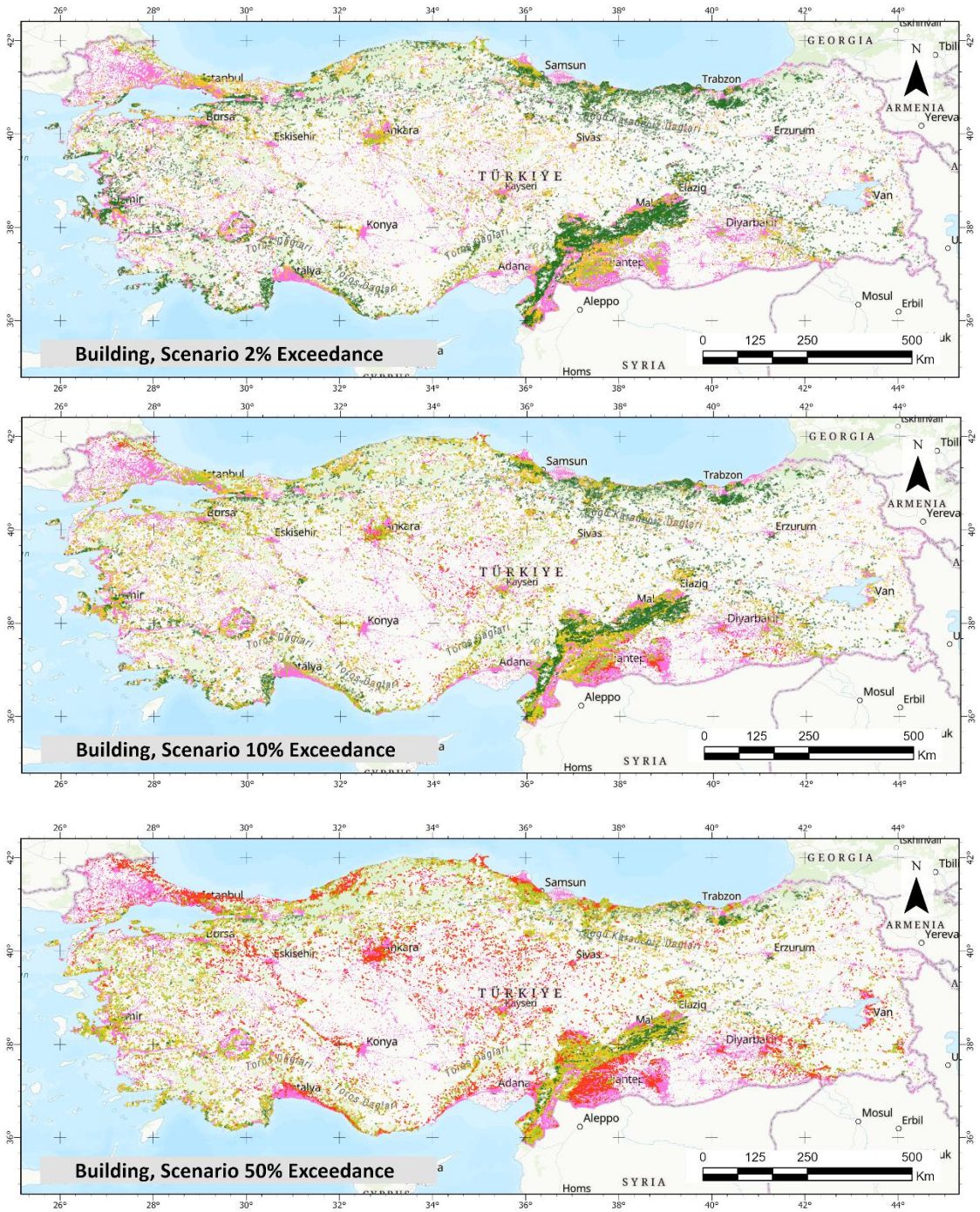

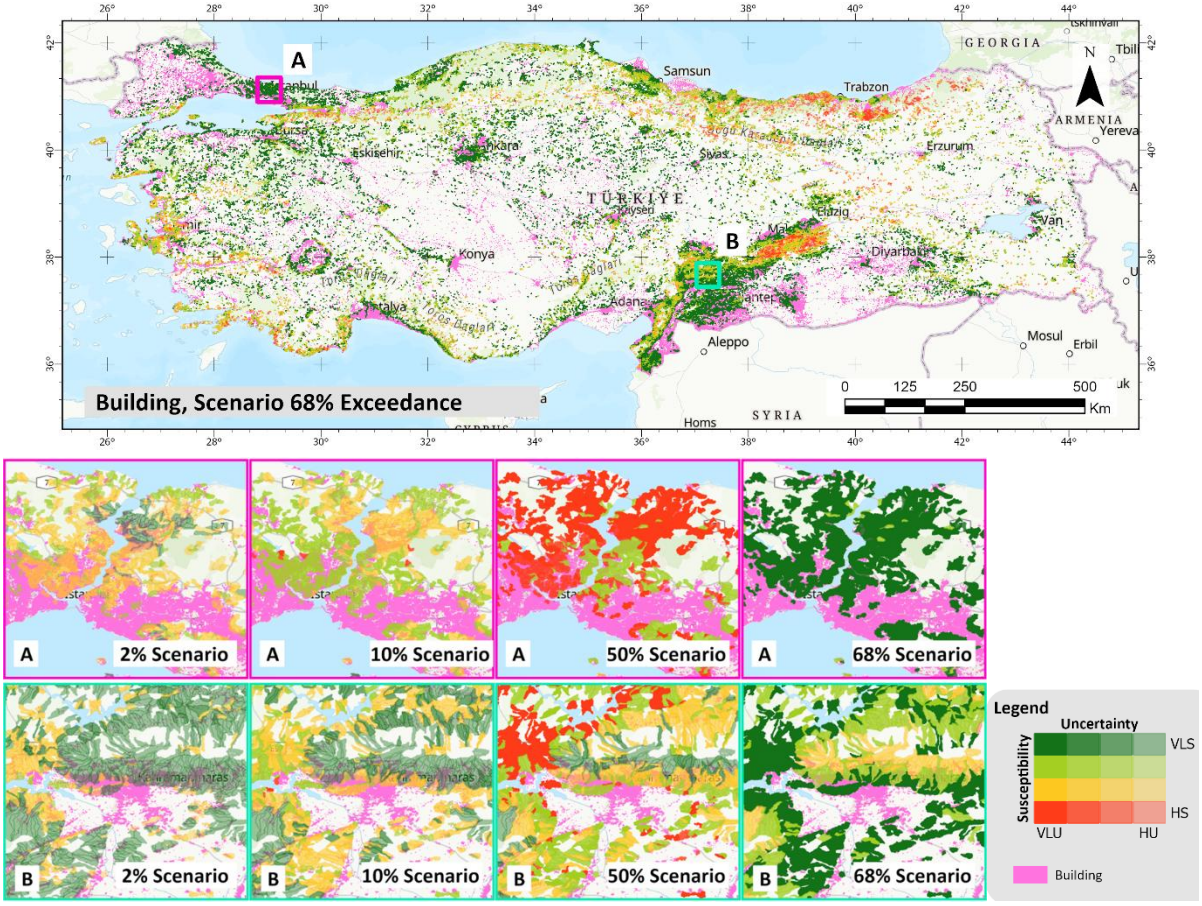

Figure 18 Buildings exposure map under 2%, 10%, 50%, and 68% PGA exceedance probabilities

Tab 8 The amount of the buildings exposed to susceptibility under 2%, 10%, 50%, and 68% PGA exceedance probabilities

	VLS		LS				MS				HS			
	VLU	LU	VLU	LU	MU	HU	VLU	LU	MU	HU	VLU	LU	MU	HU
68% Scenario	498388	45092	33303	233641	70915	0	885	31718	85919	12482	89	650	9479	26002
50% Scenario	259829	78438	55461	295338	71464	0	993	78194	136154	13124	105	1102	20862	37499
10% Scenario	18809	28139	6140	214269	92895	0	92	50067	316795	69982	13	1009	57732	192621
2% Scenario	369	4524	47	58322	63986	1	2	6541	247003	115108	0	152	19101	533407

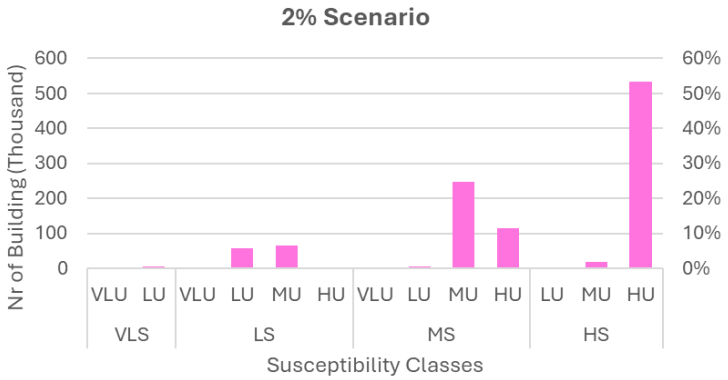

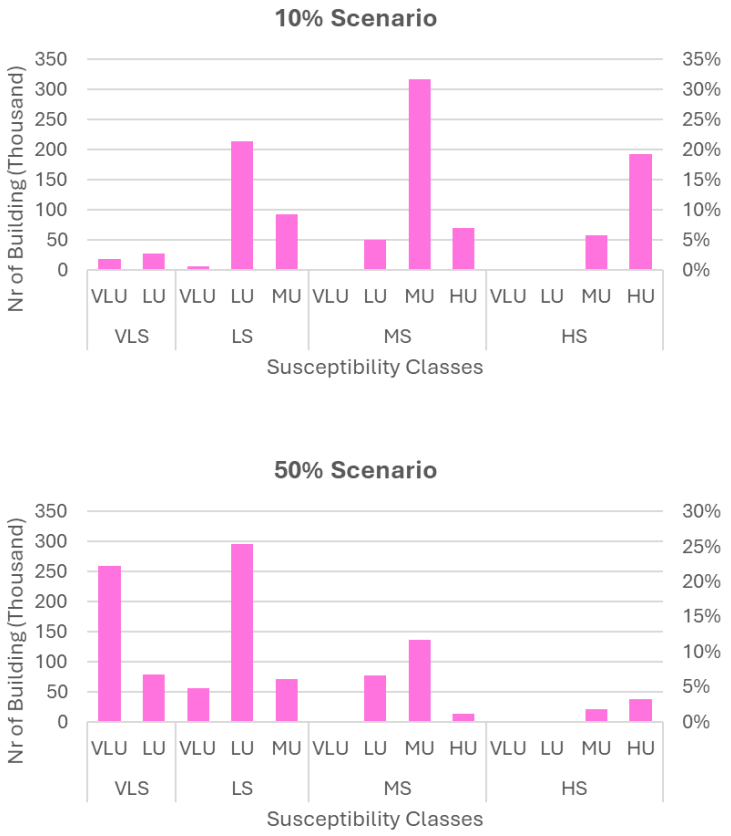

Figure 19 Buildings exposure bar plots under 2%, 10%, and 50% PGA exceedance probabilities

A.14 Critical Infrastructure Exposure

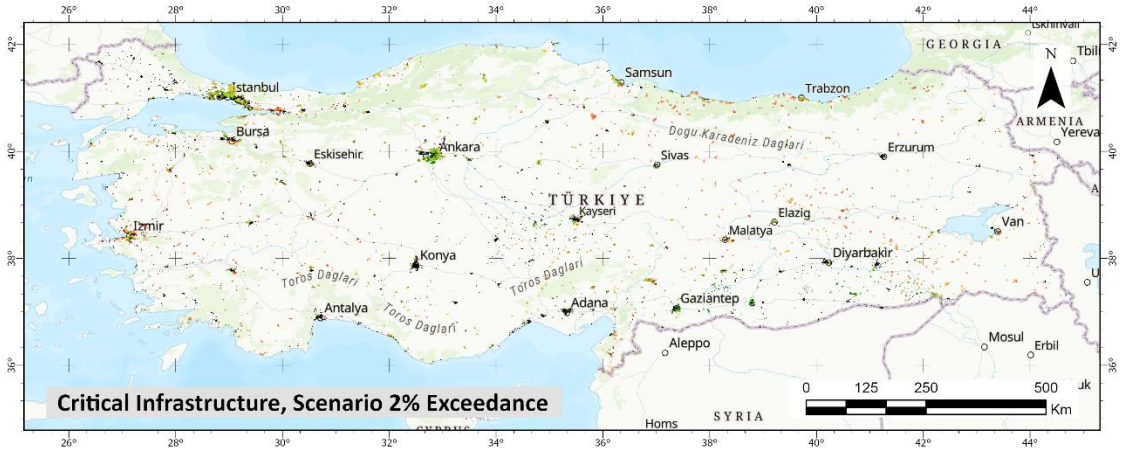

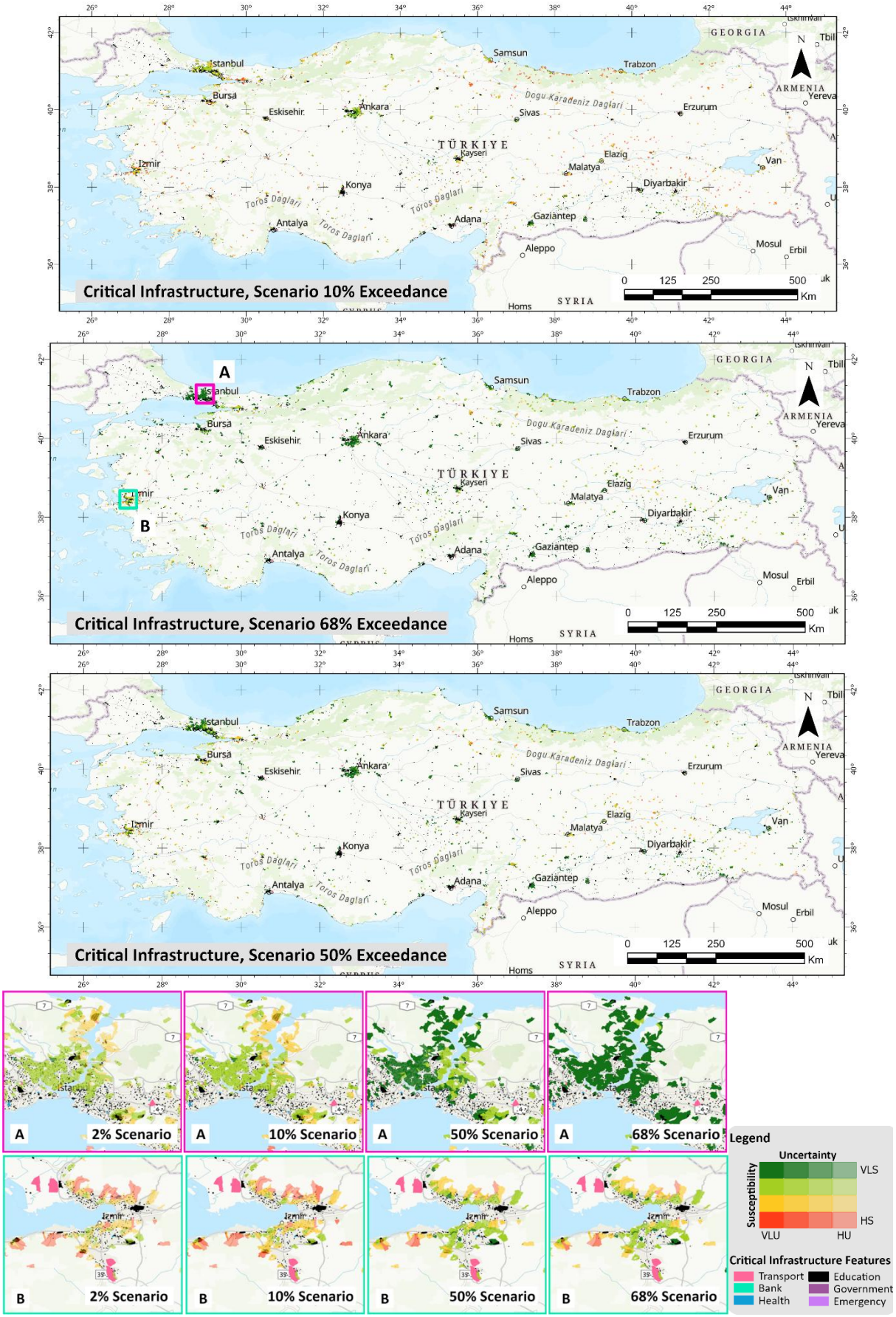

Figure 20 Critical infrastructures exposure map under 2%, 10%, 50%, and 68% PGA exceedance probabilities

Tab 9 The amount of the critical infrastructure exposed to susceptibility under 2%, 10%, and 50% PGA exceedance probabilities

68% Scenario	VLS		LS			MS				HS				Grand Total
	VLU	LU	VLU	LU	MU	VLU	LU	MU	HU	VLU	LU	MU	HU	
Transport	279	20	36	120	6	4	35	61	6		1	5	13	586
bank	30	5			2		1	4	1				3	46
Government	126	8	2	16	3			2	2				1	160
Health	391	33	31	84	40	1	19	18	10		1	1	7	636
Education	2432	194	195	557	230	21	107	154	36	2	5	28	24	3985
Emergency	146	12	13	45	10	2	10	15	5			3	3	264
Grand Total	3404	272	277	822	291	28	172	254	60	2	7	37	51	5677

50% Scenario	VLS		LS			MS				HS				Grand Total
	VLU	LU	VLU	LU	MU	VLU	LU	MU	HU	VLU	LU	MU	HU	
Transport	171	37	43	150	9	4	54	73	6		1	18	20	586
bank	16	10	1	7	2		1	5	1				3	46
Government	100	17		20	3		2	14	2				2	160
Health	239	67	33	145	35	2	41	44	12		2	5	11	636
Education	1611	453	203	857	204	20	192	271	57	2	11	59	45	3985
Emergency	101	26	18	49	10		12	28	5		3	4	8	264
Grand Total	2238	610	298	1228	263	26	302	435	83	2	17	86	89	5677

10% Scenario	VLS		LS			MS				HS			Grand Total
	VLU	LU	VLU	LU	MU	VLU	LU	MU	HU	LU	MU	HU	
Transport	13	13	2	117	49		33	179	11		46	123	586
bank	1	7		11	2			7	5		2	11	46
Government	9	43	1	45	14			26	2		10	10	160
Health	17	31	8	188	72	1	26	157	33	4	36	63	636
Education	185	186	68	1263	396	2	208	874	175	20	189	419	3985
Emergency	14	5	9	75	28		10	50	12	2	16	43	264
Grand Total	239	285	88	1699	561	3	277	1293	238	26	299	669	5677

2% Scenario	VLS		LS			MS				HS			Grand Total
	VLU	LU	VLU	LU	MU	VLU	LU	MU	HU	LU	MU	HU	
Transport	1	2	1	33	28		7	147	64		22	281	586
bank				8	3			10	8		1	16	46
Government	1	2		58	5		4	44	15			31	160
Health		4		53	67		10	206	63	1	16	216	636
Education	4	41	2	420	434	1	92	1224	385	7	162	1213	3985
Emergency	1	3		28	22		9	79	23		8	91	264
Grand Total	7	52	3	600	559	1	122	1710	558	8	209	1848	5677

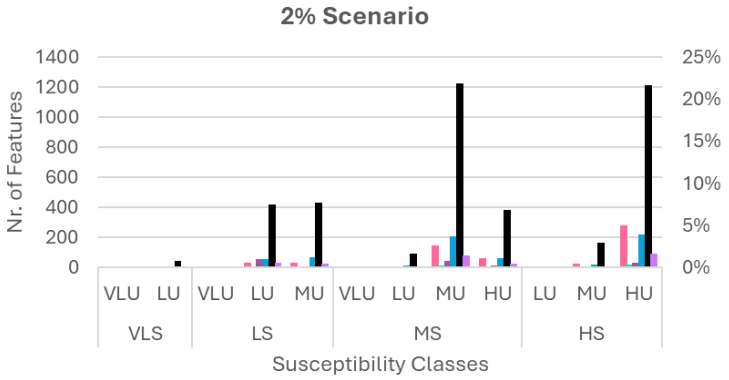

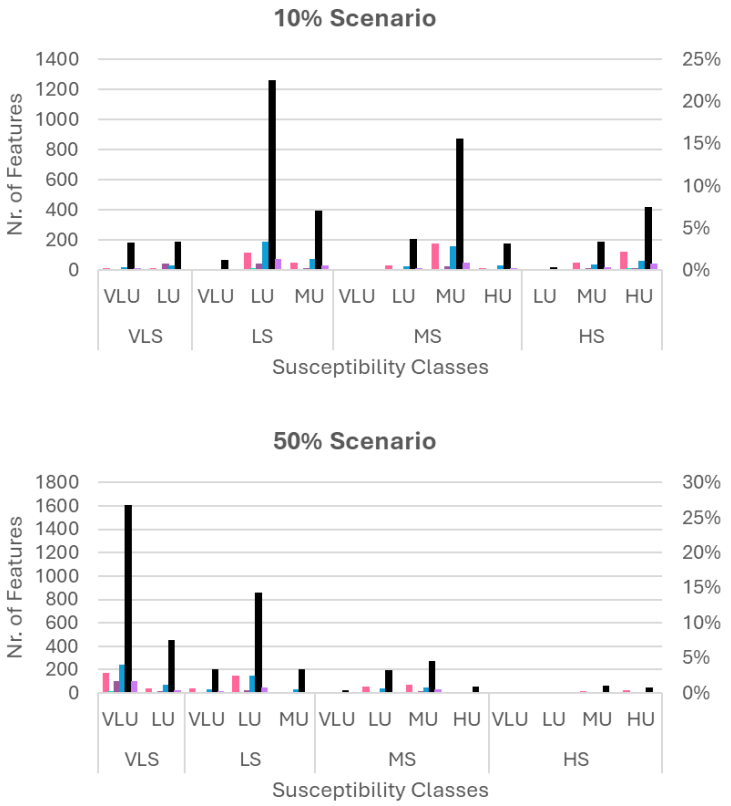

Figure 21 Critical infrastructures exposure bar plots under 2%, 10%, and 50% PGA exceedance probabilities